AEROGEL COATED METAL FOAMS FOR DEHUMIDIFICATION APPLICATIONS

BY

KASHIF NAWAZ

DISSERTATION

Submitted in partial fulfillment of the requirements
for the degree of Doctor of Philosophy in Mechanical Engineering
in the Graduate College of the
University of Illinois at Urbana-Champaign, 2013

Urbana, Illinois

Doctoral Committee:

Professor Anthony M. Jacobi, Chair, Director of Research
Research Professor Predrag S. Hrnjak
Professor Dimitrios C. Kyritsis
Professor Shelly J. Schmidt

ABSTRACT

Separate sensible and latent cooling systems offer significant increases in the overall performance of cooling/dehumidification systems compared to conventional vapor-compression air-conditioning systems. Key to the energy efficiency of such systems is the performance of the heat and mass exchangers that provide sensible cooling and dehumidification. Metal foams have emerged as a potential material for advanced heat exchangers in air-cooling systems. Metal foams have a large surface-area-to-volume ratio and a tortuous structure, which promotes flow mixing in heat exchanger applications. The subject of this thesis is the use of metal foams for air-side heat and mass transfer in air-conditioning heat exchangers.

In this work, the thermal-hydraulic performance of metal foams is studied. Experimental data are obtained, leading to new correlations for the friction factor and the Colburn j factor, valid over a wide range of foam geometry and flow rate. Geometrical parameters (pore size, ligament size, etc.), the base metal of the metal foam, and the geometry of the heat exchanger govern its performance. Metal foams are shown to provide very high air-side heat transfer coefficients, but they also induce high pressure drops. Notwithstanding potential increases in the fan power, it is shown that the overall thermal-hydraulic performance of metal foams can surpass the performance of louvered-fin heat exchangers. Hence, metal foams can compete with state-of-the-art heat exchangers in managing the sensible load.

In order to manage the latent load, metal foams are studied as substrates for aerogel desiccants. Silica aerogels are excellent desiccants, with much higher moisture adsorption rates and capacities than other solid desiccants, such as carbon sieves or salts. In this work, it is shown that silica aerogel can be deployed over the large surface area of metal foams in the form of a thin

film. In this way, the effect of the low thermal conductivity of the desiccant can be mitigated, allowing the heat of adsorption to be removed and regeneration heat to be added via the metal foam substrate. The dehumidification performance of silica aerogels is affected by their micro-structure, which depends on the catalyst used in the sol-gel process to manufacture the desiccants. Dynamic vapor sorption experiments are used to determine mass diffusivity, and the data show that silica aerogel coated on metal foam has the same mass diffusivity in adsorption/desorption as bulk silica aerogel; however, the catalyst used in the sol-gel process significantly affects the mass diffusivity. A silica aerogel coating prepared using hydrofluoric acid as a catalyst (with tetra methyl orthosilicate as a precipitator and methanol as a solvent) results in a mass diffusivity that can be an order of magnitude higher than using other catalysts, such as potassium hydroxide, steric acid *etc*. Analysis of the simultaneous heat and mass transfer processes in the silica aerogel coating shows that the moisture adsorption rate and the moisture saturation time depend on the type of foam and the thickness of coating, as well as the thermophysical properties of the desiccant coating. Silica aerogel coated on the metal foams provides better moisture removal rate and adsorption capacity per unit volume than does a coated flat plate or louvered-fin substrate.

Metal foam heat and mass exchangers have excellent thermal-hydraulic performance and may find application in separate sensible and latent cooling systems for air conditioning. However, questions regarding fouling, manufacturing cost, and heat exchanger geometry constraints remain to be addressed.

ACKNOWLEDGEMENT

I am heartily thankful to my supervisor, Professor Anthony Jacobi, whose encouragement, guidance and support from the initial to the final level enabled me to develop an understanding of the subject and will continue to inspire and motivate me to move forward in future.

I offer my regards to all of those who supported me in any respect during the completion of the thesis. I am grateful to Professor Shelly Schmidt and Sarah Scholl at the Department of Food Science and Human Nutrition (UIUC) for their generous help and suggestions. I would like to show my gratitude to ACRC (Air Conditioning and Refrigeration Center) at University of Illinois at Urbana Champaign and ASHRAE Grant in-Aid program for financing the project.

Lastly, I am thankful to my mother and sisters for their help.

Kashif Nawaz

TABLE OF CONTENTS

Chapter 4-Adsorption and desorption performance of silica aerogel coated metal foams……....91

LIST OF FIGURES

LIST OF TABLES

NOMENCLATURE

A_{base}	Base surface area (m^2)
A_{fr}	Frontal area (m^2)
A_{min}	Minimum flow area (m^2)
Bi_t	Heat transfer Biot number (-)
Bi_m	Mass transfer Biot number (-)
C	Inertia/friction coefficient (m)
c_p	Specific heat (J/kg-K)
C_{max}	Maximum moisture adsorbed (kmol/m^3)
C_0	Initial moisture concentration (kmol/m^3)
C_∞	Ambient moisture concentration (kmol/m^3)
D_{eff}	Effective diffusion coefficient (m^2/s)
D_h	Hydraulic diameter (m)
D_f	Ligament diameter (m)
D_p	Pore diameter (m)
F	Correction factor for LMTD
f	Friction factor (-)
G	Mass flux (kg/m^2-s)
h, h_T	Heat transfer coefficient (W/m^2-K)
h_m	Mass transfer coefficient (m/s)
j, j_{Dp}	Heat transfer Colburn j factor (-)
$j_{m,Dp}$	Mass transfer Colburn j factor (-)
K	Permeability (m^2)
k_{eff}	Effective conductivity (W/m-K)
L	Desiccant coating thickness (m)
L_h	Hydraulic length (m)
$LMTD$	Log mean temperature difference (K)
Pr	Prandtl number (-)
$\Delta P/L$	Pressure drop per unit length (Pa/m)

q	Heat transfer rate (W)
r_1	Radius of uncoated ligament (m)
r_2	Radius of coated ligament (m)
R_{bond}	Bonding resistance (K/W)
Re_{dh}	Reynolds number based on average pore diameter
Sc	Schmidt number (-)
T	Temperature (K)
T_o	Surface temperature of substrate (K)
T^*	Transient temperature (K)
$\bar{T}$	Steady state temperature
T_i	Initial temperature of desiccant (K)
U	Overall heat transfer coefficient (W/m^2-K)
V	Face velocity (m/s)

Greek letters

α	Heat of adsorption (J/kmol)
β	Thermal-diffusion coefficient (kmol/sec-K)
κ	Thermal diffusivity (m^2/s)
ε	Porosity (%)
ρ	Density (kg/m^3)
μ	Kinematic viscosity (N-s/m^2)
η_0	Overall surface efficiency
η_f	Fin efficiency (%)

Chapter 1- Introduction

1.1 Research background

Commercial and residential buildings consume one-third of the power produced world-wide [1.1]. In the United States alone, buildings use 40% of total energy, including 27% of electricity generation, 12% of water consumption and 60% of all non-industrial waste [1.1]. By 2025, buildings worldwide will be the largest consumers of global energy - greater than the transportation and industry sectors combined [1.1]. A considerable part of this energy is used to maintain moisture levels for comfort and process control. The humidity level can be controlled using liquid or solid desiccant systems. Solid desiccants are preferred over liquid-desiccant systems due to the ease of application. Unlike liquid desiccants they do not undergo any chemical change during the moisture removal process. Different types of solid desiccants, such as a molecular sieve, activated carbon, and silica aerogel *etc.*, employed for humidity control have a microscopic porous structure. When they are used in air conditioning, refrigeration, and cryogenic systems, the system performance is affected by the desiccant characteristics, such as pore size, porosity, and diffusion coefficient. The solid desiccant can be deployed by coating a solid surface (a substrate). The characteristics of the substrate, such as surface area and thermal conductivity, affect the moisture removal performance considerably. Therefore, an appropriate selection of desiccant and substrate is important to the overall performance of the dehumidifying system.

One candidate for a substrate material is metal foam. There has been considerable interest in establishing the thermal-hydraulic performance of metal foams when used as a heat exchanger. Despite manufacturing and implementation issues, these materials hold promise as both heat exchangers and heat sinks [1.2]. The open porosity, low relative density, high thermal conductivity, large surface area per unit volume, and the ability to enhance fluid mixing can make metal foam thermal management devices efficient, compact, and light-weight. Metal foam heat exchangers are anticipated to have relatively large pressure drop, but they are also expected to have a large heat transfer rate compared to conventional fins. This expectation is reinforced by the complex geometry of the foams, which results in a high degree of boundary layer restarting and wake destruction by mixing. Due to the relatively recent emergence and complex structure of metal foams, they are still incompletely characterized. Interest in using metal foams for heat exchangers and other applications motivates continued research on their properties. Central to this need is an accurate evaluation of the flow characteristics to assist in making the trade-off analysis between the increased heat transfer and the associated increase in the pressure drop for foam heat exchanger and heat sink designs.

After determining their thermal-hydraulic performance as heat exchangers, metal foams can be used as substrates for silica aerogel desiccants, and this method of dehumidification is a promising alternative to mechanical vapor-compression systems. The main advantage of desiccant systems is the separate handling of latent and sensible energy loads, thus improving efficiency by 30-50% in air cooling and dehumidification [1.3].

The current study is focused on evaluating the dehumidification performance of aerogel-coated metal foams.

1.2 Separate sensible and latent cooling (SSLC) systems

1.2.1 Introduction to SSLC system

During operation the conventional air-conditioning system manages two kinds of cooling loads, the sensible and latent loads. The sensible cooling is achieved by an evaporator through reducing the temperature of the supply air. During conventional operation the refrigerant temperature in the evaporator is below the dew point of the supply air, and moisture in the air condenses on the evaporator and therefore reduces the humidity ratio of the delivered air. Thus, the latent heat is removed due to the condensation of water vapor in the air.

Theoretically, the process of supply air flowing through the evaporator follows the path that is composed of a horizontal sensible load removal part (point A to point B) and a latent load removal part along the 100% relative humidity (RH) line from B to C as presented in Figure 1.1. Commonly, the temperature of point C is too low for thermal comfort, therefore a reheat process is sometimes performed by which temperature is increased from point C to the temperature of point D. The reheat process, usually carried out by electric heaters, requires extra energy input and increases the total net energy input. Hence, the reheat process reduces the overall performance of the system.

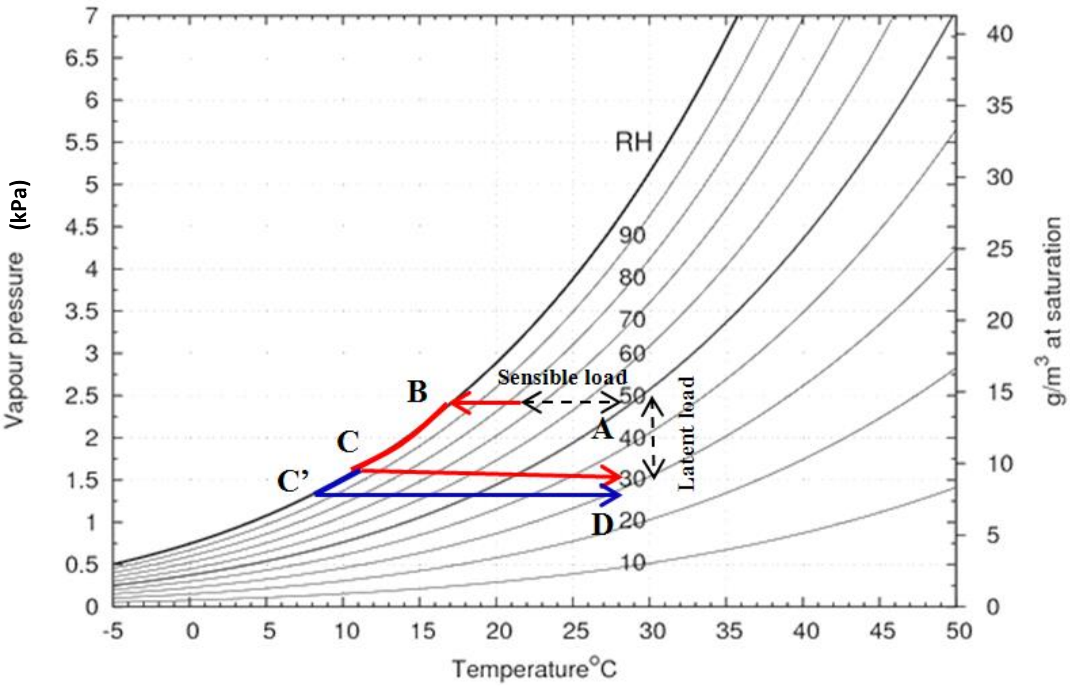

Figure 1.1 Operation of conventional air conditioning system

The reheat process in conventional systems is required due to the coupled control of sensible and latent cooling. The path from point B to point C along the 100% RH line reveals that the amount of latent cooling and the amount of sensible cooling are coupled. Hence, removing a certain amount of water vapor requires an accompanying ratio of temperature reduction. Therefore, the more the latent cooling takes place the more likely sensible over-cooling will result. Such a dependent relationship not only increases the cost of operation, but also causes a control issue in conventional systems. For example, when there are more people in the building, extra latent cooling (the vertical blue arrow pointing downward) is required. The supply air point moves downwards to point C'. Meanwhile, an unnecessary amount of sensible cooling has to be added to the room as well. This requires more reheat power input to increase temperature for thermal comfort and further reduces the performance of the HVAC system.

Separate sensible and latent cooling (SSLC) systems are considered a possible alternative to conventional air conditioning systems. The psychrometric process of a SSLC system is presented in Figure 1.2. This system consists of one vapor compression system and one solid desiccant wheel (enthalpy wheel). The vapor compression system provides only sensible cooling (point A to point B) required by the conditioned space at both elevated air temperature leaving the evaporator and a higher air mass flow rate. The reason for a higher air mass flow rate requirement is to compensate for the reduced enthalpy difference of air across the evaporator, and to maintain the capacity of sensible cooling. Since the vapor compression system operates above the dew point temperature of supply air and is not required to provide the latent cooling, the desiccant wheel is used to reduce the water vapor content in the part of the air leaving from the sensible evaporator. The part of the dry air from the desiccant wheel mixes with the rest of the air from the evaporator and is delivered to the conditioned space (point D).

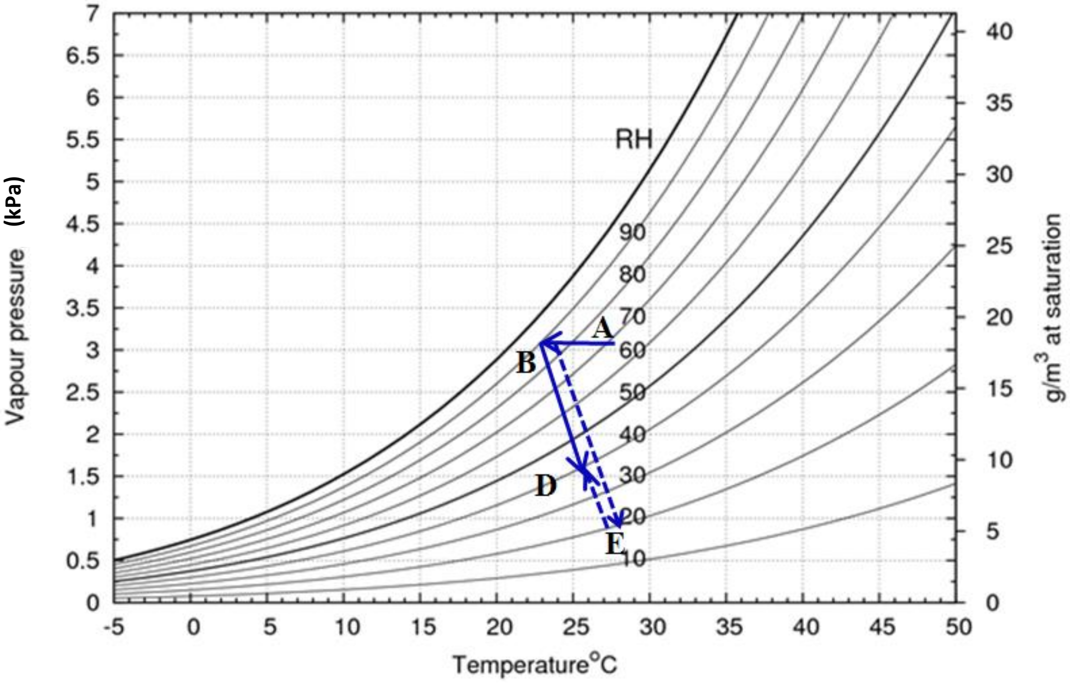

Figure 1.2 Operation of SSLC system (with enthalpy wheel)

To summarize, SSLC systems have two features that distinguish them from the conventional systems. First, since the vapor compression system used in an SSLC system operates above the dew point temperature, the supply air temperature is thermally comfortable and can be sent to the conditioned room directly. Hence, no reheat is necessary in SSLC systems. Secondly, an SSLC system uses a vapor compression system to provide sensible cooling. As a consequence, any fluctuations in sensible cooling demand can be simply met by changing the capacity of the vapor compression system. In order to meet the fluctuations of latent cooling demand, the capacity of the desiccant system can be enhanced, for example the rotation speed of the enthalpy wheel can be adjusted to provide the latent cooling load. However, it should be noted that the loads are still coupled due to the mixing of streams, and such processes can be performed within a limited range of operation. Any latent cooling demand change beyond the reach of the rotation speed adjustment will be unmet. Such drawbacks justify the need of a desiccant moisture removal device with more independent load matching and better operation control. Furthermore, although a desiccant wheel is a stand-alone device providing latent cooling, any amount of the latent capacity change would theoretically lead to the same amount of change in sensible heat generation. Therefore, the vapor compression system must increase the cooling capacity to cover the extra heat. Thus, there is still a link between the processes in vapor compression system and desiccant wheel and the independent treatment is sometimes leads to impractical conclusions.

1.2.2 Literature review

Two different configurations of SSLC systems have been proposed in the literature. One SSLC system consists of two vapor compression cycles and the other one consists of one vapor compression cycle and one solid desiccant wheel. The first configuration was theoretically studied and simulated under different ambient conditions. The second configuration was studied both theoretically and experimentally because of its better performance. Ling *et al.* [1.4] proposed to separate the sensible and latent loads using two vapor compression systems. The first system removed sensible heat only, while the second system removed both latent and a small amount of sensible heat. Under the standard ambient conditions (35°C, 44% relative humidity (RH)), the energy consumption of such an SSLC system was reduced by 30% compared to that of a conventional system, and the savings was reported to be up to 50% under the hot and dry condition (37°C, 15% RH).

Many studies have focused on the use of a vapor compression cycle for the sensible load and solid/liquid desiccant equipment for the latent load. Yadav [1.5] investigated a hybrid system consisting of a liquid desiccant and a vapor compression system. The objective of the study was to find the best operating condition of such a system, and the conclusion was that the system performed well for a low sensible heat factor (SHF) or when the ambient humidity ratio was high. The SHF is defined as the ratio of sensible heat over the total heat load. Dai *et al.* [1.6] studied the application of integrating a liquid desiccant device and a vapor compression cycle. The experiment was conducted under the AHRI standard 210/240 conditions (35°C, 44% RH, AHRI, 2008) and the cooling capacity was 5 kW. The coefficient of performance (COP) of the vapor compression cycle improved from 2.2 to 3.39 because of the assistance from the liquid desiccant. Ma *et al.* [1.7] utilized a similar configuration to a larger scale application. A green building demonstration project in Shanghai required a total of 60 kW cooling capacity, and the latent cooling was provided by a liquid desiccant unit that was regenerated by the heat from condenser. A similar study was also reported by Katejanekarn and Kumar [1.8], where solar energy was used for regeneration.

Dhar and Singh [1.9] simulated a hybrid system of a solid desiccant wheel (DW) and a vapor compression cycle. They demonstrated that the hybrid system had maximum energy savings under hot and dry weather. Depending on the desiccant material, the temperatures of regeneration can vary from 50°C to above 100°C; therefore, different heat sources are reported to drive desiccant devices.

Jia *et al.* [1.10] studied the performance of a solid desiccant wheel using lithium chloride as the adsorbent. The temperature required to regenerate the wheel was set to be 100°C, and one regeneration heater was used as a heat source. Ghali [1.11] numerically simulated a hybrid system in the ambient conditions. The main feature of this hybrid system was that the regenerative heat needed by the desiccant wheel was partly supplied by the condenser, while the rest was supplied by an auxiliary gas heater. Casas and Schmitz [1.12] studied the integration of a DW and a cooling, heating, and power (CHP) unit. In their study, the waste heat from the CHP unit could be utilized for lithium chloride regeneration. However, the regeneration temperature was only in the range of 50°C to 60°C. The difference in regeneration temperatures in these studies may be caused by different dehumidification requirements.

An exergy analysis of a solar driven hybrid system was presented by Ahmed *et al.* [1.13]. They compared the performance of the hybrid system operated at different ambient conditions and different mass flow rates through the desiccant wheel. Ling *et al.* [1.14] provided a theoretical and experimental study of the integration of VCC and a low-temperature-regenerated desiccant wheel. A major challenge for this kind of system is to balance the performance of the desiccant wheel and the COP of the vapor compression cycle. Zadpoor and Golshan [1.15] simulated the effect of applying desiccant-based evaporative cooling systems to a gas turbine cycle. The outdoor air, in this study, is fed to a desiccant wheel first and then to an EC device. This results in a lower outlet air temperature than a stand-alone EC device can provide. The system is useful especially in hot and humid conditions, in which the wet bulb temperature is not low enough compared to the air temperature. Lazzarin [1.16] numerically investigated both the direct EC and indirect EC under various conditions and proposed a new diagram-based analysis method to determine whether or not using EC is profitable. The integration of heat recovery wheels, i.e., sensible wheels (SW), and enthalpy wheels (EW) into SSLC systems also has been investigated.

Jeong and Mumma [1.17] developed practical EW effectiveness correlations based on extant complex formulations and models using statistical methods. The correlations relate the sensible and latent effectiveness of the EW to six variables, including entering air temperature and relative humidity. The two types of EW materials considered in the paper were silica gel and a molecular sieve. Nobrega and Brum [1.18] developed a mathematical model for the adiabatic adsorption within silica-gel and used it to simulate the performance of an enthalpy wheel and found an optimal non-dimensional revolution rate at which the enthalpy recovery is maximized.

1.3 A new SSLC system

1.3.1 Research undertaken

Despite earlier studies on heat sinks made of metal foams, there is very little research available on the thermal-hydraulic performance of metal foams when used under the conditions prevailing in HVAC systems, particularly under dehumidifying conditions. The experimental data for thermal-hydraulic performance of metal foam heat sinks is limited and covers a small part of the parameter space encountered in HVAC systems. In order to make comparisons to existing compact heat exchanger designs, such as louvered-fin heat exchangers, experimental data are needed. In this work, a study to provide general correlations for pressure drop and heat transfer based on a wide range of experimental conditions and geometrical parameters (pore size, flow depth *etc.*) was pursued.

Silica aerogel is being used as a solid desiccant in enthalpy wheels, but there has been no serious effort to characterize silica aerogel dehumidification and related it to microstructure. Hence the adsorption and desorption performance of silica aerogels prepared by different methods, has yet to be determined. In this work, silica aerogels having different chemical compositions were analyzed for their microstructure and adsorption and desorption behavior.

A device consisting of metal foam coated with silica aerogels (a macroscopic porous media coated with microscopic porous media) for dehumidification purposes has never been fabricated and characterized. Yet, as suggested in the literature review, there are good reasons to believe such a system can provide more effective humidification and dehumidification due to large surface area of a conductive substrate (metal foams) coated with silica aerogels. Hence, in this work this new desiccant system was constructed, and then its potential advantages and disadvantages in comparison to conventional systems were explored.

1.3.2 Statement of objectives

The objectives of this work included the following:

1. Characterize the thermal-hydraulic performance of metal foam heat exchangers under dry conditions, including the effects of foam pore size, base metal, fin depth, bonding method, and overall heat exchanger geometry.
2. Characterize the microstructure of the silica aerogels prepared using different solvents, catalysts, drying processes, and aging.
3. Establish the adsorption and desorption behavior of silica aerogels under equilibrium and transient conditions and obtain the data necessary to design dehumidification systems using these materials.
4. Develop an effective procedure for coating of metal foams with aerogels.
5. Develop a mathematical model for combined heat and mass transfer in aerogel-coated metal foams.

6. Quantify adsorption/desorption behavior of the coated metal foams and assess the feasibility of constructing a full-scale dehumidification system based on this new technology.

1.3.3 Summary of the thesis

The thermal-hydraulic performance of metal foam heat exchangers is discussed in Chapter 2. Pressure drop and heat transfer data for the bare substrate surface provides information for the suitability of metal foams to be used as substrates.

The adsorption and desorption performance of silica aerogels is presented in Chapter 3. The mass diffusivity and adsorption/desorption isotherms have been determined; the results are used to investigate the dehumidification performance of silica aerogels as desiccants

The adsorption and desorption performance of aerogel coated metal foams are explored in Chapter 4. The mass diffusion coefficients and equilibrium isotherms are determined for the deployed aerogel, in order to evaluate the effect of better thermal conductivity and higher surface area provided by the metal foam substrate.

A simultaneous heat and mass transfer model to predict the adsorption/desorption performance of a silica aerogel coated metal foam device for dehumidification applications is developed in Chapter 5.

A brief summary of the research, including the rate of moisture removal by a dehumidification device consisting of metal foams coated with silica aerogels, is provided in Chapter 6.

1.4 References

[1.1] ASHRAE, 2009, ASHRAE Handbook – Fundamentals (SI Edition), ASHRAE, Atlanta, GA.

[1.2] X. Han, Q. Wang, Y. Park, C. T'Joen, A. Sommers, A.M. Jacobi, A review of metal foam and metal matrix composites for heat exchangers and heat sinks, Heat Transfer Engineering 133 (2012) 991-1009.

[1.3] P. Mazzei, F. Minichiello, D. Palma, HVAC dehumidification systems for thermal comfort: a critical review, Applied Thermal Engineering 25 (2005) 677–707.

[1.4] J. Ling, Y. Hwang, R. Radermacher, Theoretical study on separate sensible and latent cooling air-conditioning system, International Journal of Refrigeration 33 (2010) 510-520.

[1.5] Y. Yadav, Vapor-compression and liquid-desiccant hybrid solar space-conditioning system for energy conservation, Renewable Energy 6(7) (1995) 719-723.

[1.6] Y. Dai, R. Wang, H. Zhang, J. Yu, Use of liquid desiccant cooling to improve the performance of vapor compression air conditioning, Applied Thermal Engineering 21 (2001) 1185-1202.

[1.7] Q. Ma, R.Z. Wang, Y.J. Dai, X.Q. Zhai, Performance analysis on a hybrid air-conditioning system of a green building, Energy and Buildings 38 (2006) 447-453.

[1.8] T. Katjanekarn, S. Kumar, Performance of a solar-regenerated liquid desiccant ventilation pre-conditioning system, Energy and Buildings 40 (2008) 1252-1267.

[1.9] P. Dhar, S. Singh, Studies on solid desiccant based hybrid air-conditioning systems, Applied Thermal Engineering 21 (2001) 119-134.

[1.10] C. Jia, J. Dai, J. Wu, R. Wang, Analysis on a hybrid desiccant air-conditioning system, Applied Thermal Engineering 26 (2006) 2392-2400.

[1.11] K. Ghali, Energy savings potential of a hybrid desiccant dehumidification air conditioning system in Beirut, Energy Conversion and Management 49 (2008) 3387-3390.

[1.12] W. Casas, S. Schmitz, Experience with a gas driven desiccant assisted air conditioning system with geothermal energy for an office building, Energy and Buildings 37 (2004) 493-501.

[1.13] C. Ahmed, P. Gandhidasan, S. Zubair, A. Al-Farayedhi, Exergy analysis of a liquid-desiccant-based hybrid air-conditioning system, Energy 23 (1998) 51-59.

[1.14] J. Ling, O. Kuwabara, Y. Hwang, R. Radermacher, Experimental evaluation and performance enhancement prediction of desiccant assisted separate sensible and latent cooling air-conditioning system, International Journal of Refrigeration 34 (2011) 946-957.

[1.15] A.A. Zadpoor, A.H. Golshan, Performance improvement of a gas turbine cycle by using a desiccant-based evaporative cooling system, Energy 31 (2006) 2652-2664.

[1.16] R. Lazzarin, Introduction of a simple diagram-based method for analyzing evaporative cooling, Applied Thermal Engineering 27 (2007) 2011-2025.

[1.17] J. Jeong, S.A. Mumma, Practical thermal performance correlations for molecular sieve and silica gel loaded enthalpy wheels, Applied Thermal Engineering 25 (2005) 719-740.

[1.18] C.E.L. Nobrega, N.C.L. Brum, Modeling and simulation of heat and enthalpy recovery wheels, Energy 34 (2009) 20632068.

Chapter 2- Thermal-hydraulic performance of metal foams

2.1 Introduction

Recent advances in manufacturing techniques have made possible a broader use of metal foams and metal matrix composites (MMCs) for heat transfer applications. They are characterized by the size of the windows (or pore diameter) which correlates to the nominal pore density (usually as pores per inch-PPI), the strut diameter and length, and the porosity ε (volume of void divided by the total volume of the solid matrix and void). Some of the length scales for metal foams are defined in Figure 2.1.

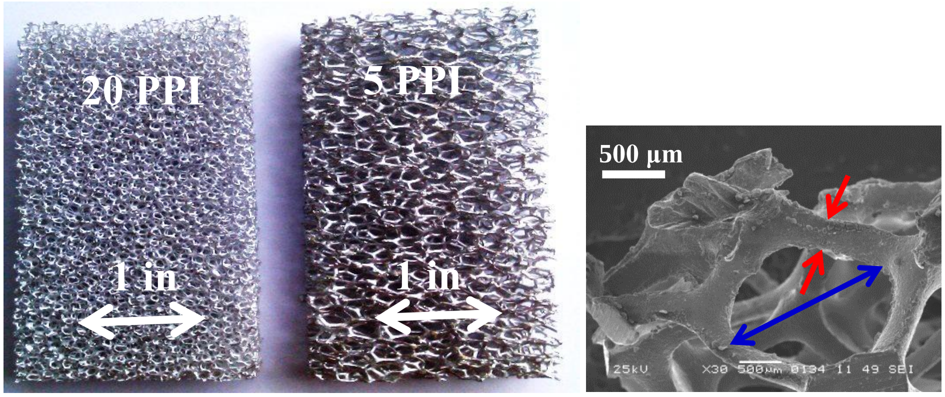

(a) **(b)**

Figure 2.1 Definition of length scale for metal foams (a) 20 and 5 PPI (b) Pore diameter (blue), strut diameter (red)

Metal foams have attractive properties for heat transfer applications and have been used for thermal applications in cryogenics, combustion chambers, geothermal systems, petroleum reservoirs, catalytic beds, compact heat exchangers for airborne equipment, air cooled condensers and compact heat sinks for power electronics. Despite manufacturing and implementation issues, these materials hold promise both for heat exchangers and heat sinks

[2.1]. Large porosity ($\varepsilon > 0.90$), low relative density, high thermal conductivity of the cell edges, large accessible surface area per unit volume, and the ability to mix the cooling fluid contribute to making the metal foam thermal management devices efficient, compact, and light-weight. If metal foams are to be widely used in thermal systems, their pressure-drop and heat transfer characteristics must be available to potential users in terms that fit into the current design methods. This paper focuses on the experimental analysis of pressure drop and heat transfer for air flow in metal foams heat exchangers with different pore size, geometry and base metal.

2.2 Literature review

2.2.1 Pressure drop in metal foams

Metal foams are a relatively new class of materials. Due to their recent emergence and complex structure, they are not yet completely characterized. Interest in using them in contemporary technologies makes the need for fully characterizing them more urgent. Central to this need is an accurate evaluation of the flow characteristics to assist in making the trade-off analysis between the increased heat transfer and the associated increase in the pressure drop for foam heat exchanger and heat sink designs. Extensive reviews of the topic of the fluid flow in the porous media in general can be found in the open literature [2.2–2.4].

Different experimental and analytical studies have been conducted to characterize the fluid flow in a porous matrix on the basis of macroscopically measurable flow quantities. Darcy established the well-known Darcy's law [2.5] which states that the pressure-drop per unit length for a flow through a porous medium is proportional to the product of the fluid velocity and the dynamic viscosity and inversely proportional to the permeability ($\Delta P/L = \mu V/K$). Though this correlation is frequently used for various flow problem through porous media (*e.g.* flow through soil), however it is applicable only when the permeability based Reynolds number is very small

($Re_K = \rho V \sqrt{K} / \mu < O(1)$). As the Re_K for the flow through metal foams are of the order 10 or 100, conventional Darcy flow model can not be directly used to predict the pressure gradients.

Seguin *et al.* [2.6] experimentally investigated the flow regimes in various porous media. The onset of the turbulent flow regime was found to occur at a Reynolds number equal to 470. The Reynolds number was defined based on the pore diameter of metal foams. Lage *et al.* [2.7] reviewed Darcy's Law [2.5] and modified it for the flow through metal foams. They argued that the ratio between the form and the viscous forces should be used to mark the transition from the linear to the quadratic flow regimes of the pressure drop behavior. They concluded that the transition is material specific and depends on the internal geometry of the porous medium. Crosnier *et al.* [2.9] studied air flow through 20 and 40 PPI[1] aluminum foam and 20 PPI stainless steel foam. The porosities of all foam samples were above 90%. The transition from the laminar to the turbulent regime took place at a Darcian velocity of about 1m/s. Tadrist *et al.* [2.10] investigated the use of aluminum foam with high porosity (above 90 %) for compact heat exchangers. They experimentally determined permeability and friction coefficients and used an Ergun-type [2.8] relation between the pressure gradient and the velocity in the foam.

Bhattacharya *et al.* [2.11] determined the values for the permeability and the friction coefficient for aluminum foam experimentally. Experiments covered porosities from 90 to 98% and pore densities of 5, 10, 20, and 40 PPI. Permeability increased with the pore diameter and porosity, while the friction coefficient depended only on the porosity. Boomsma *et al.* [2.12] modeled the flow through aluminum foam using a periodic unit of eight cells. They concluded that the pore diameter was a more practical scale to determine the Reynolds number compared to the empirically determined permeability for metal foams.

---

[1] Pore size is commonly given in pores per inch, designated as PPI.

Naakteboren *et al.* [2.13] investigated the entrance/exit effects on the pressure drop analytically and numerically using analogies between flow through slotted plates placed along a flow channel and the flow through porous media. They concluded that for a porous medium with length greater than one hundred times the pore size, the core pressure (due to the porous medium) dominated, and the entrance/exit effects could be ignored. Innocentini *et al.* [2.14] studied the effect of both sample thickness and the sample fixture on the pressure drop in nickel–chromium foam. The effect of thickness on the pressure drop was found to be quite small when the data were compared for different samples at various face velocities.

2. 2.2 Heat transfer in metal foams

Metal foams are anticipated to have relatively large pressure drop per unit length with a large heat transfer coefficient. This expectation is reinforced by the complex geometry of the foams which results in a high degree of boundary layer restarting and wake destruction by mixing. Over the past few decades, many researchers have studied the heat transfer characteristics of porous media. Zhao [2.15] reviewed the literature related to the thermal transport in metal foams. The study covered effective thermal conductivity, forced convection, natural convection, thermal radiation, pool boiling and flow boiling heat transfer, solid/liquid phase change heat transfer and catalytic reactor. He concluded that most of the research treated the metal foam as one type of effective continuous porous media and only a few studies investigated the detailed thermal behavior at the pore level. Ribeiro *et al.* [2.16] investigated the use of copper foams for small-scale refrigeration systems. Experiments were performed with microchannel condensers using foams with different porosities (0.893 and 0.947) and pore sizes (10 and 20 PPI). They concluded that the pore size of the metal foam was the most influential parameter in determining the air-side heat transfer rate and pressure drop of the metal foam condensers.

Calmidi and Mahajan [2.17] characterized the heat transfer behavior of different aluminum foams samples using a wind tunnel. The experiments were conducted by heating the base of the foam and using air as the cooling fluid. Based on the geometry of the foams, they developed a correlation to predict the thermal performance of the foams. Younis and Viskanta [2.18] presented an experimental investigation to characterize the volumetric heat transfer coefficient between a heated air stream and ceramic foams (alumina and cordierite) by using transient single-blow technique. Dukhan and Chen [2.19] presented heat transfer measurements inside rectangular blocks of commercially available aluminum foam subjected to constant heat flux at one side and cooled by air. The temperature profile in the foam decayed exponentially with distance from the heated base. Dai *et al.* [2.20] reviewed the mechanistic basis of the Boomsma-Poulikakos model [2.21] to predict the thermal conductivity of the aluminum foams, correcting it and providing an extension to account for ligament orientation. The new model provided more accurate predictions of effective thermal conductivity.

In an application study based on their prior work, Dai *et al.* [2.22] compared the heat transfer and pressure drop performance of metal-foam heat exchangers to another state-of-the-art heat exchanger. In the analysis, two heat exchangers were subjected to identical performance requirements, and the resulting volumes, masses, and costs were compared. Metal foam heat exchangers were found to meet the thermal requirements at lower volume and mass, but at a higher cost. Nawaz *et al.* [2.23] considered open-cell aluminum metal foam as a highly compact replacement for conventional fins in heat exchangers. Heat transfer and pressure drop data for a 10 PPI metal foam heat exchanger were evaluated by wind-tunnel experiments in order to make the comparison with the louver-fin heat exchangers. Moffat *et al.* [2.24] showed that three parameters must be known to calculate the heat transfer performance of a foam-fin: the convective conductance per unit volume, the effective conduction as a fin, and the effective thermal resistance between the foam and the surface to which it was attached. They developed a new test method, which, in conjunction with transient single-blow test, allowed all three parameters to be measured using one specimen.

In the current study, experimental results are presented for air flowing through a spectrum of commercially available metal foams. Based on the experiments, a model for predicting the pressure drop and heat transfer in metal foams is developed using easily measurable parameters. The pressure drop model assumes an Ergun-type dependence of the permeability on the porosity and relies on experiments to determine important transport parameters. The experimental data and thermal-hydraulic correlations provide key information needed for computing the pumping power and air side heat transfer rate for metal foam heat exchanger design, optimization and comparison to other heat exchangers.

2.3 Experimentation

2.3.1 Experimental apparatus and methods

A closed-loop wind tunnel apparatus was used to investigate the thermal-hydraulic performance of metal foam heat exchangers. As shown in the schematic of wind tunnel (Figure 2.2), air downstream of test section passed through a set of electric strip heaters, past a steam injector, through an axial blower and another set of strip heaters, a flow nozzle, a mixing chamber, a flow conditioning section, a flow contraction, and the test section, completing the loop. The heaters and steam injector were used to maintain the desired upstream air temperature and dew point at steady state. The air temperature was measured using thermocouple grids constructed using T-type thermocouples (4 channels upstream; 9 channels downstream), and chilled-mirror hygrometers were used to measure the upstream and downstream dew points. The cross-sectional flow area in the test section was rectangular, 30 cm wide and 20 cm high. An axial blower provided an air flow with face velocities at the test section ranging from 0.3 to 7m/s. An ASME flow nozzle (Inlet diameter=11 inches, throat diameter=6 inches), with a differential pressure transducer, was used to measure air mass flow rate. Another pressure transducer was used to measure air-side pressure drop across the test section. For the determination of mas flow rate and face velocity a hot-wire anemometer was also used along with the ASME nozzle. A single-phase liquid, an aqueous solution of ethylene glycol (DOWTHERM 4000), was used as the tube-side heat transfer fluid. A chiller system with a commercial heat pump, two large coolant reservoirs, a PID-controlled electric heater, and a gear pump supplied the flow. The chiller system provided a coolant flow with a steady inlet temperature (within 0.1°C) at a capacity up to 20 kW. Coolant inlet and outlet temperatures were measured using RTDs.

Coolant flow mixing devices were installed immediately upstream of the RTDs to provide a well-mixed coolant temperature. A Coriolis-effect flow meter located in the downstream coolant pipe was used to measure mass flow rate. A computer-based data acquisition system (National Instruments) was used to record and monitor the experimental data. The relevant experimental uncertainties involved in the wind-tunnel experiments are given in Table 2.1.

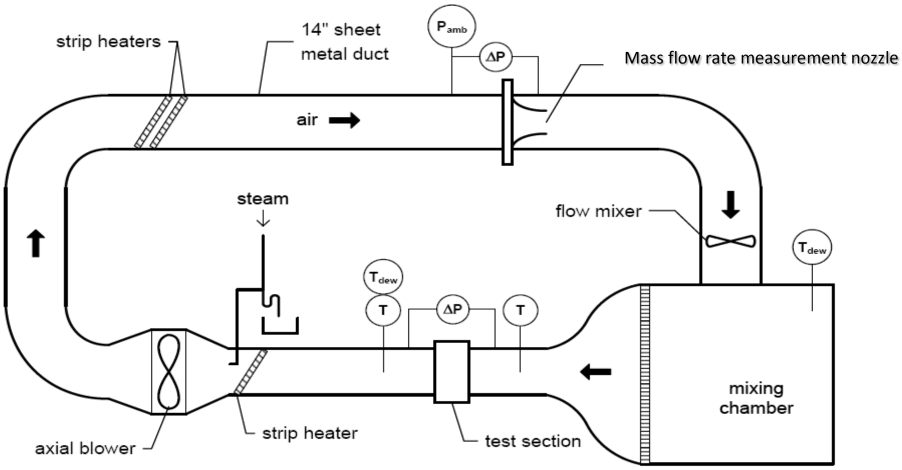

Figure 2.2 Closed loop wind tunnel

Table 2.1 Uncertainty of parameters involved in experiments.

Parameter	Uncertainty
Air temperature	±0.1°C
Coolant temperature	±0.03°C
Nozzle discharge coefficient	±2%
Core pressure drop	±0.17Pa
Nozzle pressure	±0.087Pa
Coolant mass flow rate	±0.1% of reading
Dew point	±0.2°C
Face velocity	±0.1m/s
Pressure drop(micro manometer)	±0.2Pa

The entire wind tunnel, the test specimen, and coolant pipes were all insulated to isolate the system from the environment. Steady-state conditions were considered to prevail when all individual variables measured were maintained constant within instrument uncertainty. The data stream was sampled for a period long enough to ensure that the averaged readings were independent from random instrument errors). All experiments were conducted under dry conditions and had an energy balance ($2|Q_{air} - Q_{coolant}|/(Q_{air} + Q_{coolant})$, ANSI/ASHRAE-33) within 5% when the face velocity was greater than 1.5m/s, and within 7.5% when it was smaller than 1.5m/s. Coolant flow rate was constant at 0.082kg/s, while the range for inlet coolant temperate was 17^{o}C to 23^{o}C. The inlet air temperature varied in the range of 31^{o}C to 37^{o}C. The relative humidity was maintained at 40% during all experiments.

2.3.2 Specimen preparation

Metal foam heat exchangers were built in different confrigurations. Three different methods were used to join the metal foam to the tubes including thermal epoxy (Artic silver 5), thermal compound, and brazing. A representative sample with the 10PPI metal foam is shown in Figure 2.3. All samples to compare the effect of pore size were prepared with same confriguration while deploying foams with different pore sizes (5, 10, 20 and 40PPI). Specifications and dimensions of samples (shown in Figure 3) are presentaed in Table 2.2.

Figure 2.3 Flat tube metal foam heat exchanger (10 PPI metal foams)

Table 2.2 Design specifications of heat exchangers for comparison of effect of porosity

Base metal	Al 6061 alloy
Porosity	5, 10, 20, 40 PPI
Tube side configuration	Microchannel flat-tube (1.5 mm × 1.5 mm) 8 channels
Number of fins	10
Fin depth	15 mm
Fin thickness	15 mm
Bonding method	Artic silver epoxy (*k=4.5 W/m-K*)
Face area	200 mm × 174 mm
Tube width	25.4 mm
Tube wall thickness	0.5 mm

2.3.3 Data reduction method

The Hazen-Dupuit-Darcy (widely known as the Forchheimer) equation was used to relate the pressure drop to the face velocity in the metal foams:

$$\frac{\Delta P}{L} = \frac{\mu}{K} V + \rho C V^2 \tag{2.1}$$

It is important to note that both permeability (K) and inertia coefficients (C) are empirical constants and depend on the structure of the porous medium. Equation (2.1) can be used to analyze the pressure drop data. In the current study the velocity was always sufficiently high to ensure all data were well into the Forchheimer regime (0.5m/s -10m/s), and was low enough to ignore the compressibility effects [2.7].

In order to evaluate the thermal performance, the heat transfer modeling was undertaken to account for fin-efficiency and local mixing-cup temperature effects. The total rate of heat transfer, q, was determined from an energy balance on each stream, and the modeling relied on an overall approach, as does all the prior work cited. Namely, for a metal foam heat exchanger operating under dry-surface conditions:

$$q = UA \cdot LTMD \tag{2.2}$$

where

$$LMTD = F\,\frac{(T_{air,in} - T_{coolant,out}) - (T_{air,out} - T_{coolant,in})}{\ln\left(\dfrac{T_{air,in} - T_{coolant,out}}{T_{air,out} - T_{coolant,in}}\right)} \tag{2.3}$$

The *LMTD* was determined from the measured temperatures, with the flow configuration factor, *F*, from Incropera and Dewitt [2.25]. The overall thermal conductance of the heat exchanger, *UA*, was formulated by neglecting the conduction resistance of the tube wall:

$$\frac{1}{UA} = \left(\frac{1}{\eta_o A h}\right)_{air} + \left(\frac{1}{Ah}\right)_{coolant} + R_{bond} \tag{2.4}$$

The coolant-side convection coefficient was determined for the in-tube single-phase flow during the experiments, based on the geometry and flow (there were no coolant-side fins). The thermal contact resistance due to bonding of the foam to the tubes, R_{bond}, was determined from ancillary experiments, in which it was found that the total air-side resistances for different bonding methods were 20, 45 and 80 K/W for brazing, thermal compound and thermal epoxy (artic silver) respectively. These values were obtained from the experiments performed on geometrical similar samples (Foam pore size, face area and flow depth) under same test conditions (inlet air temperature, inlet coolant temperature, face velocity *etc.*). The thermal conductivity and thickness of the bond was included in the analysis to determine the total air-side thermal resistance. The temperature variations in the air-side metal foam fins were accounted for using the surface efficiency

$$\eta_o = 1 - \frac{A_{foam}\left(1 - \eta_f\right)}{A_{foam} + \varepsilon A_{base}} \tag{2.5}$$

The surface area of the foam for air-side convection, A_{foam}, was determined from manufacturer's data for foam surface area per unit volume. The surface area per unit volume (Figure 2.4) was calculated based on the geometry of the foam and was verified using the multipoint BET method by the adsorption of krypton gas at cryogenic temperatures (less than -150°C). Relative density in Figure 2.4 represents the density of foam relative to the density of base metal (density of aluminum 6061 alloy is 2700 kg/m^3).

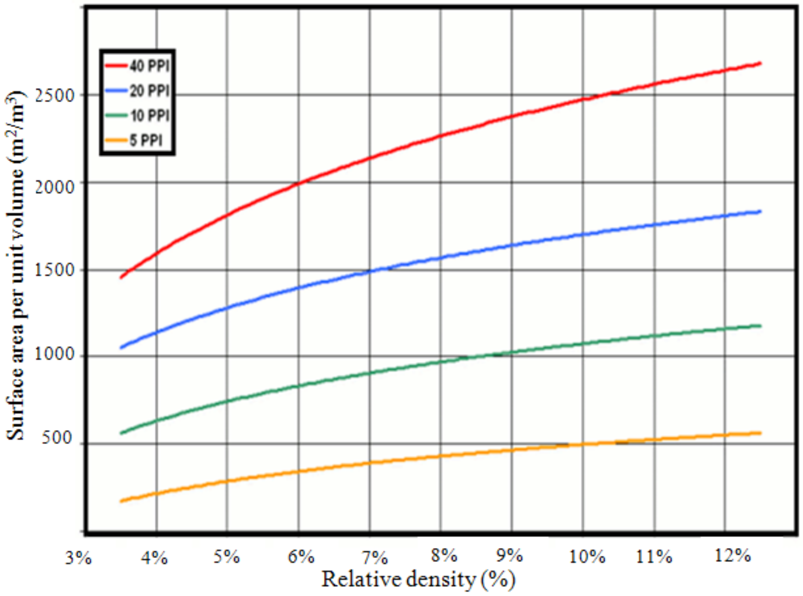

Figure 2.4 Surface area to volume ratio for metal foams (*ERG Corporation*, USA)

The fin height, L_f, was taken as half the tube spacing. The fin efficiency was then calculated assuming a straight fin with an adiabatic tip, following Dai *et al.* [2.22]:

$$\eta_f = \frac{\tanh(m_{foam} L_f)}{m_{foam} L_f} \tag{2.6}$$

where the fin parameter m_{foam} accounted for the ligament and pore diameters, D_f and D_p, respectively,

$$m_{foam} = \sqrt{3\pi D_f h / (D_p^2 k_{eff})} \tag{2.7}$$

and the effective thermal conductivity of the foam was taken as the solid-only effective thermal conductivity [2.20]:

$$k_{eff} = (1-\varepsilon)k_{solid} / 2 \tag{2.8}$$

2.4 Results

The pressure drop and the heat transfer rate are used to characterize the heat exchanger performance. These parameters determine the fan power and size requirements of the heat exchanger. Both pressure drop and thermal performance are affected by a number of parameters such as the geometry of heat exchanger, metal foam characteristics and flow conditions.

2.4.1 Pore size of metal foam

The pore size is an important characteristic of metal foams. Most of manufacturers use PPI to characterize the size of the pores in metal foams. The results for the pressure drop per unit length are plotted against the face velocity under dry surface conditions in Figure 2.5a. As demonstrated by the figure, the pressure drop per unit length increases with an increase in PPI (a decrease in pore size). The 5 PPI foam, with a pore size of about 4 mm, shows the smallest pressure drop for all face velocities, while the 40 PPI foam, with pore size of about 1.8 mm results in the highest pressure drop. An interesting finding is how the pressure gradient depends on pore size. Based on the SEM image analysis to quantify the foam geometry, the pore size differs by about 30% between the 5 PPI and 10 PPI foams (determined by SEM image analysis, Table 2.6), and the pressure gradient increases by roughly 15 to 20 percent at high velocities. At velocities below about 3m/s, the difference is negligible. However when the pore size becomes smaller the pressure gradient shows an obvious difference even for small face velocities, as can be observed in Figure 2.4a. While reducing the data for the pressure gradients, the effect of flat tubes between metal foam fins was neglected; their contribution to pressure drop was very small compared to the porous metal foam. The heat transfer coefficients based on the total surface area (base area and foam surface area) are presented in Figure 2.5b. As the data were normalized based on the total air-side surface area, the effect of surface area per unit volume was accounted for. The heat transfer coefficient also depends on the flow conditions. The heat transfer coefficient increases with velocity for foams of all pore sizes at almost same rate. Heat transfer coefficients as high as 400W/(m$^{2\cdot}$K) can be achieved with a 40PPI metal foam heat exchanger when the face velocity is about 6m/s. This number is about twice the heat transfer coefficient achieved by compact louver-fin heat exchangers under the same flow conditions. It is not only surface area which contributes to larger heat transfer rate; small pore diameters imply more ligaments per unit volume, and more ligaments promote flow mixing.

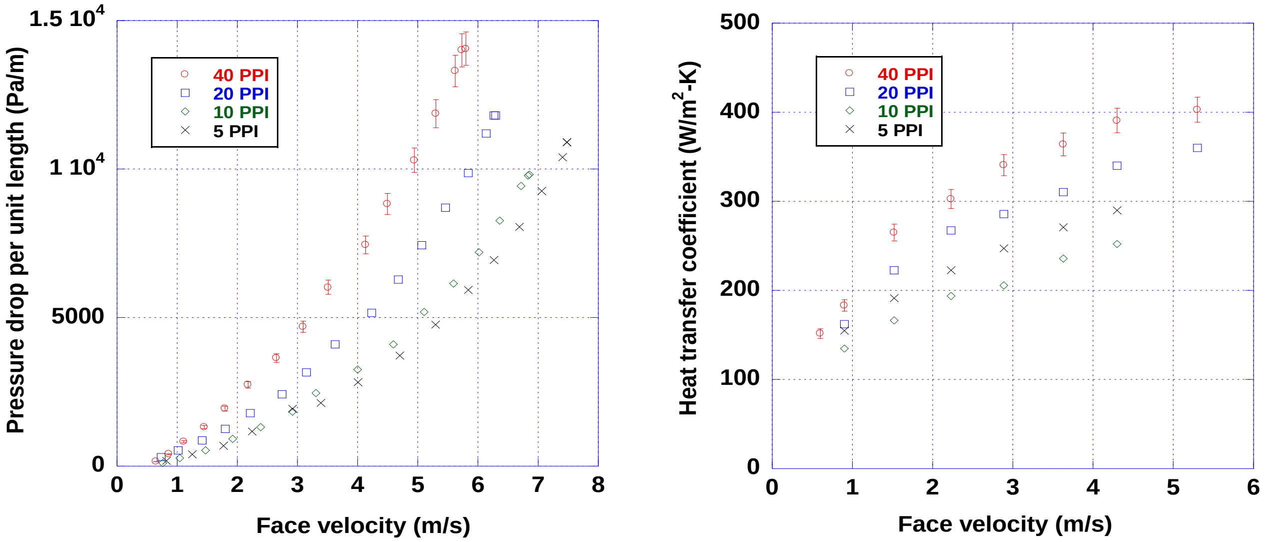

(a) (b)

Figure 2.5 Effect of pore size on (a) pressure drop per unit length (b) heat transfer coefficient

2.4.2 Geometry of heat exchanger

As pointed out in the introduction one important concern regarding the use of metal foam in heat transfer applications is the relatively large pressure drop. Seeking an improvement in the hydraulic performance of metal foams, alternative geometric configurations of the metal foam were explored. In undertaking new deployments, face area, volume, and mass were constraints. A relative comparison is presented, where the deployment geometry affects the performance of the heat exchanger by changing the pressure drop. There were two round-tube heat exchangers used in this comparison, and they had identical face areas (200mm×200mm) and flow depths (25mm). Sample 1 had a continuous block deployment of foam, with round tubes running through the foam block. Sample 2 had an annular metal foam layer on the round tubes (Figure 2.6). The thickness of the annulus of metal foam was such that there was no bypass of flow; i.e., the outer surface of the annulus of metal foam on one tube touched the outer surface of the annulus of foam on the neighboring tube. The pressure drop data for the two round-tube foam heat exchangers are presented in Figure 2.7a. It is obvious at relatively low face velocity (less than 1.5m/s) pressure gradients for both samples were comparable but at larger face velocities, the sample with a continuous metal foam block had a higher pressure drop compared to the annular foam configuration. The total air side heat transfer (at fixed flow rate and inlet temperatures) for both configurations is shown in Figure 2.7b. Although Sample 1 had a slightly larger heat transfer rate, the values do not differ much. Furthermore the weight of Sample 2 was almost half that of Sample 1(0.60 kg for (a) vs. 0.34 kg for (b))

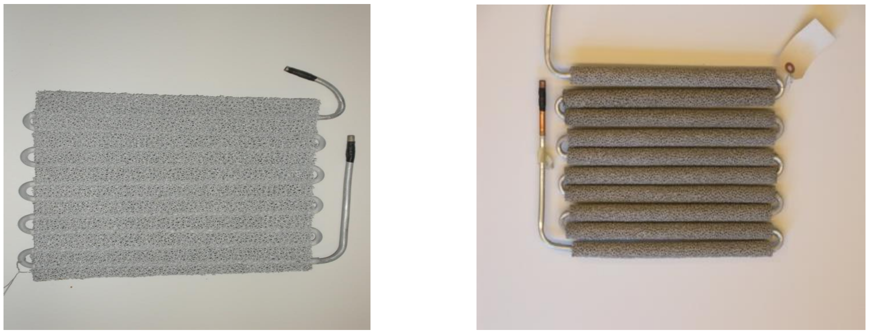

(a) (b)

Figure 2.6 Metal foam heat exchangers with different geometry

(a)Sample 1-continuous block structure (b) Sample 2-Annular structure

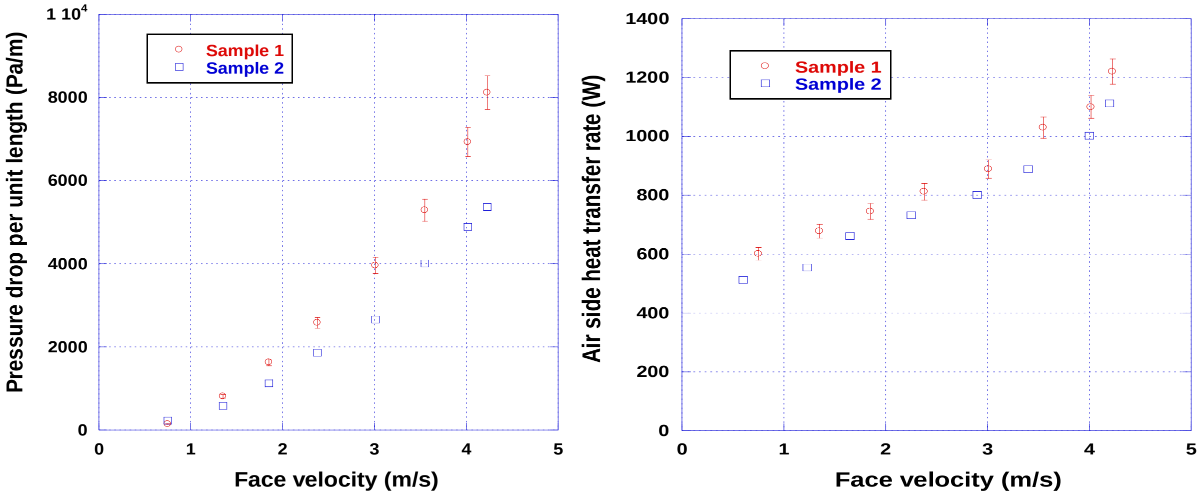

(a) (b)

Figure 2.7 Effect of heat exchanger geometry on (a) pressure drop per unit length (b) air-side heat transfer rate

These comparisons show that the higher pressure drop associated with metal foams can be mitigated by judicious deployment of the metal foam, so that the heat transfer performance remains excellent, and the fan power requirements are reduced.

2.4.3 Base metal of the foam

Most of the metal foams used in heat transfer applications are made of aluminum or copper. The thermal conductivity of copper is larger than that of aluminum. If the base metal used to manufacture metal foam has larger thermal conductivity, the resulting heat transfer rate will be larger. In order to explore base-metal effects, two samples of the same geometry with differing base metals were constructed (frontal area (200mm×200mm), flow depth (25mm), number of tubes turns (10) (see Figure 2.8). The thermal performance of two heat exchangers is compared in Figure 2.9. Sample 1 had copper as the base metal for the metal foam, with copper tubes passing through annular fins. Sample 2 was manufactured from an aluminum alloy. Sample 1 showed much better performance, as the heat transfer rate was increased by almost 40%. For both samples the heat transfer rate increased as the face velocity increased, and the rate of increase was nearly identical. This behavior confirms that the only difference between the performances of two samples is due to the difference in thermal conductivity of the metal foam. It is important to note that the thermal conductivity of 20PPI copper foam is about 15W/m-K while for 20PPI aluminum foam it is about 8W/m-K). The thermal hydraulic performance is affected by the porosity and geometry in exactly the same way for the copper foam heat exchanger as for the aluminum foam heat exchanger. It is important to note that the both foam type (20PPI) had the same pore and ligament diameters ($d_f=0.36\pm0.05mm$, $d_p=2.54\pm0.05mm$ for aluminum foam and $d_f=0.35\pm0.05mm$, $d_p=2.56\pm0.05mm$ for copper foam determined by SEM image analysis). One important factor to consider is the cost of the base metal as the cost of the foam is directly related to the base metal cost. Based on the Wall-Streeter Journal (August 2013) the cost of copper (C10100) was approximately 4 times the cost of aluminum alloy (6061).

(a) (b)

Figure 2.8 Metal foam heat exchangers with different base material (a) copper (b) aluminum

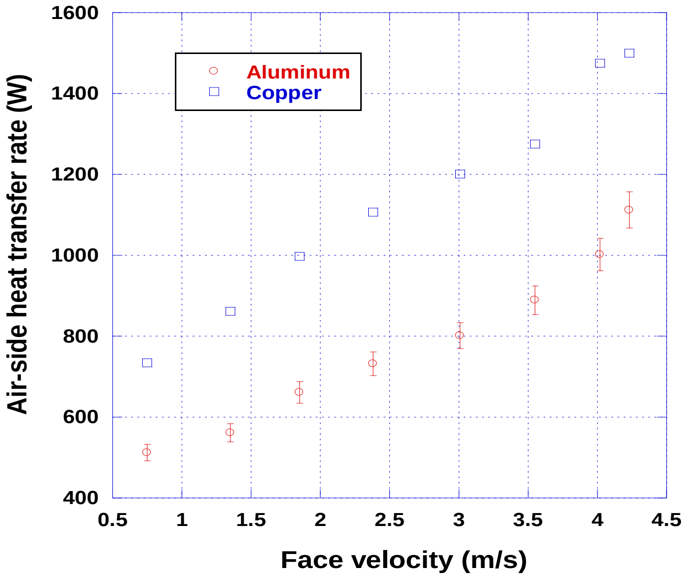

Figure 2.9 Heat transfer for samples with different base metal

2.4.4. Comparison to louver-fin heat exchangers

The ultimate goal in heat exchanger design is to minimize cost. Thermal hydraulic performance is directly related to operating cost, so a good heat exchanger design should give the maximum heat transfer rate with the minimum pressure drop. Geometry, base metal and fin configuration all affect the performance. In order to evaluate metal foam heat exchanger performance for HVAC&R applications, a comparison to louvered-fin performance was undertaken. A state-of-the-art louvered fin design was adopted for the comparison (Figure 2.10);

its characteristics are presented in Table 2.3 (Park and Jacobi, Sample 1 [2.26]). The comparison considers 10 PPI aluminum metal foam as a “drop-in” replacement for the louvered fins. Obviously, this deployment of metal foam is not expected to be optimal; however, this approach allows a comparison with as few design changes as possible. The performance of the metal foam heat exchanger is compared to the louver fin heat exchanger in Figure 2.11. Under all flow conditions the metal foam heat exchanger performed much better than the louver-fin configuration for the same volume of the device. Such a comparison confirms that metal foam can replace conventional materials for HVAC&R heat transfer applications.

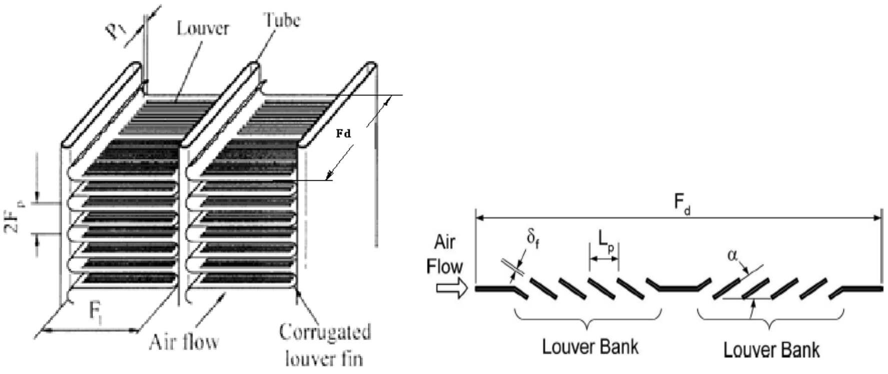

Figure 2.10 Louver fin heat exchanger geometry [2.26]

Table 2.3 Characteristics of louver-fin design [5.26]

L_p (mm) Louver pitch	**F_p (mm)** Fin pitch	**F_l (mm)** Fin length	**L_l (mm)** Louver length	**α (deg)** Louver angle	**F_d (mm)** Fin width	**T_p (mm)** Tube pitch	**δ_f (mm)** Fin thickness
1.38	1.4	12.43	11.15	44	25.4	14.26	0.24

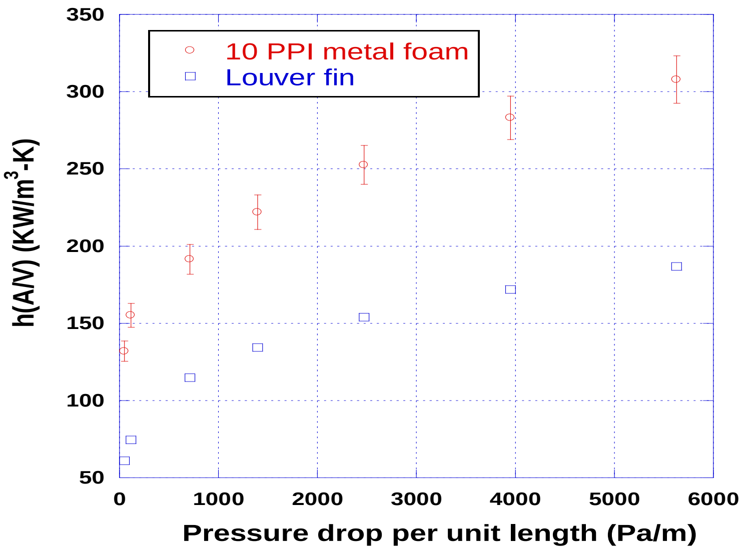

Figure 2.11 Comparison of 10 PPI metal foam to louver-fin heat exchanger

2.5 Thermal hydraulic model development

There has been tremendous effort to quantify the thermal-hydraulic behavior of porous media, such as metal foams. For the pressure drop, the conventional approach is based on defining the parameters such as permeability and inertia coefficient by curve fitting the pressure drop data. While this approach is widely adopted, it fails to completely capture the physics reflected in the data. A better approach appears to be to reduce the data based on the pore diameter or the hydraulic diameter of specimen and present the results as curve fits in dimensionless space as explained later. Similarly, for the heat transfer the conventional approach is based on a model developed by considering the flow through metal foam as a flow through an array of cylinders. An alternative approach is to resort to pure empiricism.

2.5.1 Existing thermal-hydraulic models

As discussed earlier, many researchers have tried to generalize and modify the Darcy model for flow through porous media to predict the pressure-drop performance of metal foams. Such models were found to work well for a certain, narrow range of flow conditions but cannot be used to predict the performance over the range of the current experiments. As an example, experimental results for pressure drop of a 40 PPI metal foam are compared to the modified Darcy model of Bhattacharya *et al*. [2.11] in Figure 11a. The model of Bhattacharya *et al*. [2.11] is given as Equation (2.9):

$$-\frac{dp}{dx}=\frac{\mu V}{K}+\frac{\rho \bar{C}}{\sqrt{K}}V^2 \qquad (2.9)$$

In Equation (2.9), K is the permeability, and $\bar{C}$ is a dimensionless inertia coefficient. As shown in Figure 2.12a, the model makes reasonable predictions at the lowest velocities for 40 PPI aluminum foam, but it under predicts pressure drop by as much as 40% at intermediate velocities.

Similar to pressure drop, there are numerous models available in the open literature to predict the heat transfer performance for flow through porous media. Equation (2.10) was developed by Calmidi and Mahajan [2.17] to predict the heat transfer coefficient based on the foam properties such as conductivity, ligament diameter, *etc*.

$$h=\left(\frac{k_{fluid}}{D_f}\right)0.52\,\mathrm{Re}_{Df}^{0.5}\,\mathrm{Pr}^{0.37} \qquad (2.10)$$

The ligament diameter, D_f, is considered as the characteristic length, and k_{fluid} is the fluid thermal conductivity. Experimental results are compared to values predicted by this relationship for a 40 PPI metal foam sample in Figure 2.12b. Although the model is widely used to predict the heat transfer coefficient for foams, it does not provide accurate predictions of the current data. A possible source of error is a flaw in the assumed geometry: the model considered metal foam ligaments as stack of small cylinders, either in cross-flow or parallel-flow orientation. This is not the case in reality (see Figure 2.13).

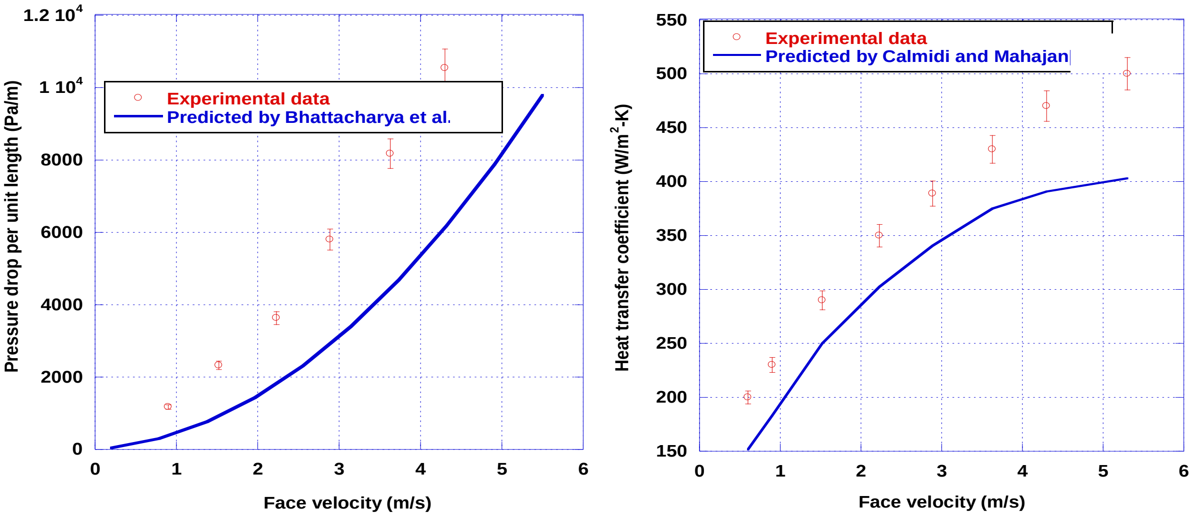

(a) **(b)**

Figure 2.12 Comparison of experimental data with (a) pressure drop [2.11] (b) heat transfer model [2.17] for 40 PPI sample.

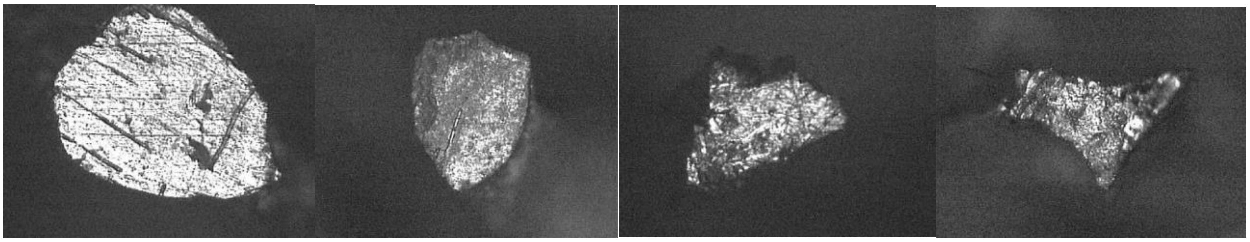

(a) $\varepsilon = 90.95\%$ *(b)*$\varepsilon = 92.01\%$ *(c)* $\varepsilon = 93.48\%$ *(d)* $\varepsilon = 97.85\%$

Figure 2.13 Metal foam ligament cross sectional view for different porosities [2.11]

2.5.2. Determination of permeability and inertia coefficient

Based on the modified Darcy flow model, the pressure gradient can be related to the hydraulic characteristic of the foam by Equation 2.1.This relation can be rearranged as

$$\frac{\Delta P_f}{LV} = \frac{\bar{\mu}}{K} + \bar{\rho}CV \tag{2.11}$$

Equation (2.11) provides a linear relationship in terms of face velocity,

$$\frac{\Delta P_f}{LV} = A + BV \tag{2.12}$$

$$A = \frac{\bar{\mu}}{K} \quad , \qquad B = \bar{\rho}C \tag{2.13}$$

These relations for A and B were used to determine the permeability and inertia coefficient for three different types of porous media. The results are summarized and compared to values from the literature in Table 2.4.

The values from experiments are of the same order of magnitude as those from the literature, but there are significant discrepancies. The final fit to pressure gradient has a correlation coefficient of R^2=0.99792. Thus, the parameters given in Table 2.4 can be used with Equation 2.1 to obtain good fits to the current data. However, a more general approach is explored in the next section.

Table 2.4 Permeability and inertia coefficient for porous media*

Porous media	K_{exp}(m^2)	C_{exp}(m)	$K_{Literature}$(m^2)	$C_{Literature}$ (m)
5 PPI Al	3.79±0.04(10^{-7})	0.132±0.005	2.70(10^{-7})	0.097
10 PPI Al	2.72±0.04(10^{-7})	0.095±0.004	1.49(10^{-7})	0.07
20 PPI Al	8.37±0.05(10^{-8})	0.082±0.004	1.42(10^{-7})	0.10
40 PPI Al	6.91±0.03(10^{-8})	0.086±0.003	5.68(10^{-8})	0.0899

* $K_{Literature}$ and $C_{Literature}$ are taken from Bhattacharya *et al.* [2.11].

2.5.3. Determination of friction factor *f* and colburn *j* factor

For comparison purposes and generality, the pressure-drop and heat transfer performance of the metal foam heat exchangers is presented following the convention of Kays and London [2.27], wherein the friction factor f and Colburn j factor are related to the Reynolds number based on hydraulic diameter. With some as yet determined length scale, L_c, as an additional characteristic length and $\bar{\rho}$ the average density. The relationship for friction factor can be represented as

$$f_{Lc} = \frac{\Delta P}{L} \frac{\bar{\rho}}{G^2} \frac{L_c}{2} \tag{2.14}$$

where G mass flux, $G = \bar{\rho} V_{\max}$, with $V_{\max}$ the velocity at the minimum free-flow area:

$$A_{\min} = \varepsilon A_{fr} \tag{2.15}$$

The characteristic length, L_c, can be defined by many ways. Some of the options follow:

- Heat exchanger characteristics: hydraulic diameter, flow depth, tube spacing
- Foam characteristics: pore diameter, ligament diameter, ligament length

The hydraulic diameter follows convention:

$$D_h = \frac{4 A_{\min} L}{A_T} \tag{2.16}$$

$$A_T = A_{base} + A_{foam} \tag{2.17}$$

The total surface area, A_T, is comprised of the exposed tube area, A_{base}, and the surface area of the metal foam, A_{foam}. Again, if D_h is used as L_c in Equation (2.14), then the conventional definitions of Kays and London prevail [2.27], and we expect f=function (Re_{Dh}).Where Re_{Dh} is the Reynold number based on the hydraulic diameter of the heat exchanger. In the approach embodied in equations (2.14) to (2.17), that convention need not be followed. However, the geometric parameters must be known.

In order to determine A_{min}, image processing technique was used, rather than simply relying on the reported porosities. Images from X-ray tomography [2.28] were analyzed as suggested in Figure 2.14. In order to identify the metal in the cross sectional view of foam, a pixel threshold value of 100 was set, with pixel values ranging from 0 (black) to 255 (white). Threshold was set based on the common practice used in Histogram-shaped based method for image processing. The minimum flow areas calculated by the image analysis (threshold=100) agreed well with the method reported in the literature ($A_{min} = \varepsilon A_{front}$).Later when the results were compared with a threshold value of 125, the minimum flow area decreased by 3%.

Similarly for a threshold value of the 75, the minimum area was increased by about 2%. The number of pixels exceeding this threshold divided by the total gave $A_{\mathrm{min}}/A_{\mathrm{fr}}$. The process was repeated for five images for each type of foam and the values were averaged. The results are given in Table 5, and other geometric properties are reported in Table 2.6.

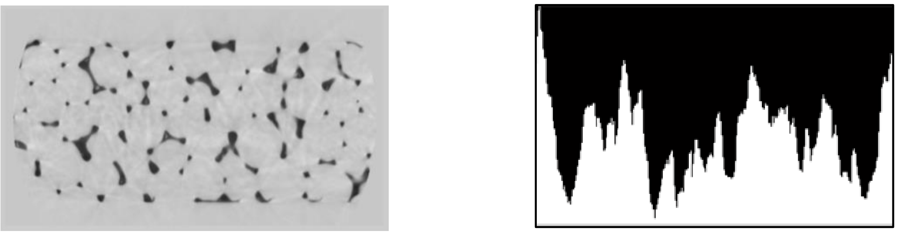

(a) (b)

Figure 2.14 Image processing for cross sectional view of 5 PPI metal foam (a) X-rays image of foam slice (b) intensity distribution of the image.

Table 2.5 Free-flow cross-sectional area of metal foams

Foam designation	Measured A_{min}/A_{fr}	Manufacturer's reported porosity
5 PPI	0.988	0.97
10 PPI	0.977	0.96
20 PPI	0.971	0.95
40 PPI	0.957	0.93

Table 2.6 Geometric parameters of metal foams

Foam designation	Pore diameter, D_p (mm)	Ligament diameter, D_f (mm)	Hydraulic diameter, D_h (mm)
5 PPI	4.02±0.04	0.50±0.05	6.34
10 PPI	3.28±0.04	0.45±0.04	4.61
20 PPI	2.58±0.05	0.35±0.05	2.69
40 PPI	1.80±0.05	0.20±0.04	1.74

For comparison to other heat exchangers, the friction factor is plotted versus *Re* for various foams, with L_c=D_h, in Figure 2.15a. Comparing to the general trends in Kays and London

[2.26], it is clear that the metal foams have a very high *f*-factor. Moreover, because the data do not collapse to a single curve, there is a strong suggestion that another length scale is important (not simply D_h). Through a trial and error process, it was found that the friction factor data would collapse to a single curve, with a goodness of fit suitable for engineering design, if pore diameter was included as a characteristic length. In this process 2 of 64 data were discarded as outliers; the resulting fit had a relative RMS deviation of ±14.86%, and almost all of the data were predicted to within ±20% (Figure 2.16a). The fit uses pore diameter as L_c, with the Reynolds number based on hydraulic diameter:

$$f_{D_p} = \frac{\Delta P}{L} \frac{\bar{\rho}}{G^2} \frac{D_p}{2} = 1.975\,\mathrm{Re}_{D_h}^{-0.1672} \left(D_p / D_h \right)^{-3.708} \tag{2.18}$$

Similarly, in order to facilitate comparison to conventional compact heat exchangers, the Colburn *j* factor, with $L_c = D_h$, is presented in Figure 2.15b. As shown in the figure, foams with higher pore density (PPI) had higher *j* factors. In comparison to most conventional heat exchangers (e.g., louvers), metal foams have a high Colburn *j* factor. Attempting to fit the data in this format, only to Re_{Dh}, results in a fit with a relative RMS deviation of more than ±10%; however, when pore diameter, D_p, is used as an additional characteristic length, the following fit predicts all dry-foam heat transfer data with a relative RMS deviation of 4%:

$$j_{Dp} = \frac{h}{\bar{\rho} \bar{c}_p V} \frac{D_p}{D_h} \mathrm{Pr}^{2/3} = 2\,\mathrm{Re}_{Dh}^{-0.5611} \left(D_p / D_h \right)^{0.3213} \tag{2.19}$$

The predicted and measured Colburn *j* factors are presented in Figure 2.16b. The uncertainty was 8%.

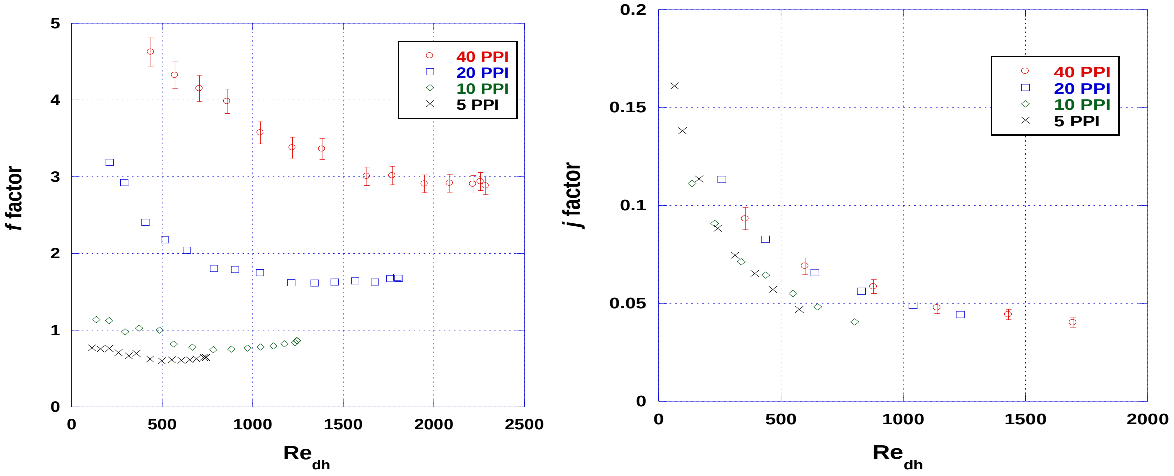

(a) (b)

Figure 2.15 (a) Friction factor (b) Colburn j factor for metal foam with different pore sizes plotted against Reynolds number (based on hydraulic diameter).

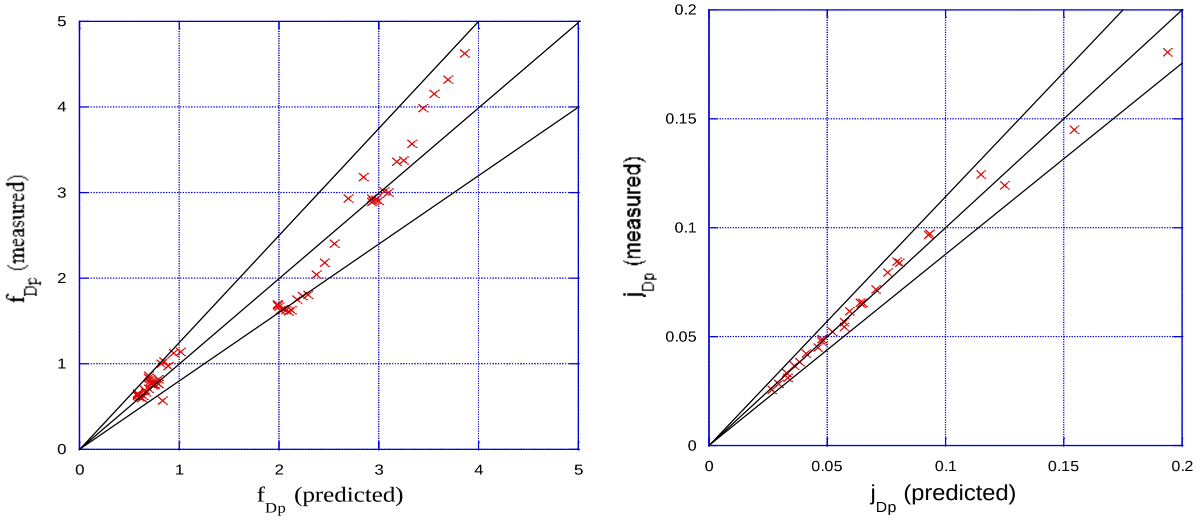

(a) (b)

Figure 2.16 (a) Friction factor with pore diameter as a characteristic length, measured versus predicted (Equation 18). The relative RMS deviation is ±14.86%; limits of ±20% are shown in the plot. (b) Colburn j factor with pore diameter as a characteristic length, measured versus predicted (Equation 19). The relative RMS deviation is ±4%; limits of ±12.5% are shown in the plot.

2.6 Conclusions

The thermal-hydraulic performance of the metal foams has been analyzed using data from wind tunnel experiments. The flow conditions, metal foam characteristics and heat exchanger geometry affect the performance. The pressure drop and heat transfer rate increase as the face velocity increases. Pore size is an important parameter in determining the pressure drop and heat transfer rate. Foams with a smaller pore size have a higher heat transfer coefficient due to better flow mixing, but the resulting pressure gradient is higher as well. The geometry of metal foam heat exchangers can considerably reduce the pressure drop without significantly compromising the heat transfer performance. The base material of metal foam heat exchangers also plays important role by affecting the heat transfer rate. Overall thermal hydraulic performance of metal foam heat exchangers surpasses existing designs such as louver-fins. There are various models available to predict the pressure drop and heat transfer coefficient, but they are based on non-realistic geometries, and they fail to predict the performance accurately. It was found that more than one length scale is important to the pressure gradient and heat transfer rate in metal foams. By using a Reynolds number based on hydraulic diameter, a curve fit for the friction factor f and Colburn j factor based on pore diameter has been developed with reasonable engineering accuracy.

2.7 References

[2.1] X. Han, Q. Wang, Y. Park, C. T' Joen, A. Sommers, A. M. Jacobi, A review of metal foam and metal matrix composites for heat exchangers and heat sinks (Review), Heat Transfer Engineering 33 (2012) 991-1009.

[2.2] M. Kaviany, Principles of Heat Transfer in Porous Media, Springer-Verlag, New York, 1995, Chapter. 2.

[2.3] J. L. Lage, The fundamental theory of flow through permeable media form Darcy to turbulence, Transport Phenomena in Porous Media (1998) D.B. Ingham and I. Pop eds., Pergamon, New York, 1–30.

[2.4] D.A. Nield, Modeling fluid flow and heat transfer in a saturated porous medium, Journal of Applied Mathematics and Decision Sciences 4 (2000) 165-173.

[2.5] H. Darcy, Les Fontaines Publiques de la ville de Dijon., Dalmont, Paris. 1856.

[2.6] D. Seguin, A. Montillet, J. Comiti, Experimental characterization of flow regimes in various porous media-I: Limit of Laminar Flow Regime, Chemical Engineering Science, 53 (1998) 3751–3761.

[2.7] J. L. Lage, B. V. Antohe, D. A. Nield, Two types of nonlinear pressure-drop versus flow-rate relation observed for saturated porous media, ASME Journal of Fluids Engineering 119 (1997) 700-706.

[2.8] S. Ergun, Fluid flow through packed columns, Chemical Engineering Progress 48 (1952) 89–94.

[2.9] S. Crosnier, R. Rivam, B. Bador, V. Blet, Modeling of gas flow through metallic foams, Presented at the 1st European Hydrogen Energy Conference, 2003, Alpexpo-Alpes Congrés, Grenobel, France.

[2.10] L. Tadrist, M. Miscevic, O. Rahli, F. Topin, About the use of fibrous materials in compact heat exchangers, Experimental Thermal and Fluid Science 28 (2004) 193–199.

[2.11] A. Bhattacharya, V.V. Calmidi, R.L. Mahajan, Thermophysical properties of high porosity metal foams, International. Journal of Heat and Mass Transfer 45 (2002) 1017–1031.

[2.12] K. Boomsma, D. Poulikakos, Y. Ventikos, Simulation of flow through open cell metal foams using an idealized periodic cell structure, International Journal of Heat and Fluid Flow 24 (2003) 825–834.

[2.13] C. Naakteboren, P.S. Krueger, J.L. Lage, The effect of inlet and exit pressure-drop on the determination of porous media permeability and form coefficient, ASME Fluids Engineering Division Summer Meeting and Exhibition, 2004, Houston, TX,.

[2.14] M.D.M. Innocentini, L.P. Lefebvre, R.V. Meloni, E. Baril, Influence of sample thickness and measurement set-up on the experimental evaluation of permeability of metallic foams, Journal of Porous Materials 17 (2009) 491-499.

[2.15] C.Y. Zhao, Review on the thermal transport in high porosity cellular metal foams with open cells, International Journal of Heat and Mass Transfer 55 (2012) 3618-3632.

[2.16] G.B. Ribeiro, J.R. Barbosa, A.T. Prata, Performance of microchannel condenser with metal foams on the air-side: Application in small scale refrigeration systems, Applied Thermal Engineering 36 (2012) 152-160.

[2.17] V.V. Calmidi, R.L. Mahajan, Forced convection in high porosity metal foams, ASME Journal of Heat Transfer 122 (2000) 557–565.

[2.18] L.B. Younis, R. Viskanta, Experimental determination of the volumetric heat transfer coefficient between stream of air and ceramic foam, International Journal of Heat and Mass Transfer 36 (1993) 1425–1434.

[2.19] N. Dukhan, K.C. Chen, Heat transfer measurements in metal foam subjected to constant heat flux, Experimental Thermal and Fluid Science 32 (2007) 624–631.

[2.20] Z. Dia, K. Nawaz, J. Bock, A.M. Jacobi, Correcting and extending the Boomsma-Poulikakos effective thermal conductivity model for three-dimensional, fluid-saturated metal foams, International Communications in Heat and Mass Transfer 37(2010) 575-580.

[2.21] K. Boomsma, D. Poulikakos, On the effective thermal conductivity of a three dimensionally structured fluid-saturated metal foam, International Journal of Heat and Mass Transfer 44 (2001) 827–836.

[2.22] Z. Dia, K. Nawaz, Y. Park, C. Qi, A.M. Jacobi, A comparison of metal-foam heat exchangers to compact multi-louver designs for air-side heat transfer applications, Heat Transfer Engineering 33 (2012) 21-30.

[2.23] K. Nawaz, J. Bock, A.M. Jacobi, Experimental studies to evaluate the use of metal foams in highly compact air-cooling heat exchangers, 13th International Refrigeration and Air Conditioning Conference, July 2012, Purdue University Lafayette, IN.

[2.24] R.J. Moffat, J.K. Eaton, A. Onstad, A method for determining the heat transfer properties of foam-fins, ASME Journal of Heat Transfer 131 (2009) 011603-1.

[2.25] F.P Incropera, D.P. DeWitt, Fundamentals of heat and mass transfer, 4th ed. 1996, John Wiley & Sons.

[2.26] Y. Park, A.M. Jacobi, Air-side heat transfer and friction correlations for flat-tube, louver-fin heat exchangers, ASME Journal of Heat Transfer 131(2009) 061801-1.

[2.27] W.M. Kays, A.L. London, Compact Heat Exchangers, 2nd ed, 1964, McGraw-Hill, New York.

[2.28] J. Bock, A. M. Jacobi, Geometric classification of open-cell metal foams using X-ray micro-computed tomography, Materials Characterization 75 (2013) 35-43.

Chapter 3-Adsorption and desorption performance of silica aerogels

3.1 Introduction

A vast majority of recent studies on dehumidification systems have focused on the development and application of solid adsorbent materials that can provide improved adsorption capacity and higher moisture removal rates [3.1–3.3]. Adsorption systems with improved performance result in a considerable decrease in the initial and operating costs and in some cases make such dehumidification systems attractive alternatives to existing vapor compression systems for cooling and dehumidification. Generally, solid salt adsorbents (e.g. calcium chloride and cobalt chloride) have greater hygroscopic capacity than other inorganic adsorbents, such as silica gel; however; calcium chloride granules often deliquesce beyond an adsorptive capacity of 0.33 kg/kg, after the formation of the solid crystalline hydrate, $CaCl_2{\cdot}2H_2O$ [3.3]. To overcome this problem, desiccant materials based on silica gel have become an attractive alternative to the salt-based adsorbents. They have been used as high-performance desiccants to remove water vapor from humid ventilation air for buildings [3.4]. Silica aerogels are highly porous materials with low density, low thermal conductivity, as well as large surface area. They have received significant attention in heat insulation [3.5], waste treatment [3.6], drug delivery and targeting systems [3.7, 3.8], as well as many other applications. Silica aerogel has a relatively high moisture adsorption capacity because of its microporous structure of internal interlocking cavities, which gives a high internal surface area (up to 800 m^2/g, or 10^8 to 10^9 m^2/m^3) [3.9].

When the water vapor pressure at or near any pore region of a silica gel particle is lower than the adjacent air water vapor pressure, water molecules diffuse through the air and are adsorbed onto the internal pore surfaces of the silica gel particles. Another advantage of using silica aerogel is the fact that there is no chemical reaction during adsorption, unlike many salt absorbents which change their chemical composition and physical appearance with addition of moisture. Even when saturated with water vapor, silica gel still has a dry appearance with its geometry unchanged. The adsorption and desorption characteristics of different silica gel samples may vary because of different manufacturing procedures [3.3]. Although silica gel is frequently used as a desiccant, the detailed heat and moisture transport within the pores of silica gel particles is a complicated process and research is ongoing. Comprehensive experimental studies of the physicochemical properties and some research applications of the organic and salt-based adsorbents have been reported by Aristov *et al.* [3.1] and Zhang *et al.* [3.3]. These studies show that silica-aerogel-based adsorbents have a higher adsorption capacity and can be regenerated with a lower temperature than the other commercially available desiccants, such as activated carbon.

Despite such promising properties, ultimate conclusions on the feasibility of these materials for sorption systems can only be drawn after dynamic analysis of the absorbent and desorbing performance under operating conditions typical to sorption/desorption systems. The performance of a porous adsorbent solid in adsorption of an adsorbate gas is determined not only by the adsorption isotherm, but also by the desiccant mass diffusivity, which affects the adsorption rate. However, up to present, the studies on dynamic adsorption properties of composite adsorbents are very rare, and this is especially true for the solid side mass diffusivity of aerogels with different microstructures. In order to help fill this gap, the main aim of the present work is to investigate the dynamic properties and solid side mass diffusivity of different types of silica aerogels.

3.2 Literature review

3.2.1 Preparation of silica aerogels

Generally, the synthesis of silica aerogels using silicon alkoxide takes place in two steps: (1) a sol–gel process to prepare the gel, and (2) supercritical drying of the gel to obtain an aerogel [3.10-3.15]. In a sol–gel process the hydrolysis of silicon alkoxides generates intermediate species and these species then undergo a stepwise poly-condensation reaction to form a three-dimensional gel network. The secondary step is the supercritical drying of the gel, which involves drying at the critical temperature and pressure of the solvent present in the pores of gel to form an aerogel. The supercritical drying for the synthesis of silica aerogels requires a special type of autoclave assembly. Many research groups have synthesized silica aerogels using tetraethoxy silane precursor (TEOS) using ambient pressure drying, wherein the surface chemical modification of silica surface was carried out prior to drying [3.16-3.19]. However, silica aerogels prepared using TEOS precursors have the disadvantages of relatively high density and low porosity, which hinders wider application of these materials. It has been observed that in a system with a highly polar solvent, the solvent is expected to affect the rate determining step and, therefore, the nature and size of the resulting polymeric particles [3.20]. It has been reported that, acetonitrile is a highly polar aprotic solvent, which does not form hydrogen bonds with the silicate nucleophile, but reduces the rate of the condensation reaction. This behavior is due to the high polarity of acetonitrile, which stabilizes the anionic reactants with respect to the activated complex [3.21]. Furthermore, acetonitrile is an easily displaceable ligand and miscible with water and methanol. Therefore, in order to obtain optically transparent and low density silica aerogels acetonitrile has been employed in the sol–gel process [3.22, 3.23]. However, in these reports the methods used for the preparation of aerogels are time consuming and not scalable for commercialization.

Brinker and Scherer [3.24] described the parameters that affect the sol-gel process; including the way hydrolysis and condensation are carried out, the pH of the catalyst used, and the temperature and pressure. Their work also described the effects of ageing and possible applications of different types of aerogels. Prakash *et al.* [3.25] prepared silica films with the range of porosity from 91% to 98.5% at ambient pressure by a process wherein organo-siloxane polymers were deposited on a silicon substrate by conventional dip-coating at 25°C and 0.85 bar and then heated to 450°C. The film thicknesses (from scanning electron microscopy) varied from 0.1 to 3.5 microns, depending upon the dip-coating rate (0.05-1.9cm/s) and concentration of the solvent. The process was optimized by varying the dilution, ageing, organic modification, heat treatment and dip-coating conditions, allowing control of film porosity from 30% to 99%. Scherer *et al.* [3.26] found that when a gel is heated, the thermal expansion of the pore liquid causes stretching of the solid network. If the heating rate is very high, the gel expands at the same rate as the liquid; at slower rates, some of the liquid drains out and the gel expands less. Pel *et al.* [3.27] presented a procedure to determine the moisture diffusivity for drying from measured moisture concentration profiles. They also described a means of determining the relative error of moisture diffusivity, when they used their proposed method for evaluating diffusion performance.

3.2.2 Characterization of silica aerogels

Shen *et al.* [3.28] prepared silica aerogels by a sol-gel technique from industrial silicon derivatives (polyethoxydisiloxanes, E-40), followed by silylation and drying under ambient pressure. The specific surface area, pore size distribution and thermal conductivity of the silica aerogels were investigated and the results showed that the diameter of the silica particles was approximately 6 nm, and the average pore size of the silica aerogels was 14.7 nm. The specific surface area was approximately 1000 m^2/g and the thermal conductivity was approximately 0.014 W/m-K at room temperature and a pressure of 101 k Pa. Si-CH_3 groups were also detected on the surface of the silica aerogels, which explained the hydrophobic behavior of silica aerogels. Lucas *et al.* [3.29] analyzed pore structures and mechanical properties of silica aerogels obtained by traditional base-catalyzed sol–gel synthesis. They concluded that these characteristics can be modified by curing in neat methanol. The curing process produced gels with a larger mean pore-size and more cumulative pore volume than their uncured (standard) counterparts, both before and after heat-treatment steps. Cured silica aerogels that were densified by heat treating in air at 900 °C for 30 min retained a mean pore-size of about 30 nm, comparable to a standard or dry silica aerogel. Heating the standard silica aerogel to 900 °C for 30 min markedly decreased the mean pore-size to 16 nm. Magaliga *et al.* [3.30] experimentally determined the effective diffusion coefficients of water vapor in pure and calcium chloride and lithium bromide impregnated silica gels. The experiments were performed at a temperature of 323 K using spherical particles of silica aerogels with a diameter of 3.57 mm. Diffusion coefficients were determined from moisture adsorption rate. They concluded that effective diffusivity of water was about three times lower in impregnated silica gel than pure silica gel. The difference occurred due to the equal contribution of different diffusion mechanisms (Knudsen and bulk diffusion). It is important to note that salts, which are often mixed with pure silica aerogels to enhance the adsorption capacity of the desiccant or for durability during a cyclic process, often decrease the adsorption rate.

Yadav and Bajpai [3.31] analyzed the regeneration and adsorption performance of different desiccants, such as silica gel, activated alumina, and activated charcoal, for producing dry air. The air needed for regeneration was heated in an evacuated-tube solar collector. The desiccants were regenerated at temperatures in the range of 54.3 to 68.3 ^{0}C. The regeneration performance was greatly affected by the regeneration temperature, but also depended on the initial moisture content, temperature of the desiccants, and flow rate of regeneration air. Comparison of the performances showed that at high hot air flow rates the regeneration times and adsorption times were shorter for these desiccants than at low flow rates. Silica gel was observed to perform better than activated alumina and activated charcoal for regeneration and adsorption at high and low flow rates.

3.2.3 Determination of mass diffusivity

In order to undertake a quantitative analysis of the moisture transport in silica aerogels, the mass diffusion coefficient must be known. It is well known that water vapor can diffuse through a porous medium by ordinary (Fickian) diffusion or Knudsen diffusion. Surface diffusion often classified to distinguish the surface (adsorption) *vs.* volumetric (absorption) phenomena. The diffusion coefficients can be calculated based on kinetic theory and are often used in performance simulation of adsorption systems [3.8, 3.32]. Both ordinary and Knudsen diffusion coefficients can be expressed in a Fickian form, but surface diffusion is expressed in a theoretical Arrhenius form as a function of surface concentration (through the heat of adsorption).

The transport processes that prevail at isothermal conditions are shown in the Figure 3.1. Knudsen diffusion becomes important when the diameter of the pores is of the same order of magnitude as the mean free path of the molecules, the different sorts of molecules move independently of each other and diffusion is governed by the collisions of the molecules with the walls. However for characteristic length scale (average pore diameter-Figure 3.3) for most of the silica aerogels is much larger compared to mean free path of water molecule. Hence, the Knudsen diffusion can be neglected for diffusion process through irregular porous media with large pore size (>30 nm) at room temperature and pressure.

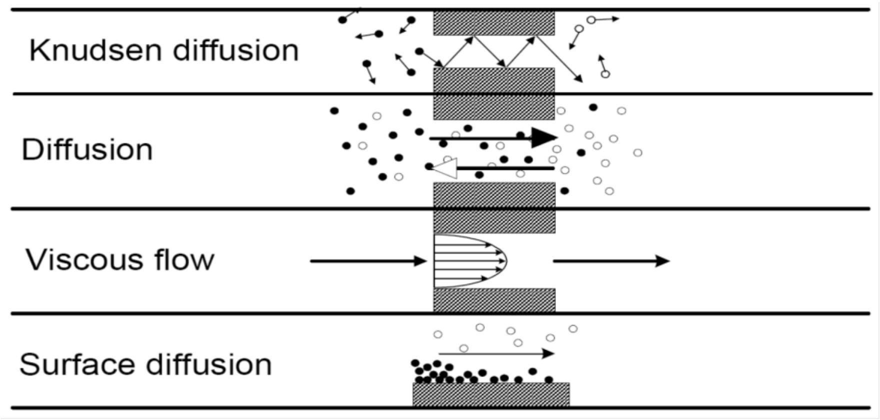

Figure 3.1 Different transport processes [3.33]

The mass diffusivity of an adsorption system can be determined by using several different approaches, the two most common methods are traditional uptake rate measurements and nuclear magnetic resonance (NMR) measurements.

Three experimental methods have been developed for the measurement of bulk diffusion coefficient in desiccant materials: analysis of drying data, sorption kinetics, and permeability measurements. The first two methods can be applied to various shapes of desiccants, while the permeability method is limited to desiccant films as demonstrated by Karathanos and Saracacos

[3.36]. Obtaining moisture diffusion coefficients from drying data is the most commonly used method [3.36]. In general, the moisture diffusion coefficient is calculated from the slope of the drying curve or from the comparison of the experimental drying curve to those predicted by Fick's second law [3.35].

For the sorption kinetics approach, only a limited amount of research has been conducted. Lamauro *et al.* [3.38] used petri dishes containing saturated salt solutions to control relative humidity values to measure the bulk diffusion coefficient of dry and semi-moist materials. The sorption kinetics data were obtained by weighing these samples with initial weight of 1.0 and 1.3 grams at 1-week intervals until equilibrium was reached. Spieles *et al.* [3.37] evaluated the effect of temperature and pressure on water mass transport during the secondary drying stage for concentrated, aqueous solutions of hydroxyethyl starch, a stabilizing agent common in the freeze-drying of biological materials. Similarly Steckel *et al.* [3.39] used relative humidity rooms to study moisture diffusion properties of various materials. Such methods require cumbersome weight measurements and long data collection times. Valkovska and Danov [3.40] presented a method for the determination of the surface diffusion coefficient and surface diffusion flux. The theoretical considerations are based on the Onsager linear theory for the definition of the surface diffusion flux and on the Einstein theorem for the definition of the surface diffusion parameter. In this interpretation, the surface diffusion coefficient differs from the one commonly defined in the literature. It does not depend on the surfactant concentration and it is a function only of the type of surfactant and the liquid/liquid interface. They found that the theoretical calculations indicate that the effect of the surface diffusion on the film drainage was stronger than that predicted by previous theoretical studies [3.40].

New automated water sorption instruments, which can be used to conveniently and precisely control both relative humidity and temperature, provide a faster, more robust method for determining the bulk diffusion coefficient, compared to traditional sorption techniques. However, only a few researchers have utilized these instruments for obtaining diffusion coefficients. Roman-Gutierrez *et al.* [3.41] and Burnett *et al.* [3.42] used a Dynamic Vapor Sorption (DVS) instrument (Surface Measurement System Ltd, London, UK) to collect the data to be used for determining the moisture diffusion coefficients for different proton exchange membranes. Different mathematical models were used in these studies to calculate the apparent bulk diffusion coefficients. Roca *et al.* [3.43] investigated the impact of formulation and initial porosity of sponge cakes on the water vapor diffusion using a DVS. Roman-Gutierrez and colleagues [3.42] used the diffusion model for polydispersed spheres derived from Fick's second law for wheat flour samples contained in a DVS flat video pan, while Burnett and others [3.42] used the thin-slab model derived from Fick's second law for proton exchange membranes contained in a DVS mesh pan. Roca and others [3.43] used a solution to the Fick's second law for sponge cake. Yu *et al.* [3.44] used the DVS as a faster, more robust method for collecting the data needed for determining the bulk diffusion coefficient (D_b). The objectives of that study were to investigate the use of the DVS instrument for collecting the data needed for determining the adsorption (D_{ba}) and desorption (D_{bd}) bulk moisture diffusion coefficients for dent corn starch as a function of relative humidity and to determine the effect of temperature on D_{ba} for dent corn starch at a constant relative humidity. Kinetic water adsorption profiles of dent corn starch were obtained at eight relative humidity values ranging from 10 to 80% at 10% intervals at 25 °C and at five temperatures, 15, 20, 25, 30, and 35 °C, at 50% relative humidity using a DVS instrument. D_b was calculated from the kinetic water adsorption profiles using the full solution of Fick's second law for the thin slab model proposed by Peppas and Peppas [3.45].

3.2.4 Sorption and desorption isotherms

The retention (or release) of a liquid compound on a solid controls the mobility of many substances in the environment and has been quantified in terms of the ‘‘sorption isotherm’’. The sorption isotherm is a common approach to describe a great diversity of retention/release phenomena. This is very useful and often unavoidable to understand and predict the mobility of sorbing substances in the environment. However, a sorption isotherm is empirical in nature, thus not saying, by itself, anything on the complicated mechanisms involved. In particular, it is important to verify if thermodynamic equilibrium is reached within the reaction- (or residence-) time, both for the retention and for the release stage of the compound. Otherwise, kinetic experiments must be considered. Since the isotherm is not an intrinsic property of the substance/solid couple, the measurement method has a great influence on the results. Thus, it must be chosen carefully and always described with the results in detail. Other methods allow the investigation of the retention microscopically, particularly with spectroscopic and microscopic tools. They have provided a new efficient way to verify several assumptions used in isotherm interpretations on the solid structure and retention/release mechanisms, thus leading to more confidence in structure-based and mechanism-based complicated models. On the other hand, the increasing power of computers makes possible not only improving mechanistic models of speciation, but also running ‘‘Molecular Dynamic Experiments’’. However, natural media are such complicated mixtures of numerous mineral and organic compounds that empirical approaches such as the ‘‘sorption isotherm’’ will still be used for a long time to come [3.46-3.48].

Limousin *et al.* [3.49], reviewed different empirical and mechanistic models, and details several experimental methods to acquire the sorption isotherm. They concluded that the adsorption (or desorption) isotherm does not provide automatically any information about the reactions involved in the sorption phenomenon. So, mechanistic interpretations must be carefully verified. The range of reaction times to reach equilibrium was found to be extremely wide depending on the type of material and process. They also found that a pseudo-hysteresis of the release compared with the retention was often observed. The comparison between the mean characteristic time of the reaction and the mean residence time of the mobile phase in the natural system allowed knowing if the studied retention/release phenomenon should be considered as an instantaneous reversible, almost irreversible phenomenon, or if reaction kinetics must be taken into account. Ng *et al.*, [3.50] reviewed the development of nanoporous sorbents for water. They studied the mechanism of water sorption of commonly used sorbents with emphasis on the modification methods for enhancement of their water sorption capacity. The mostly widespread adsorbents for water are molecular sieves (zeolites and mesoporous materials), activated carbon, silica gel/aerogel, clays, and aluminophosphates were described to have regular or irregular pore systems ranging from micro- to meso- to macro-dimensions, which was found to be the base for their high water sorption capacity.

Knez and Novak [3.51] established water vapor adsorption isotherms in aerogels gravimetrically at 293 K. They also measured the adsorption/desorption isotherms of nitrogen at 77 K and used the adsorption/desorption data for investigation of specific surface areas of silica aerogel samples. Prior to the measurements, each sample was dried in a vacuum. Aerogel adsorbents were also viewed with transmission electron microscopy (TEM) to define both the morphology and porous texture. The investigation of adsorption of water vapor on silica, alumina, and mixed silica-alumina aerogels, prepared by supercritical CO_2 drying showed that all three aerogels exhibited adsorption capacities in the range between 1.0 and 1.2 kg of water/kg of aerogel, which was markedly higher than other well-known adsorbents. The adsorptivity of a mixed silica-alumina aerogel was found to be higher than the adsorptivities of both single aerogels in repeated adsorption and desorption cycles and remained unchanged after 25 cycles. Novak *et al.* [3.52] conducted a study focused on the adsorption capacity of different adsorbents for benzene, toluene, ethylbenzene and xylene (BTEX) vapors using the mini-column method. Continuous adsorption measurements show that silica aerogels were excellent adsorbents of (BTEX) vapors from waste gas stream.

International Union of Pure and Applied Chemistry (IUPAC) has identified following six types of equilibrium isotherms (Figure 3.2)

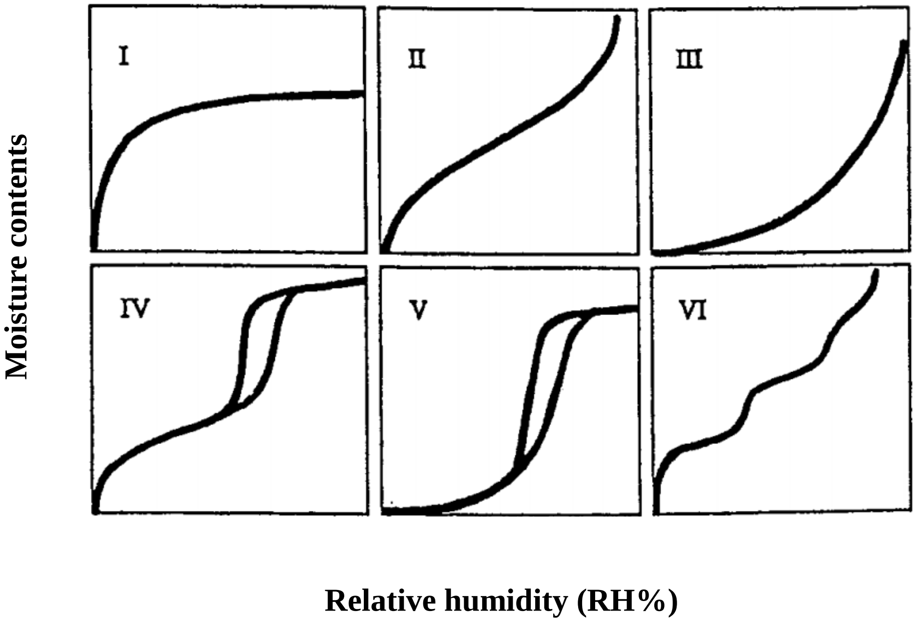

Figure 3.2 IUPAC classifications of equilibrium isotherms [3.53]

It is interesting to note that for type IV and V isotherms, commonly observed for the desiccant materials, the adsorption and desorption isotherms do not follow the same behavior. Many studies have been conducted to explain the presence of hysteresis in some isotherms. Naumov [3.54] investigated the origin of the adsorption hysteresis phenomenon typical for mesoporous materials. He studied the adsorption dynamics and the equilibrium properties of guest molecules in mesopores using nuclear magnetic resonance, the macroscopic information, accessible by transient sorption experiments, and the microscopic information, provided by the effective self-diffusivities and concluded that slowing down of the transient uptake happens due to the onset of capillary.

3.2.5 Modeling of sorption/desorption isotherms

Over the years, a wide variety of equilibrium isotherm models (Langmuir, Freundlich, Brunauer Emmett–Teller, Redlich-Peterson, Dubinin–Radushkevich, Temkin, Toth, Koble–Corrigan, Sips, Khan, Hill, Flory–Huggins and Radke–Prausnitz isotherm), have been formulated based on three different fundamental approaches. The first approach is based on kinetic consideration. In such an approach adsorption equilibrium is defined being a state of dynamic equilibrium, with both adsorption and desorption rates are equal [3.55]. A second approach is based on thermodynamics. Such an approach provides a framework of deriving numerous forms of adsorption isotherm models [3.56, 3.57] and potential theory is the third approach which provides the attributes of characteristic curves for equilibrium isotherms [3.58].

Foo and Hameed [3.59] provided a comprehensive literature review sorption isotherm modeling. They concluded that linear regression has been developed as a major option in designing the adsorption systems. Though the approach was simple to use many investigations had indicated the growing discrepancy (between the predictions and experimental data) and disability of the model, propagating towards a different out come.

Malek and Farooq [3.60] studied seven different isotherm models using equilibrium data of methane, ethane and propane in activated carbon. Besides comparing the goodness of data fit, the limiting behaviors as well as the pressure and temperature derivatives of the equilibrium isotherm models were also investigated. This systematic evaluation of the more important equilibrium isotherm models provided the general basis for making a preliminary selection of an effective model for a given application.

Ho et al. [3.61] investigated the sorption of divalent metal ions (copper, nickel and lead) from aqueous solution onto peat in single component systems and the equilibrium were isotherms determined. The experimental data was analyzed using the Langmuir, Freundlich, Redlich-Peterson, Toth, Temkin, Dubinin-Radushkevich and Sips isotherm models. In order to determine the best fit isotherm for each system, six error analysis methods were used to evaluate the data: the coefficient of determination, the sum of the errors squared, a hybrid error function, determination, the sum of the errors squared, a hybrid error function, Marquardt’s percent standard deviation, the average relative error and the sum of absolute errors. The error values demonstrated that the Sips equation provided the best model for the three sets of experimental data overall.

Four different isotherms for conventional desiccants are presented in Figure 3.3.

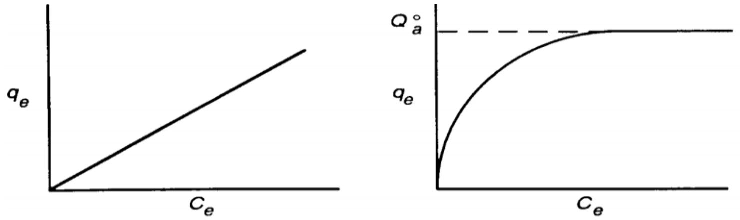

(a) Linear (b) Langmuir

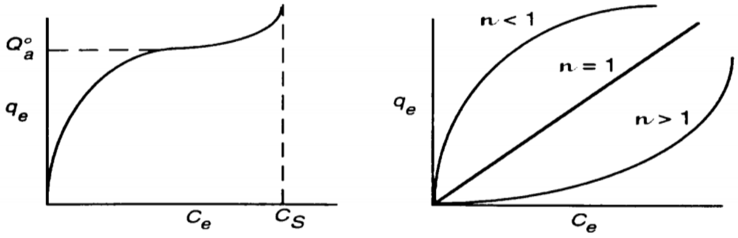

(c) BET (d) Freundlich

Figure 3.3 Isotherm models [3.53]

Linear: $$q_e = k_{lin} c_e \tag{3.1}$$

q_e is amount of solute adsorbed per unit weight of solid at equilibrium. (mg/mg) and c_e is equilibrium concentration of solute remaining in solution when the amount adsorbed equals q_e.

Langmuir: $$q_e = Q_a^o \frac{K_L c_e}{1+K_L c_e} \tag{3.2}$$

q_{max} is maximum adsorption capacity for forming for single layer. K_L is the constant (L/mg).

Freundlich: $$q_e = K_F c_e^{1/n} \tag{3.3}$$

K_F is the constant which indicates the adsorption capacity, while n is the measure of intensity of adsorption.

BET: $$q_e = \frac{K_B c_e Q_a^o}{(c_s - c_e)\{1+(K_B-1)(c_e/c_s)\}} \tag{3.4}$$

c_s is the saturation (solubility limit) concentration of solute (mg/L), K_B and Q are the constants.

3.3 Preparation of silica aerogel samples

3.3.1 Sol-gel chemistry

There are many different preparation methods available to manufacture silica aerogels with hydrolysis and condensation processes occurring in one or two steps. However, most of the silica aerogels are prepared using silicon alkoxide precursors. Generally, tetramethyl orthosilicate (TMOS, Si $(OCH_3)_4$) and tetraethyl orthosilicate (TEOS, Si $(OCH_2CH_3)_4$) are used for this purpose. However, many other alkoxides, containing one or more organic functional groups (alcohols, ethers, aldehydes), can be used to impart different physical properties to the gel. Alkoxide-based sol-gel chemistry avoids the formation of undesirable salt by-products, and allows a much greater degree of control over the physical properties of the product. Formation of a wet gel by TMOS is presented in equation (3.5)

$$\mathrm{Si(OCH_3)}_{4\,(Liq.)} + 2\mathrm{H_2O}_{(Liq.)} \rightarrow \mathrm{SiO}_{2\,(Solid)} + 4\mathrm{HOCH}_{3\,(Liq.)} \tag{3.5}$$

The above reaction is typically conducted in methanol, where the final density of the aerogel is dependent on the concentration of silicon alkoxide monomers in the solution. Note that the stoichiometry of the reaction requires two moles of water per mole of TMOS. In practice, this amount of water leads to incomplete reaction and weak, cloudy aerogels, that is why a higher water ratio than is required by the balanced equation is used (anywhere from 4-30 equivalents).

3.3.2 Catalysts

The kinetics of the above reaction renders it impracticably slow at room temperature, often requiring several days to complete. For this reason, acid or base catalysts are added to the formulation. The amount and type of catalyst used play key roles in the microstructural, physical, and optical properties of the final aerogel product. Acid catalysts can be any protic acid, such as HCl or HF. Basic catalysis usually uses ammonia, ammonium hydroxide or ammonium fluoride). Aerogels prepared with acid catalysts often show more shrinkage during supercritical drying and may be less transparent than base-catalyzed aerogels. The microstructural effects of various catalysts are difficult to describe accurately, as the substructure of the primary aerogel particles can be difficult to image with conventional optical microscopy. Images show small particles that are generally spherical or egg-shaped when observed under optical microscopes. With acid catalysis, however, these particles may appear "less solid" (looking something like a ball of string) than those in base-catalyzed gels as shown in Figure 3.4. As the condensation reaction progresses, the sol will set into a rigid gel. At this point, the gel is usually removed from its mold. However, the gel must be kept covered by alcohol to prevent evaporation of the liquid contained in the pores of the gel. Evaporation causes severe damage to the gel and will lead to poor-quality aerogels.

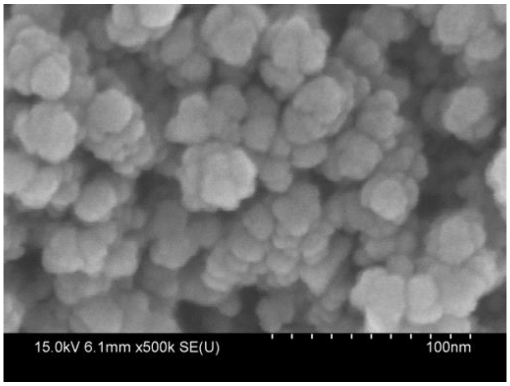

Figure 3.4 Microstructure of silica aerogel prepared by sol-gel process using hydrofluoric acid as catalyst

3.3.3 Aging and soaking

When a sol reaches the gel point, the hydrolysis and condensation reactions of the silicon alkoxide reactant are not necessarily complete. The gel point simply represents the time required at which the polymerizing silica species span the container containing the sol. At this point, the silica backbone of the gel contains a large number of unreacted alkoxide groups. In fact, hydrolysis and condensation can continue for much longer times compared to the time required for gelation. Hence, it is important that sufficient time is given for the strengthening of the silica network. This process can be enhanced by controlling the pH and water content of the covering solution. Common ageing procedures for base-catalyzed gels typically involve soaking the gel in an alcohol/water mixture of equal proportions to the original sol at a pH of 8 to 9 (ammonia). The gels are kept in this solution for up to 48 hours. This step and all subsequent processing steps are diffusion controlled. That is, transport of material into and out of the gel is unaffected by convection or mixing (due to the solid silica network). The diffusion rate is affected by the thickness of the gel. Thus, the time required for each processing step increases dramatically as the thickness of the gel increases. For this reason, in the current study the aerogel samples were prepared in the form of small cylinders with a diameter of 6mm. After ageing the gel, all the water still contained within its pores must be removed prior to drying. Water removal is simply accomplished by soaking the gel in pure alcohol several times until all the water is removed. Again, the length of time required for this process is dependent on the thickness of the gel. Any water left in the gel cannot be removed by supercritical drying, and hence results in an opaque, white, and very dense aerogel.

3.3.4 Drying process

The final, and most important, step in making silica aerogels is drying, where the liquid within the gel is removed, leaving only the linked silica network. The wet gel can be dried either by evaporation or by supercritical drying with CO_2 or alcohols. It was observed in the current study that when the gels are dried by evaporation, the resulting glass-like material (xerogel) cracks and the coating is not durable (Figure 3.5a). Instead of evaporation, if a sample is dried under supercritical conditions, the effects of surface tension, resulting in the cracking of the coating, can be eliminated (Figure 3.5b). In the figure, both specimens were prepared with the same type of gel.

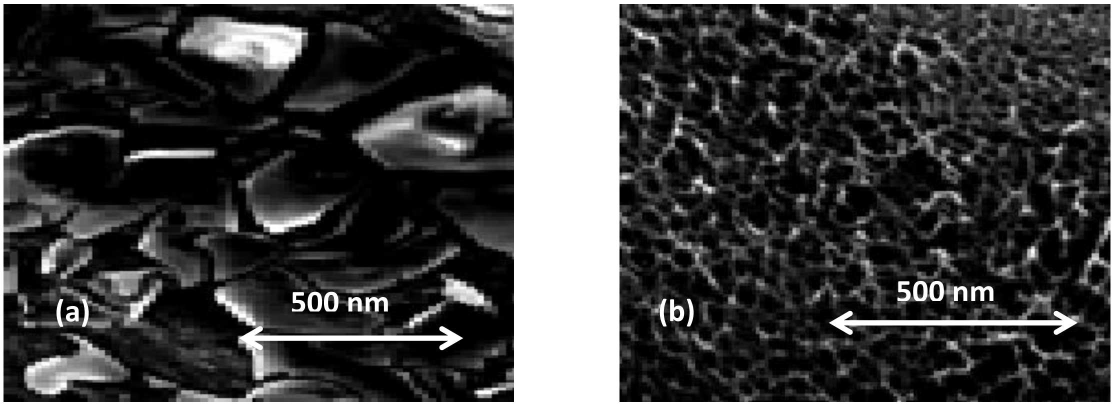

Figure 3.5 SEM images of silica aerogel coated metal foam ligaments dried by (a) evaporation (b) supercritically (CO_2)

The supercritical drying process is performed by venting the ethanol above its critical point or by prior solvent exchange with CO_2 followed by supercritical venting so that the process takes less time to complete. This drying process can only be performed in an autoclave specially designed for this purpose. The alcogels (wet gels) are placed in the autoclave (which has been filled with ethanol/methanol). The system is pressurized to at least 5200-5900kPa with CO_2 and cooled to 5-10^{o}C. Liquid CO_2 is then flushed through the vessel until all the ethanol has been removed from the vessel and from within the gels. When the gels are ethanol free, the vessel is heated to a temperature above the critical temperature of CO_2 ($31^{o}C$). As the vessel is heated, the pressure of the system rises. CO_2 is carefully released to maintain a pressure slightly above the critical pressure of CO_2 (7240kPa). The system is held under these conditions for a short time, followed by the slow, controlled release of CO_2 to ambient pressure. As with previous steps, the length of time required for this process is dependent on the thickness of the gel sample. The process may last anywhere from 12 hours to 6 days. The flow chart (Figure 3.6) summarizes the process for the preparation of silica aerogel.

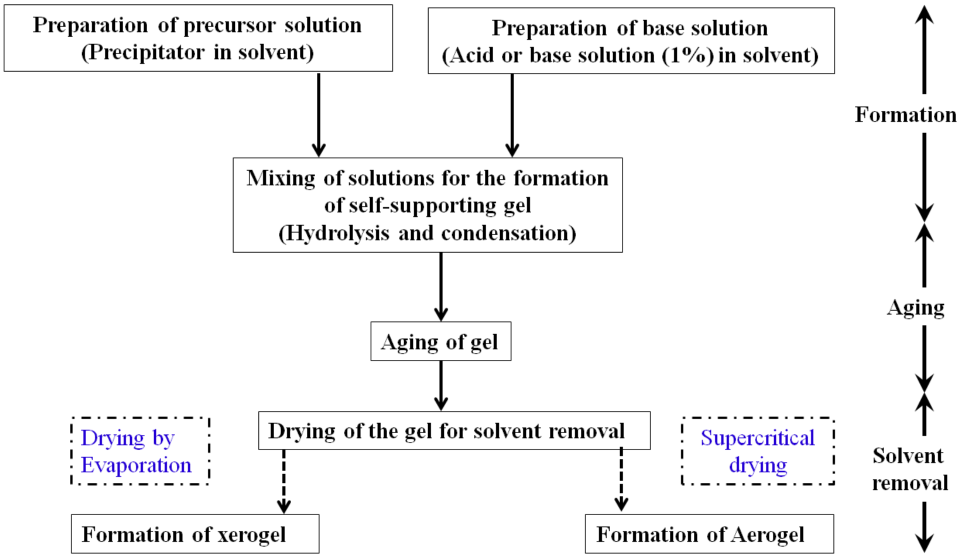

Figure 3.6 Manufacturing of silica aerogels (Adopted from Brinker and Scherer [3.24] and modified)

3.4 Microstructure analysis

The catalyst used in the chemical reaction affects the microstructure of the resulting silica aerogel. In order to evaluate the effect of the catalyst used in the sol-gel process on microstructure, samples were prepared using different catalysts. The specimens were prepared for scanning electron microscopy. The micrographs were recorded with the same magnification (40000x) for all specimens using a *Hitachi 4800* (Hitachi High-Technologies Corporation, Japan) environmental scanning electron microscope at the Materials Research Laboratory (MRL) at the University of Illinois at Urbana-Champaign. The microstructures of six different silica aerogels samples (supercritically dried) are presented in Figure 3.7.

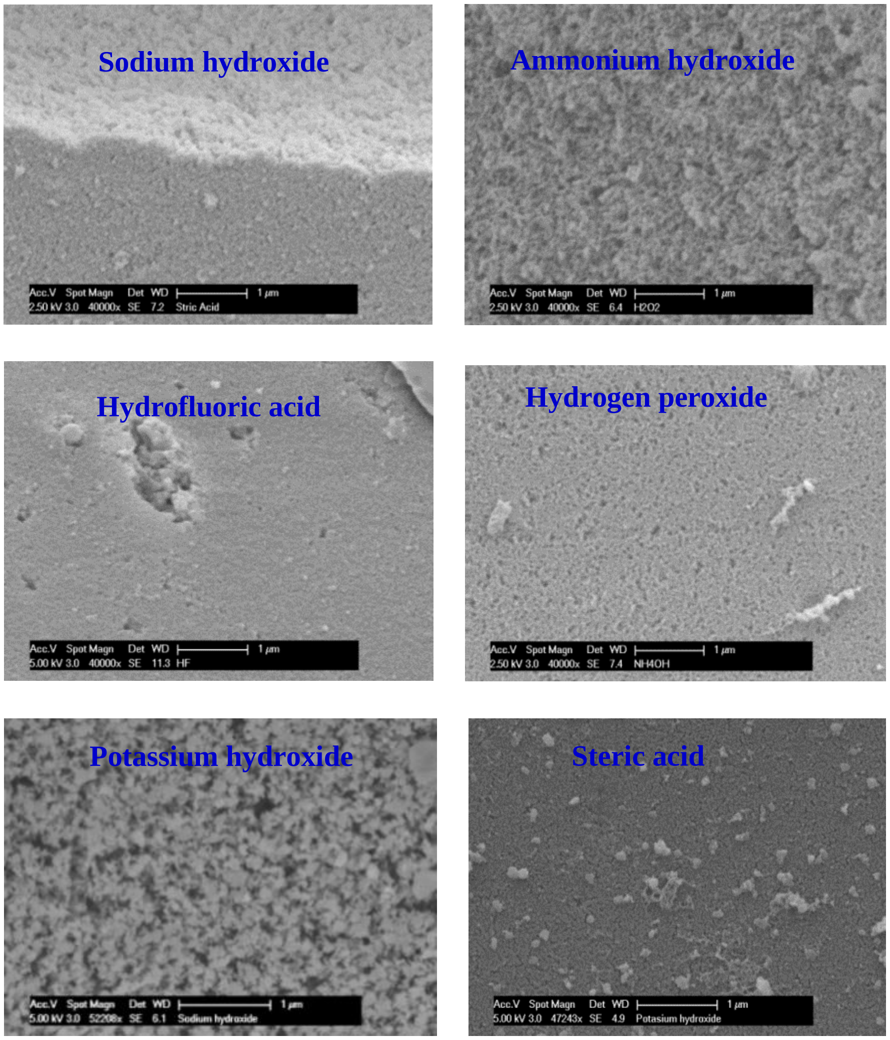

Figure 3.7 Microstructures of six different aerogels prepared by different catalysts

It can be observed from the micrographs of supercritically dried silica aerogel samples that the microstructure (pore size) depends upon the catalyst used in preparation (sol-gel process). Samples prepared using hydrofluoric acid as the catalyst resulted in a more dense structure with small pores, while with potassium hydroxide as the catalyst the structure was highly porous and relatively less dense. It is important to note that the titanium gold sputtering process was avoided to preserve the original microstructure. The sputtering process is often employed in SEM to increase the conductivity of electrically non-conducting material (ceramics and powers) for better magnification.

3.5 Mass diffusivity of silica aerogels

As both equilibrium and transient adsorption/desorption behavior of the desiccant are affected by the microstructure (pore size), it is important to know which catalyst will result in the appropriate pore size range and hence will absorb/desorb more moisture at relatively faster rates compared to the others. In order to evaluate the moisture diffusivity of silica aerogels used as desiccants, transient tests were conducted.

3.5.1 Experimental apparatus and methods

For the transient response of silica aerogels as desiccants, and to determine the diffusion coefficients, a Dynamic Vapor Sorption (DVS Advantage, *Surface Measurement System, UK*) apparatus was used (Figure 3.8). Experiments were performed in which samples were suddenly exposed to a humid or dry environment (compared to the sample water activity) and the weight change was measured (which was converted to moisture content) as a function of time and ultimately used to calculate the diffusion coefficients.

The DVS apparatus is equipped with mass flow controllers for mixing wet and dry nitrogen gas and controlling the relative humidity, and a vapor measurement sensor to monitor the resultant relative humidity and a microbalance to determine the response of the samples. The apparatus has a dry carrier gas (nitrogen), and precise control of the ratio of saturated and dry carrier gas flows was enabled with mass flow control combined with the use of real-time vapor concentration monitoring for water. A known concentration of water vapor then flowed over a sample suspended from a recording ultra-microbalance, which was used to measure the weight change of the sample caused by adsorption or desorption of the vapor molecules.

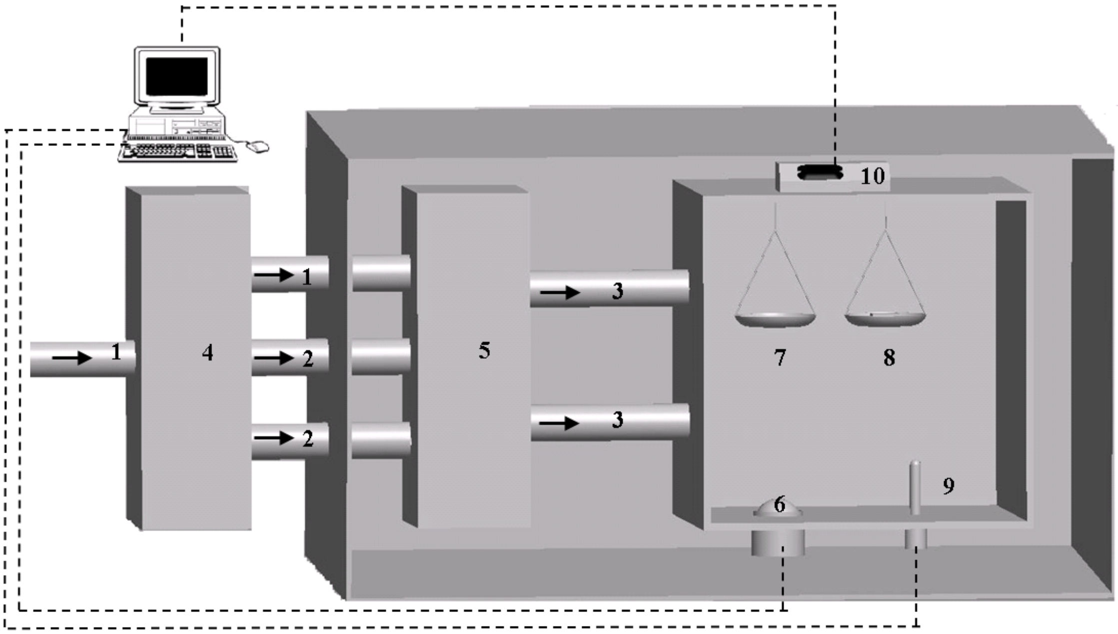

Figure 3.8 Apparatus for dynamic vapor sorption experiments (*Surface Measurement System, UK*) 1-Dry gas, 2-gas for mixture, 3-vapor mixture, 4-mass flow controllers, 5-vapor generator module, 6-camera, 7-sample, 8-reference, 9-humidity sensor, 10-microbalance

The temperature of the entire system was selected and precisely controlled under closed loop conditions to ensure that the solute vapor pressure at the sample is constant. The good sensitivity and precision of the DVS enables the use of very small sample sizes (typically 1 to 30mg), thus allowing equilibrium to be reached quickly, and sample sizes smaller than 2g were used to ensure accuracy. The instrument was fully programmable and controlled by software through a smart operator interface. All experiments were conducted at a temperature equal to 25°C.

3.5.2 Determination of the bulk diffusion coefficient

The DVS sorption automatic operation (SAO) method was used to set both the desired percent relative humidity steps and the equilibrium criterion. First, each sample was equilibrated to 0% RH using an equilibrium criterion of a change in mass over time (dm/dt) of no greater than 0.0005% for 5 consecutive minutes. After this equilibrium criterion was met at 0% RH, the relative humidity was increased automatically to the target value and equilibrated using the same dm/dt criterion (0.0005% for 5 consecutive minutes). The relative humidity was also decreased to 0% RH using a dm/dt criterion (0.0005% for 5 consecutive minutes). Sample mass data and sample and reference chamber relative humidity and temperature data were automatically collected every 60s. A new sample was used for each relative humidity and temperature experimental run. A silica aerogel sample in the shape of small cylinder (Figure 6) was placed on a DVS quartz round bottom sample pan (13 mm in diameter). Total gas flow was parallel to the sample surface and was set at 500 cm^3/min for all experiments. Duplicate runs were conducted for each sample. The uncertainty in the mass measurement using the microbalance is 10micrograms.

The bulk moisture diffusion coefficient can be defined using Fick's first law for a dilute solution (equation 3.6).

$$F = -D\frac{\partial \rho}{\partial r} \tag{3.6}$$

where F is the mass flux of water (kg/s-m^2), D is the diffusion coefficient (m^2/s), ρ is the water partial density (kg/m^3), and r is the radius (m) of the cylinder. The moisture diffusion coefficient can be obtained by solving Fick's second law for the applicable experimental conditions. For the experimental conditions studied here, the moisture diffusion coefficient was obtained by numerically solving Fick's second law for one-dimensional, isothermal penetrate (water) diffusion into (adsorption) or out of (desorption) a cylinder. The assumptions include: (1) D is constant for a given sorption/desorption experiment, (2) swelling (or shrinkage) during adsorption (or desorption) is negligible, (3) the aerogel sample is isotropic and homogeneous, and (4) there is no axial or circumferential diffusion. The one-dimensional transient diffusion equation for a thin cylinder can be written as equation (3.7)

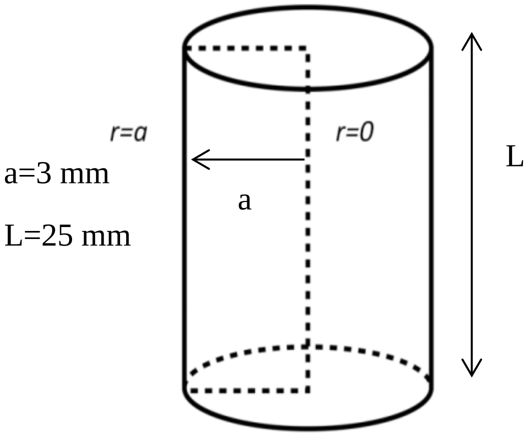

Figure 3.9 Sample geometry

$$\frac{\partial \rho}{\partial t} = D\left(\frac{\partial^2 \rho}{\partial r^2} + \frac{1}{r}\frac{\partial \rho}{\partial r}\right) \tag{3.7}$$

The appropriate initial and boundary conditions for the thin cylinder model used in this study are given by equation (3.8a) and (3.8b), (3.8c) respectively. Infinitely fast diffusion in the gaseous phase is presented by equation (3.8b), while the concentration symmetry at the center of the cylinder is shown by equation (3.8c).

$$\rho(r, t = 0) = 0 \qquad (3.8a)$$

$$\rho(r = a, t) = \rho_\infty \qquad (3.8b)$$

$$\frac{\partial \rho}{\partial r}(r = 0, t) = 0 \qquad (3.8c)$$

Initial water concentration (density) of water vapors in the sample was zero as the sample was dried to remove any vapor concentration. The *r*=*a* boundary is assumed to be at the steady-state concentration for all *t*>0. The initial and boundary conditions specified above correspond to typical conditions found in gravimetric adsorption experiments, where the sample is contained in a sample holder and water adsorption occurs via the outer surface of the sample. The solution to Fick's second law can be represented by equation (3.9)

$$\frac{\rho}{\rho_\infty} = 1 - \sum_{n=0}^{\infty} \frac{4}{a^2 \alpha_n^2} e^{-D\alpha_n^2 t} \qquad (3.9)$$

where α_n are the eigenvalues which are solutions of equation (3.10),

$$J_0(a\alpha_n) = 0 \qquad (3.10)$$

J_0 is the Bessel function of first kind of order zero.

Representative experimental data and the resulting curve fit for determining the diffusion coefficient are shown in Figures 3.10 and 3.11, respectively. The sample was prepared with ammonium hydroxide (catalyst) with methanol and tetra-methyl orthosilicate, used as the solvent and precipitator, respectively. The resulting diffusion coefficient is D=4.70(10^{-10}) m^2/s. By the same procedure, the diffusion coefficients for a sample prepared by hydrofluoric acid as catalyst was determined to be 8.73(10^{-10}) m^2/s and 1.43(10^{-9}) m^2/s for adsorption and desorption, respectively. The uncertainty in calculating the diffusion coefficient was 1.5% based on the uncertainty of the mass balance (10 micrograms).

It is important to note that the diffusion coefficient which is a property of the mixture that is considered not to be affected by the direction of the process. However in the current study it was found that it depends on whether the moisture is adsorbed or desorbed (table 3.1). This phenomenon occurs due to the change in microstructure of desiccant as the moisture contents of in the silica aerogel are changed.

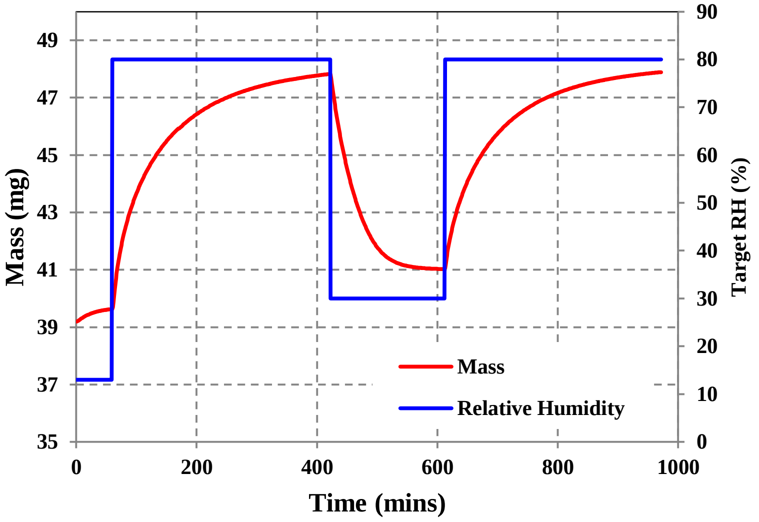

Figure 3.10 Mass variation of the sample due to step change in humidity

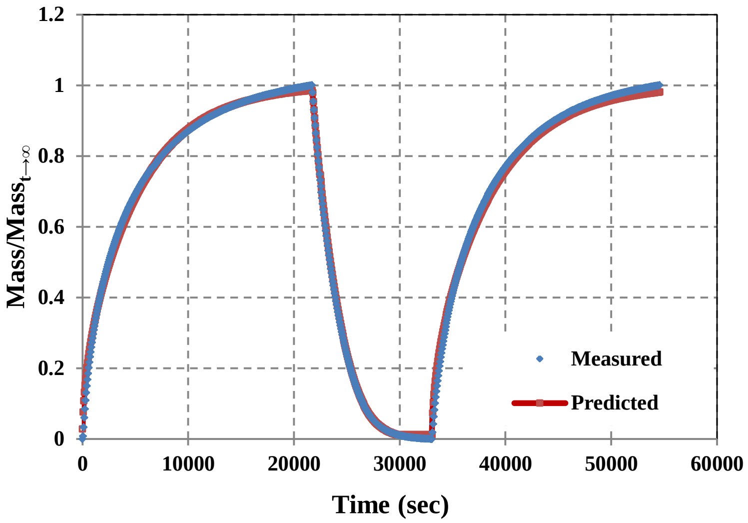

Figure 3.11 Measured and predicted mass change from equation (5) with $D=4.70(10^{-10})\ m^2/s$ for the ammonium hydroxide (catalyst) sample

3.5.3 Parametric study of the bulk diffusion coefficients

The diffusion coefficient is an important transport parameter, which is generally assumed to be constant at a given temperature. In order to determine the dependence of the diffusion coefficient on the environmental humidity increase or decrease and to analyze the variation in an adsorption/desorption cycle, the experiment protocol represented in Figure 3.12 was used. A dry sample was suddenly exposed to 85% relative humidity. After reaching equilibrium, the sample was dried back to 30% RH for desorption. Then RH was increased to 75% and after equilibrium was decreased back to 30%. The next cycle increased the humidity to 65% and decreased back to 30%. The resulting diffusion coefficients for the samples prepared by different catalysts in the sol-gel process are presented in Table 3.1.

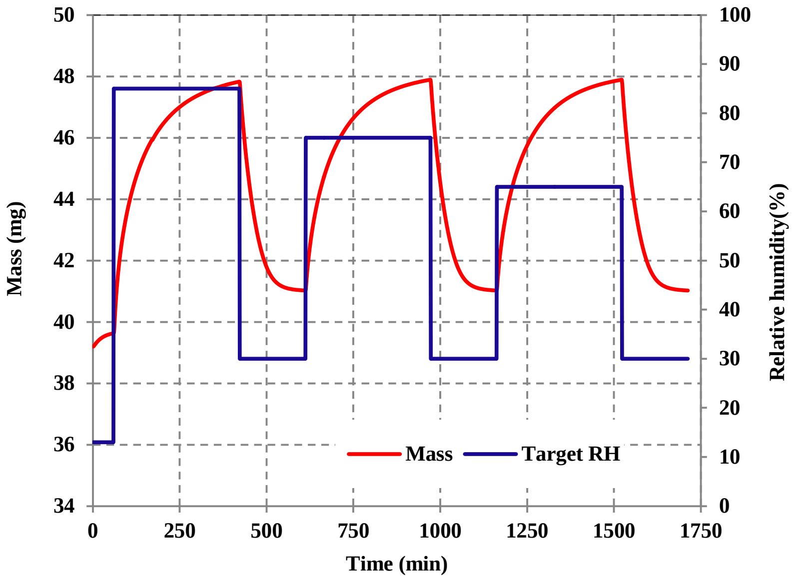

Figure 3.12 Mass change of the aerogel sample due to step changes in the humidity for a cyclic adsorption and desorption process

Table 3.1 Diffusion coefficients for silica aerogels samples

Aerogel Type	Process	Change in Relative Humidity (%) at T=298 K		
		85 to 30	75 to 30	65 to 30
Ammonium hydroxide	Adsorption	$4.70(10^{-10})m^2/s$	$4.42(10^{-10})m^2/s$	$4.37(10^{-10})m^2/s$
	Desorption	$9.27(10^{-10})m^2/s$	$9.14(10^{-10})m^2/s$	$9.15(10^{-10})m^2/s$
Hydrofluoric acid	Adsorption	$8.73(10^{-10})m^2/s$	$8.53(10^{-10})m^2/s$	$8.67(10^{-10})m^2/s$
	Desorption	$1.43(10^{-9})m^2/s$	$1.48(10^{-9})m^2/s$	$1.51(10^{--9})m^2/s$
Potassium hydroxide	Adsorption	$9.15(10^{-11})m^2/s$	$9.11(10^{-11})m^2/s$	$9.19(10^{-11})m^2/s$
	Desorption	$1.68(10^{-10})m^2/s$	$1.72(10^{-10})m^2/s$	$1.65(10^{-10})m^2/s$
Hydrogen peroxide	Adsorption	$7.67(10^{-10})m^2/s$	$7.63(10^{-10})m^2/s$	$6.96(10^{-10})m^2/s$
	Desorption	$1.15(10^{-9})m^2/s$	$1.14(10^{-9})m^2/s$	$1.14(10^{-9})m^2/s$

It can be observed from the values of the diffusion coefficient for silica aerogel prepared using different catalysts that the mass diffusion coefficient for desorption is higher than the mass diffusion coefficient for adsorption/desorption for all three cycles. The values were nearly equal for each adsorption and desorption cycle as the relative difference was not more than 7%. Thus, in the case of silica aerogels, it can be concluded that mass diffusion coefficient is independent of the relative humidity to which the sample is exposed.

3.5.4 Effect of catalyst used in the sol-gel process on mass diffusivity

The diffusion coefficients for silica aerogels depend on their microstructure, which is affected by the catalyst used in the sol-gel process; hence, the diffusion coefficients for different silica aerogels prepared by different catalysts are also different. It can be observed that when hydrofluoric acid was used as the catalyst, the pore size was relatively small (Figure 3.13), and the diffusion coefficient determined was $8.73(10^{-10})$ m^2/s. However, if potassium hydroxide was used as the catalyst, the structure was less dense and the diffusion coefficient was small ($9.13(10^{-11})$ m^2/s) compared to the sample prepared by hydrofluoric acid. In general, when basic catalysts (ammonium hydroxide, potassium hydroxide) were used in sol-gel process, the resulting silica aerogel had a less dense microstructure, and the resulting diffusion coefficients were relatively small. A denser aerogel was obtained when acid catalysts were used and had higher diffusion coefficients by an order of the magnitude.

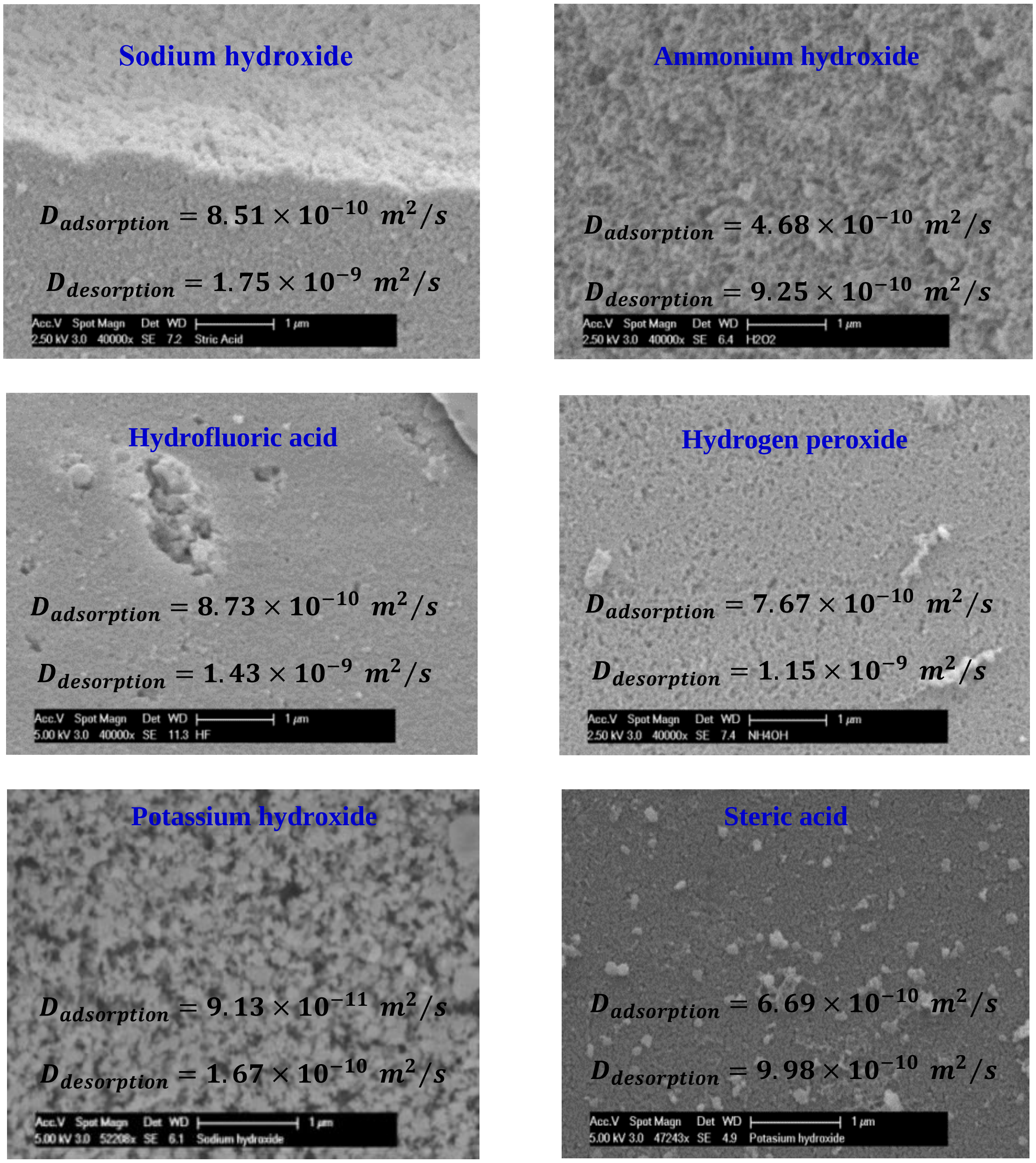

Figure 3.13 Bulk diffusion coefficients for silica aerogel samples prepared by different catalysts.

3.5.5 Effect of temperature on mass diffusivity

In general, the mass diffusivity of desiccants increases with temperature, and it is important to know whether these variations are important in the context of HVAC systems. When two different types of aerogels were subjected to Dynamic Vapor Sorption experiments at different temperatures, the resulting diffusion coefficients (Table 3.2) did not change significantly. The different temperatures used during the experiments are those commonly observed in commercial HVAC systems; therefore, these effects appear unimportant in HVAC systems.

Table 3.2 Diffusion coefficients for silica aerogels samples at different temperatures

Aerogel Type	Process	Temperature of the process (Relative Humidity: 30%-80%)		
		288 K	298 K	308 K
Ammonium hydroxide	Adsorption	$4.75(10^{-10})m^2/s$	$4.70(10^{-10})m^2/s$	$4.68(10^{-10})m^2/s$
	Desorption	$9.17(10^{-10})m^2/s$	$9.27(10^{-10})m^2/s$	$9.25(10^{-10})m^2/s$
Hydrofluoric acid	Adsorption	$8.58(10^{-10})m^2/s$	$8.73(10^{-10})m^2/s$	$8.61(10^{-10})m^2/s$
	Desorption	$1.31(10^{-9})m^2/s$	$1.43(10^{-9})m^2/s$	$1.51(10^{--9})m^2/s$

3.6 Adsorption/desorption isotherms for silica aerogels

3.6.1 Experimental method

The DVS sorption automatic operation (SAO) method was used to set both the desired percent relative humidity steps and the equilibrium criterion. First, each sample was equilibrated to 0% RH using an equilibrium criterion of a change in mass over time (*d*m/*dt*) of no greater than 0.0005% for 5 consecutive minutes. After this equilibrium criterion was reached at 30% RH, the relative humidity was increased automatically to the target value (40%) and equilibrated using the same *d*m/*dt* criterion (0.0005% for 5 consecutive minutes). The relative humidity was increased with an increment of 10% for adsorption cycle. After reaching the equilibrium at 90%, the relative humidity was decreased to 20% RH using a *d*m/*dt* criterion (0.0005% for 5 consecutive minutes) with a decrement of 10%. Sample mass data and sample and reference chamber relative humidity and temperature data were automatically collected every 60 s. A new sample was used for each relative adsorption/desorption cycle and temperature experimental run.

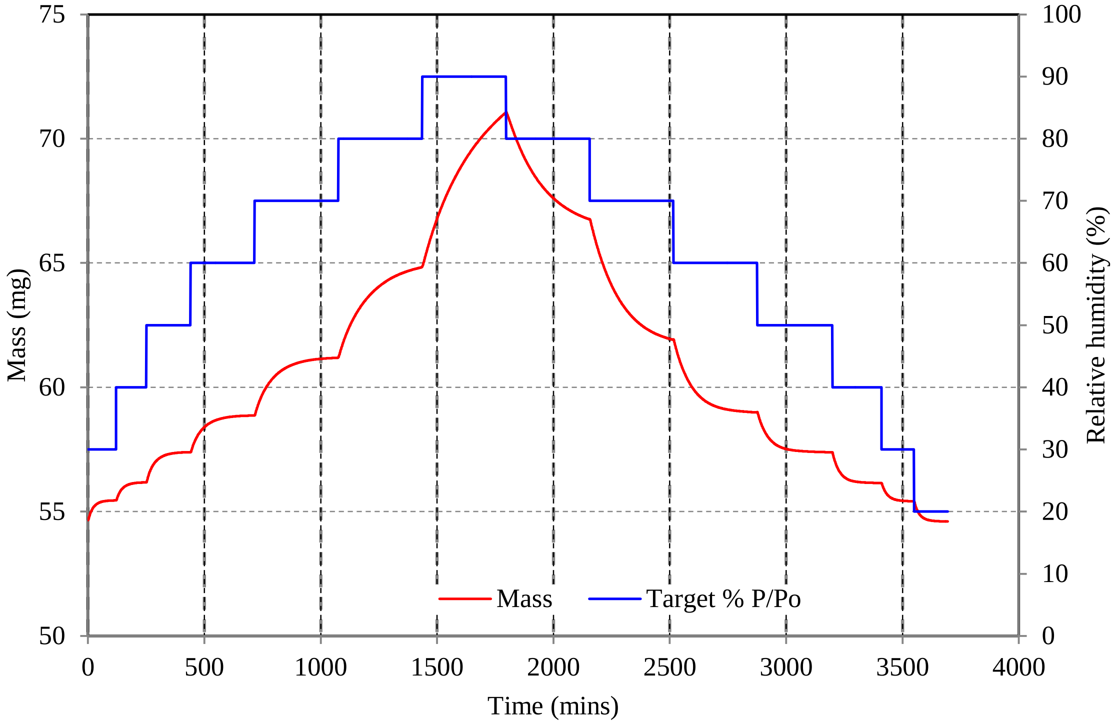

Figure 3.14 Mass change of the sample due to step change in relative humidity

3.6.2 Effect of catalyst used in the sol-gel process on adsorption/desorption isotherms

The adsorption capacity for silica aerogels depends on their microstructure, which is affected by the catalyst used in the Sol-Gel process. A representative adsorption/desorption isotherm is presented in Figure 3.15. It is obvious that the equilibrium isotherm is of type IV, as classified by IUPAC. The adsorption and desorption isotherms do not follow the same path and there is a hysteresis loop, which exists due to capillary condensation.

Adsorption and desorption isotherms for five different type of silica aerogel are presented in figure 3.16 and 3.17. All isotherms are of type IV and the hysteresis exists for all of them. Aerogel prepared by hydrofluoric acid and by ammonium hydroxide has the maximum moisture retention capacity which can be upto 150% of the mass of the dry sample at 90% relative humidity when the equilibrium is reached. While the silica aerogel prepared by hydrogen peroxide and potassium hydroxide can retain moisture only about 80% of the mass of the dry sample under same conditions. The sorption desorption isotherms are also an indicator of the surface area of the microstructure. Hence, based on the equilibrium isotherms data it can be concluded that silica aerogel prepared by hydrofluoric acid and ammonium hydroxide as catalysts have the largest surface area among the five samples prepared by different catalysts.

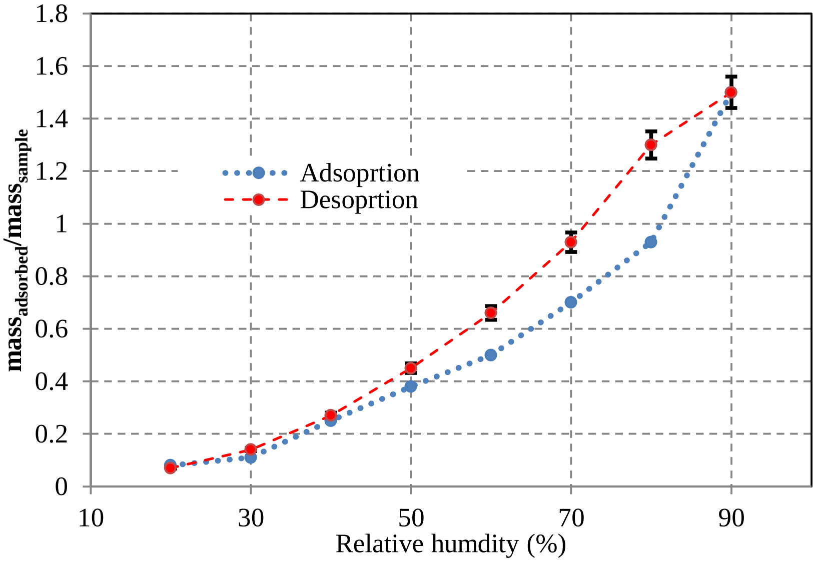

Figure 3.15 Hysteresis in adsorption and desorption isotherms

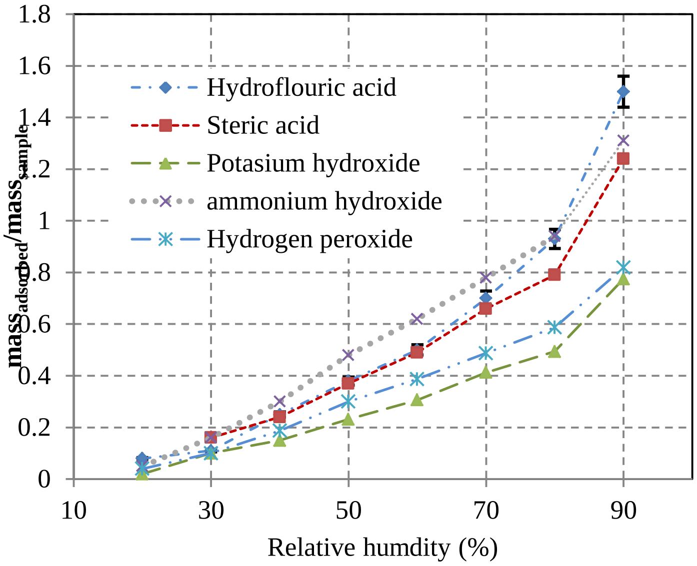

Figure 3.16 Adsorption isotherms of different silica aerogels

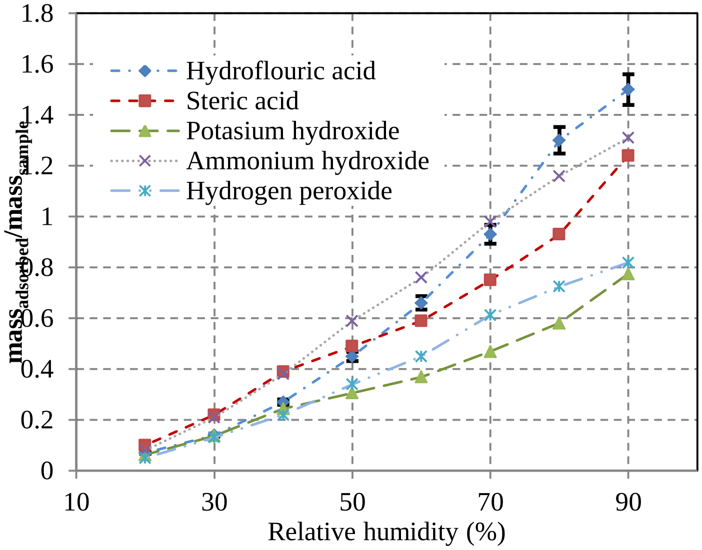

Figure 3.17 Desorption isotherms of different silica aerogels

3.6.3 Effect of temperature on adsorption/desorption isotherms

Moisture adsorption and desorption capacity of the desiccant materials is affected by pressure and temperature. The equilibrium isotherms are always presented with temperature at which the experiments are performed. Desiccants used for dehumidifying applications in HVAC applications typically do not sustain through large temperature differences (ΔT>30^{o}C). Such temperature differences do not affect the diffusion rate significantly ($D_{adsorption}$). However, it is still important to account for the change based on the temperature when the adsorption capacity of a desiccant material is analyzed. Adsorption and desorption isotherms for a silica aerogel prepared by hydrofluoric acid at three different temperatures are presented in Figure 3.18. DVS equilibrium tests for conducted at 15^{o}C, 25^{o}C and 35^{o}C using new samples for each test. As indicated in Figure 3.18, the adsorption capacity of the desiccant increases about 15%, when the experiment temperature is increased from 15^{o}C to 35^{o}C. It is expected that all other silica aerogel samples follow the same trend, *i.e.* that the capacity is increased as the temperature of the environment is increased.

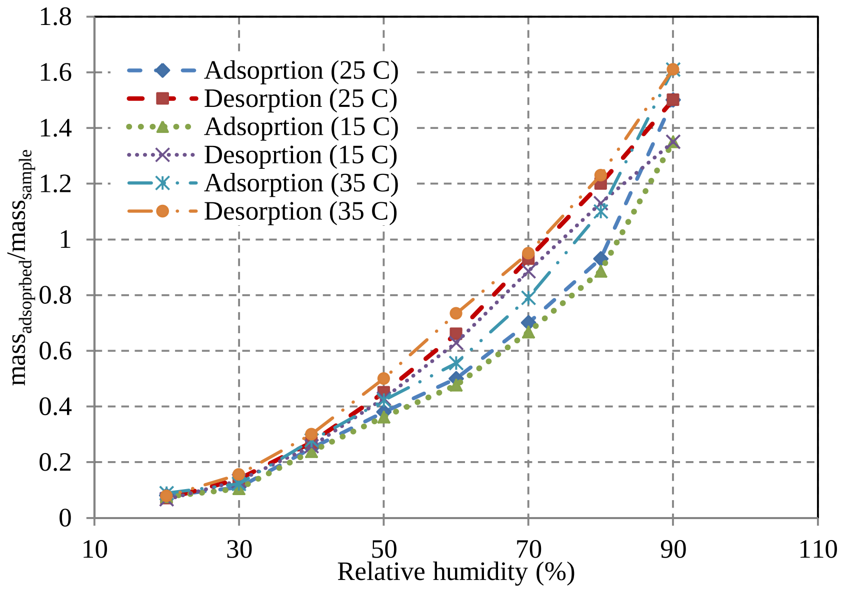

Figure 3.18 Effect of temperature on adsorption/desorption isotherms

3.6.4 Modeling of adsorption isotherms

Adsorption isotherms indicate the moisture adsorption capacity of the desiccants and often represented by models. Some models for curve-fitting adsorption isotherms are presented in Figure 3.3. Adsorption isotherm for different silica aerogel can be modeled by Freundlich equation (Figure 3.3). In Equation 3.3, constant K_F presents the adsorption capacity of the desiccant, while exponent (1/n) shows intensity of adsorption. Adsorption isotherms for different silica aerogel samples were model using Freundlich equation (3) and the resulting constant (K_F) and exponent (n) are presented in the Table 3.3 for comparison.

Table 3.3 Constants of Freundlich equation for adsorption isotherms (Temperature= 25°C)

Desiccant	**K_F (10^5)**	**1/n**	**Reduced chi-square**	**Adjusted R-square**
Hydrofluoric acid	1.72301	2.51371	0.00587	0.97438
Ammonium hydroxide	0.941934	1.81741	0.00209	0.98828
Steric acid	0.55840	2.0922	0.00485	0.96487
Hydrogen peroxide	0.353708	1.808866	0.00077	0.98881
Potassium hydroxide	0.229681	2.10422	0.0016	0.97339

As the adsorption isotherms change with temperature, so the values of K_F and n also changes with temperature. Silica aerogel prepared by hydrofluoric acid has the largest value for K_F, which indicates its better moisture adsorption capacity. Silica aerogel prepared by potassium hydroxide has the least moisture adsorption capacity among five desiccants, as indicated by the smallest value of K_F.

3.7 Conclusions

The sol-gel process was used to prepare a variety of silica aerogels. Different types of acidic and basic catalysts were used in the process. The wet samples were dried using a supercritical drying process with CO_2. Scanning Electron Microscopy was performed to analyze the pore structure of different aerogels. It was found that the catalyst used in the process significantly affects the microstructure. Bulk diffusion is an important mass transport parameter. The diffusion coefficient values were determined using a Dynamic Vapor Sorption instrument, where the dry or wet samples were exposed to sudden changes in environmental humidity. A one-dimensional transient diffusion model was used to calculate the diffusivity of the silica aerogel samples from the measured data. As the diffusion coefficient depends on the microstructure of the porous media, it was found that some silica aerogel prepared by particular catalyst have relatively higher diffusion coefficient compared to others by an order of magnitude. Thus, the type of catalyst used in sol-gel process can change the mass transfer properties of the resulting aerogels. Samples prepared with basic catalysts (ammonium hydroxide) have more porous microstructure and relatively smaller value for diffusion coefficients, while the samples prepared with acidic catalysts (hydrofluoric acid, hydrogen peroxide) have dense microstructures and relatively larger values for diffusion coefficients ($8.73 \times 10^{-10}\ m^2/s$ compared to $9.13 \times 10^{-11}\ m^2/s$ for silica aerogel prepared by potassium hydroxide). The mass diffusivity of silica aerogels depends on the process. The mass diffusion coefficient for desorption was almost twice the mass diffusion coefficient for adsorption. Hence, the moisture desorption process can be performed at faster rate compared to adsorption. Mass diffusion coefficients were found to be independent of the environment humidity. It was found that under typical HVAC operating conditions, the temperature has no significant impact on the mass diffusivity of silica aerogels.

The equilibrium isotherms indicated that adsorption capacity of the silica aerogels also depends on the microstructure of the porous media, which is affected by the catalysts used in the sol-gel process. The silica aerogel prepared by hydrofluoric acid and ammonium hydroxide showed the capacity of about 150% the dry mass of the desiccant. All adsorption/desorption isotherms were of type IV and showed hysteresis, which was observed due the capillary condensation phenomena. The adsorption/desorption capacity of the desiccant is highly affect by the operation temperature. An increase of about 15% was observed when the temperature was increased from 15^{o}C to 35^{o}C.

3.8 References

[3.1] Y. Aristov, G. Restuccia, G. Cacciola, V.N. Parmon, A family of new working materials for solid sorption air conditioning systems, Applied Thermal Engineering 22 (2002) 191–204.

[3.2] B. Dawoud, Y. Aristov, Experimental study on the kinetics of water vapor sorption on selective water sorbents, Silica gel and alumina under typical operating conditions of sorption heat pumps, International Journal of Heat and Mass Transfer 46 (2003) 273–81.

[3.3] X.J. Zhang, K. Sumathy, Y.J. Dai, R.Z. Wang, Parametric study on the silica gel–calcium chloride composite desiccant rotary wheel employing fractal BET adsorption isotherm, International Journal of Energy Research 29(1) (2005) 37–51.

[3.4] R.W. Besant, C.J. Simonson, Air-to-air exchangers, ASHRAE Journal 45 (4) (2003) 2-9.

[3.5] S.A. Omer, S.B. Riffat, G. Qiu, Thermal insulation for hot water cylinder: A review and a conceptual evaluation, Building Service Engineering Research and Technology 28 (3) (2007) 275–293.

[3.6] M.S. Ahmed, Y.A. Attia, Materials for photocatalytic detoxification of cyanide wastes in water, Journal of Non-Crystalline Solids 186 (1995) 402-407.

[3.7] I. Smirnova, S. Suttiruengwong, M. Seiler, W. Arlt, Dissolution rate enhancement by adsorption of poorly soluble drugs on hydrophilic silica aerogels, Pharmaceutical Development and Technology 9 (2004) 443–452.

[3.8] A.A. Pesaran, A.F. Mills, Moisture transport in silica gel packed beds-I: Theoretical study, International Journal of Heat and Mass Transfer 30 (1987) 1037–1049.

[3.9] I. Smirnova, S. Suttiruengwong, W. Arlt, Feasibility study of hydrophilic and hydrophobic silica aerogels as drug delivery systems, Journal of Non-Crystalline Solids 350 (2004) 54–60.

[3.10] S. Kistler, Coherent expanded aerogels and jellies, Nature 127 (1931) 741.

[3.11] H. Goda, C.W. Frank, Fluorescence studies of the hybrid composite of segmented-polyurethane and silica, Chemistry of Materials 13 (2001) 2783–2787.

[3.12] A.C. Pierre, G.M. Pajonk, Chemistry of aerogels and their applications, Chemical Reviews 102 (2000) 4243–4265.

[3.13] J. Aguado-Serrano, M.L. Rojas-Cervantes, Titania aerogels: Influence of synthesis parameters on textural, crystalline, and surface acid properties, Microporous and Mesoporous Materials 88 (2006) 205–213.

[3.14] N.D. Hegde, H. Hirashima, A.V. Rao, Two step sol–gel processing of TEOS based hydrophobic silica aerogels using trimethylethoxysilane as a co-precursor, Journal of Porous Materials, 14 (2007) 165–171.

[3.15] D.Y. Nadargi, S.S. Latthe, A.V. Rao, Effect of post-treatment (Gel ageing) on the properties of methyltrimethoxysilane based silica aerogels Prepared by two-step sol–gel process, Journal of Sol–Gel Science and Technology, 49 (2009) 53–59.

[3.16] T. Gerber, The subcritical preparation of aerogels based on sodium water glass, Journal of Sol–Gel Science and Technology 13 (1998) 323–328.

[3.17] G.S. Kim, S.H. Hyun, H.H. Park, Synthesis of low dielectric silica aerogel films by ambient drying, Journal of the American Ceramic Society 84 (2001) 453–455.

[3.18] J.L. Gurav, D.Y. Nadargi, A.V. Rao, Effect of mixed catalysts system on TEOS-based silica aerogels dried at ambient pressure, Applied Surface Science 255 (2008) 3019-3027.

[3.19] J.L. Gurav, A.V. Rao, U.K.H. Bangi , Hydrophobic and low density silica aerogels dried at ambient pressure using TEOS precursor, Journal of Alloys and Compounds 47 (2009) 296–302.

[3.20] B.L. Newalkar, S. Komarneni, Synthesis and characterization of microporous silica prepared with sodium silicate and organosilane compounds, Journal of Sol–Gel Science and Technology 18 (2000) 191–198.

[3.21] I. Artaki, T.W. Zerda, J. Jonas, Solvents effects on the condensation stage of the sol-gel process, Journal of Non-Crystalline Solids 81 (1986) 381–395.

[3.22] E. Economopoulos, T. Ioannides, Synthesis of transparent silica aerogels using tetraalkylammonium fluoride catalysts, Journal of Sol–Gel Science and Technology, 49 (2009) 347–354.

[3.23] M. Alnaief, I. Smirnova, Functionalized silica aerogels for advanced drug carrier systems, PhD Thesis, Technical University of Hamburg, Germany, 2011.

[3.24] C.J. Brinker, G.W. Scherer, Sol-Gel Science, The Physics and Chemistry of Sol-Gel Processing, Academic Press Inc. 1990.

[3.25] S.S. Prakash, C.J. Brinker, A.J. Hurd, Silica aerogel films at ambient pressure, Journal of Non-Crystalline Solids 190 (1995) 190-275.

[3.26] G.W. Scherer, H. Hdach, J. Phalippou, Thermal expansion of gels: A novel method for measuring permeability, Journal of Non-Crystalline Solids 130 (1991) 157-170.

[3.27] L. Pel, H. Brocken, K. Kopinga, Determination of moisture diffusivity in porous media using moisture concentration profiles, International Journal of Heat and Mass Transfer 39 (1996) 1273-1280.

[3.28] J. Shen, Z. Zhang, G. Wu, B. Zhou, X. Ni, J. Wang, Preparation and characterization of silica aerogels derived from ambient pressure, Journal of Material Science Technology 22 (2006) 798-802.

[3.29] E.M. Lucas, M.S. Doescher, D.M. Ebenstein, K.J. Wahl, D.R. Rolison, Silica aerogels with enhanced durability, 30-nm mean pore-size, and improved immersibility in liquid, Journal of Non-Crystalline Solids 350 (2004) 244-252.

[3.30] I. Mamaligai, W. Schabel, S. Petrescui, Characterization of water vapor diffusion into spherical silica gel particles, REV CHIM BUCHAREST (2010) 61.

[3.31] A. Yadav, V.K. Bajpai, Experimental comparison of various solid desiccants for regeneration by evacuated solar air collector and air dehumidification, Drying Technology 30 (2012) 516-525.

[3.32] A.A. Pesaran, A.F. Mills, Moisture transport in silica gel packed beds- II. Experimental study, International Journal of Heat and Mass Transfer 30 (1987) 1051–1060.

[3.33] R.E. Cunningham, R.J. Williams, Diffusion in Gases and Porous Media, New York Plenum 1980.

[3.34] I. Hopkinson, R.A.L. Jones, S. Black, D.M. Lane, P.J. McDonald, Fickian and case II diffusion of water into amylase: A stray field NMR study, Carbohydrate Polymers 34 (1997) 39-47

[3.35] S. Chemkhi, F. Zagrouba, Water diffusion coefficients in clay material from drying aata, Desalination 185 (2005) 491-498.

[3.36] V.T. Karathanos, G.D. Saracacos, Porosity and pore size distribution of starch materials, Journal of Food Science 19 (1992) 259-280.

[3.37] G. Spieles, T. Marx, I. Heschel, G. Rau, Analysis of desorption and diffusion during secondary drying in vacuum freeze-drying of hydroxyethyl starch, Chemical Engineering and Processing 34 (1995) 351-357.

[3.38] C.J. Lomauro, A.S. Bakshi, T.P. Labuza, Moisture transfer properties of dry and semi-moist food, Journal of Food Science 50 (1985) 397-400.

[3.39] V. Steckel, C.M. Clemons, H. Thoemen, Effects of material parameters on the diffusion and sorption properties of wood-flour/polypropylene composites, Journal of Applied Polymer Science 103 (2007) 752-763.

[3.40] D.S. Valkovska, K.D. Danov, Determination of bulk and surface diffusion coefficients from experimental data for thin liquid film drainage, Journal of Colloid and Interface Science 223 (2000) 314-316.

[3.41] A.D. Romman-Gutierrez , F. Mabille, S. Guilbert, B. Cuq, Contribution of specific flour components to water vapor adsorption properties of wheat flours, Cereal Chemistry 80 (5) (2003) 558-563.

[3.42] D.J. Burnett, A.R. Garcia, F. Thielmann, Measuring moisture sorption and diffusion kinetics on proton exchange membranes using gravimetric vapor sorption apparatus, Journal of Power Sources 160 (2006) 426-430.

[3.43] E. Roca, V. Guillard, S. Guilbert, N. Gontard, Moisture migration in a cereal composite food at high water activity: Effects of initial porosity and fat content, Journal of Cereal Science 43 (2006) 144-151.

[3.44] X.Yu, A.R. Schmidt, L.A. Bello-Perez, S.J. Schmidt, Determination of the bulk moisture diffusion coefficient for corn starch using an automated water sorption instrument, Journal of Agricultural Food Chemistry 56 (2008) 50–58.

[3.45] N.A. Peppas, L.B. Peppas, Water diffusion and sorption in amorphous macromolecular systems and food, Journal of Food Engineering 22 (1994) 189-210.

[3.46] N.S. Bolan, R. Naidu, J.K. Syers, R.W. Tillman, Surface charge and solute interactions in soils. Advanced Agronomy 67 (1999) 87–140.

[3.47] J.J. Pignatello, The measurement and interpretation of sorption and desorption rates for organic compounds in soil media. Advanced Agronomy 69 (2000) 1–73.

[3.48] W. Huang, P. Peng, Z. Yu, J. Fu, Effects of organic matter heterogeneity on sorption and desorption of organic contaminants by soils and sediments Applied Geochemistry 18 (2003) 955–972.

[3.49] G. Limousin, J.P. Gaudet, L. Charlet , S. Szenknect, V. Barthe`s, M. Krimissa, Sorption isotherms: A review on physical bases, modeling and measurement, Applied Geochemistry 22 (2007) 249–275.

[3.50] E.P. Ng, S. Mintova, Nanoporous materials with enhanced hydrophilicity and high water sorption capacity, Microporous and Mesoporous Materials 114 (2008) 1-26.

[3.51] Z. Knez, Z. Novak, Adsorption of water vapor on silica, alumina, and their mixed oxide aerogels, Journal of chemical Engineering Data 46 (2001) 858-860.

[3.52] Z. Novek, S. Štandeker, Z. Knez, Adsorption of BTEX vapors using modified silica aerogels of different hydrophobicity (open source)

[3.53] F. Rouquerol, J. Rouquerol, K. Sing, Adsorption by Powders and Porous Solids: Principles, Methodology and Applications, Elsevier Ltd.1999.

[3.54] S. Naumov, Hysteresis Phenomena in Mesoporous Materials, PhD dissertation, Leipzig University, 2009.

[3.55] I. Langmuir, The constitution and fundamental properties of solids and liquids, Journal of American Chemical Society 38 (11) (1916) 2221–2295.

[3.56] J.H. De Boer, The Dynamical Character of Adsorption, second ed., Oxford University Press, London, 1968.

[3.57] A.L. Myers, J.M. Prausnitz, Thermodynamics of mixed gas adsorption, AIChE Journal 11 (1) (1965) 121–129.

[3.58] M.M. Dubinin, The potential theory of adsorption of gases and vapors for adsorbents with energetically non-uniform surface, Chemical Review 60 (1960) 235–266.

[3.59] K.Y. Foo, B.H. Hameed, Insights into the modeling of adsorption isotherm systems: Review, Chemical Engineering Journal 156 (2010) 2–10.

[3.60] A. Malek and S. Farooq, Comparison of Isotherm Models for Hydrocarbon Adsorption on Activated Carbon, AIChE Journal 11 (42) (1996) 3191–3201.

[3.61] Y. S. Ho, J. F. Porter, G. McKay, Equilibrium isotherm studies for the sorption of divalent metal ions onto peat: copper, nickel and lead single component system, Water, Air, and Soil Pollution 141 (2002) 1–33.

Chapter 4- Adsorption and desorption performance of silica aerogel coated metal foams

4.1 Introduction

Because of the importance of energy efficiency in buildings, there is significant interest in separating the sensible and latent loads when conditioning air for human comfort. Separating the sensible and latent loads offers significant potential in energy savings (unlike the conventional single vapor compression cycle systems, the cooling up to the dew point and reheat process are not required) and provides opportunities for improved control of temperature and humidity (there are different components for sensible and latent loads working independently). Many recent studies of dehumidification systems have focused on the development of solid adsorbent systems that can provide improved sorption capacity and higher mass and heat transfer rates, as well as favorable equilibrium isotherms [4.1–4.3]. Adsorption systems with improved performance result in substantial decreases in the initial and operating costs and in some cases make such dehumidification systems attractive alternatives to existing vapor compression systems for cooling and dehumidification. In general, the salt adsorbents, such as calcium chloride, have better moisture absorbing capacity than the organic adsorbents, such as silica gel, but deliquescence occurs on the surface of calcium chloride granules beyond a certain adsorption level and a hydrate solution is formed). This behavior limits the effectiveness of salt desiccants

[3]. In order to overcome this problem, desiccant materials based on silica aerogel have become an attractive alternative to the existing salt-based adsorbents. They have been used as a high-performance desiccant to remove water vapor from humid ventilation air for buildings [4.4]. There is no chemical reaction involved during adsorption and desorption. Even when saturated with water vapor, silica gel still has a dry appearance with its geometry unchanged, which is an advantage over liquid desiccant systems.

The solid desiccant can be deployed by coating a solid substrate. The characteristics of the substrate, such as surface area and thermal conductivity, affect the moisture removal performance considerably. Therefore, an appropriate dehumidification performance evaluation of the desiccant coated on the substrate is important. One potential candidate for a substrate material is metal foam. There has been considerable interest in establishing the thermal-hydraulic performance of metal foams when used as a heat exchanger. Despite manufacturing and implementation issues, these materials hold promise as both heat exchangers and heat sinks [4.5-4.8]. The open porosity, low relative density, high thermal conductivity, large surface area per unit volume, and the ability to enhance fluid mixing can make metal foam thermal management devices efficient, compact, and light-weight. Two major advantages of using metal foams as substrates are the large surface area per unit volume and a thermal conductivity higher than that of the desiccant. A relatively large quantity of silica aerogel can be deployed as thin coating on the foam, and the higher thermal conductivity of the foam assists in removing the heat of adsorption and can provide heat for desorption as shown in Figure 4.1 [4.9]. In Chapter 3, the adsorption and desorption rate and equilibrium capacity of solid silica aerogel was analyzed, while current chapter is focused on evaluating the dehumidification performance of aerogel-coated metal foams.

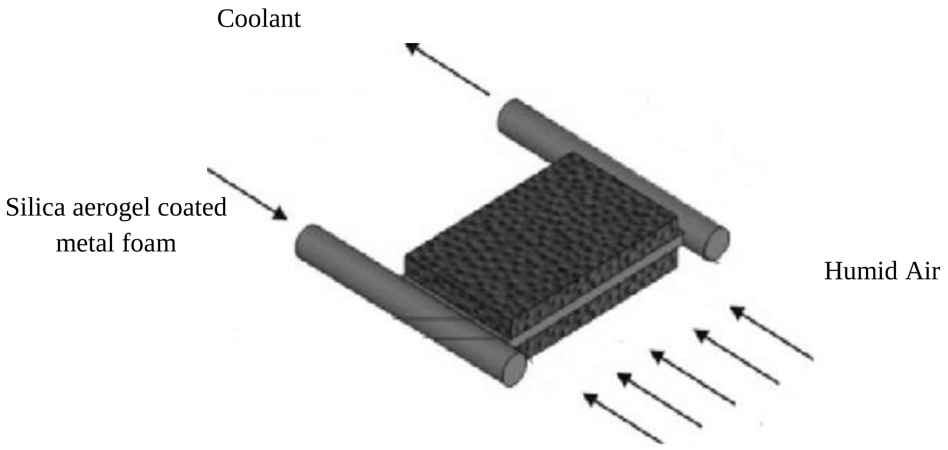

Figure 4.1 A configuration for aerogel coated metal foam dehumidification device

The adsorption and desorption characteristics of different silica gel coatings may vary because of different manufacturing procedures [4.3]. Although silica gel is frequently used as a desiccant, the transport of heat and moisture within the pores of silica gel particles is complex and research is ongoing. Comprehensive experimental studies of the physicochemical properties and some research applications of the organic and salt-based adsorbents have been reported by Aristov *et al.* [4.1] and Zhang *et al.* [4.3]. These studies show that silica-aerogel-based adsorbents have a higher adsorption capacity and can be regenerated with a lower temperature than the other commercially available desiccants, such as activated carbon. Despite such promising properties, conclusions as to the feasibility of these materials for sorption systems can only be drawn after dynamic analysis of the adsorption and desorption performance of the silica aerogel coated on the substrate under realistic operating conditions. The capacity of a porous adsorbent solid in adsorption of an adsorbate gas is determined by the adsorption isotherm, and the mass diffusivity affects the adsorption rate. However, the dynamic adsorption properties of adsorbents with different microstructures have not been widely reported, and this is especially true for the solid side mass diffusivity of aerogels coated on a metal foam surfaces. The main objective of the present work is to investigate the dynamic properties and desiccant mass diffusivity of different silica aerogels coated on metal foams.

4.2 Literature review

4.2.1 Preparation of silica aerogel coatings

Despite significant advances in technologies based on sol-gel thin film process, there has been relatively little effort directed toward understanding the fundamentals of sol-gel coating processes. Dip coating is one way to deposit a thin layer of a desiccant on a substrate surface. In dip coating, the substrate is normally withdrawn vertically from the coating bath at a constant speed [4.10]. The moving substrate pulls liquid out of the bath, retaining a liquid layer, the thickness of which depends on substrate surface condition, speed of withdrawal, liquid properties, and ambient conditions. Since the solvent is evaporating and draining, the liquid film acquires a wedge-like shape that terminates at a well-defined drying line. When the receding drying line velocity equals the withdrawal speed, the process is in steady state with respect to the liquid bath surface.

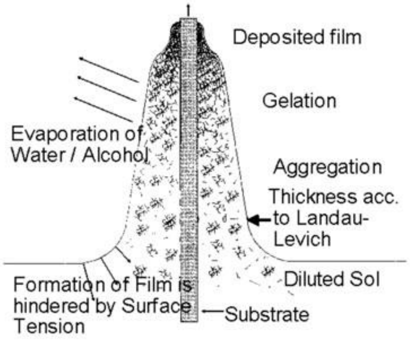

Figure 4.2 Gelation process during dip coating process [4.10]

The hydrodynamics dip coating (pure liquids, ignoring evaporation) was first calculated correctly by Landau and Levich [4.11] and later was generalized by Wilson [4.12]. Scriven [4.13] conducted a review of the progress of the dip coating process and stated that the thickness of the deposited film is related to the position of the intersection of the upward and downward moving layers. He found that the competition between six forces in the film deposition region governed the film thickness and position of the streamline. These forces included (1) viscous drag upward on the liquid by the moving substrate; (2) force of gravity; (3) resultant force of surface tension in the concavely shaped meniscus; (4) inertial force of the boundary layer liquid arriving at the deposition region; (5) surface tension gradient; and (6) the disjoining (or conjoining) pressure (important for films less than 1 micron thick).

4.2.2 Effect of substrate characteristics on adsorption/desorption performance

For dehumidification systems containing solid desiccants, absorbent materials are often deployed on substrates. These substrates can be metallic or non-metallic. Commonly used materials for such applications include aluminum, stainless steel or fiber paper, which provides structural integrity and strength. The substrate heat capacity improves both the sensible and the latent heat recovery performance of the enthalpy recovery wheel, due to reduced fluctuations of desiccant temperature during the wheel operation. However, axial heat conduction through the substrate reduces the sensible heat recovery performance of the enthalpy recovery wheel and has little impact on the latent heat recovery performance of the wheel [4.14]. The most common type of substrate geometry currently used in dehumidification systems consists of a honeycomb structure. The honeycomb structure of the desiccant wheel was developed by Carl Munter, a Swedish inventor, in the late 1950's for low humidity applications in the defense industry [4.15]. Early desiccant wheels used honeycomb paper impregnated with lithium chloride, which functioned as the desiccant. The airflow channels can have different shapes such as triangle, sinusoidal and square, but the sinusoidal shape is preferred [4.16]. The sinusoidal shape results in better mixing and hence uniform humidity.

The effect of substrate characteristics on the overall performance of dehumidification systems is often ignored, as pointed out by Ge *et al.* [4.17]. The extensive review of the literature related to heat and mass transfer in dehumidification systems resulted in the conclusion that most of the time, the effect of substrate is ignored for simplicity and convenience, while analyzing the performance of enthalpy wheels. Joeng and Mumma [4.18] analyzed the two most common desiccant materials, silica gel and molecular sieve on aluminum substrate. They compared the heat conduction in the axial direction through the matrix and the aluminum substrate. Sphaier and Worek [4.19] developed a combined heat and mass transfer model. The proposed model can be extended to include the effect of supporting medium. Nawaz *et al.* [4.20] conducted a study on the use of metal foams as substrates for silica aerogels. An analytical model was developed for the desiccant-coated metal foam for simultaneous heat and mass transfer, including metal foam and desiccant characteristics. The model was used to predict the dehumidification performance of desiccant coated metal foam.

4.3 Preparation of silica aerogel coated samples

Silica aerogel coated metal foam samples were prepared using a dip coating method. Metal foams with pore size of 4.02 mm (5 PPI), 3.28 mm (10 PPI) and 2.58 mm (20 PPI) were used for this study. Small metal foam blocks with dimensions of about 8 mm were machined for coating. Wet silica gels were prepared using silicon alkoxide precursor, tetramethyl orthosilicate

(TMOS, Si $(OCH_3)_4$). The formation of a wet gel coating by TMOS is presented by equation (3.5) in Chapter 3.

The kinetics of the above reaction is impracticably slow at room temperature, often requiring several days to reach completion. For this reason, acid or base catalysts are added to the formulation. The amount and type of catalyst used in synthesis played key role in the microstructural, physical, and optical properties of the final aerogel product as will be explained later in the section. Acid catalysts included hydrofluoric acid and hydrogen peroxide. Basic catalysts used were ammonium hydroxide and potassium hydroxide. During the gelation process, metal foam samples were dipped in the viscous solution and were removed at moderate speed (about 0.5cm/s). It was important to perform the process an appropriate speed to try to obtain a uniform coating. Leaving the sample in the gel solution for long time would cause the resulting sample to have solid gel particles in the pores. It is important to note the difference between hydrolysis and condensation reaction involved in sol-gel process. Hydrolysis is the process when two metal alkoxides react with water to form the hydroxides (equation 4.1a), while condensation is the process by which two metal hydroxides combines to form the metal oxides (alcohol condensation-equation 4.1b,water condensation-equation 4.1c).

$$\equiv Si - OR + H_2O \rightarrow \equiv Si - OH + ROH \qquad (4.1a)$$

$$\equiv Si - OR + Si - OH \rightarrow \equiv Si - O - Si + ROH \qquad (4.1b)$$

$$\equiv Si - OH + Si - OH \rightarrow \equiv Si - O - Si \equiv + H_2O \qquad (4.1c)$$

When a sol reaches the gel point, it cannot be assumed that the hydrolysis and condensation reactions of the silicon alkoxide reactant are complete. The gel point simply represents the time at which the polymerizing silica species span the container containing the sol. At this point, the silica backbone of the gel contains a significant number of unreacted alkoxide groups. In fact, hydrolysis and condensation can continue for much longer times compared to the time required for gelation. For this reason, sufficient time was given for the strengthening of the silica network, and the gels on the coated samples were kept in this solution for up to 48 hours.

The final and most important step in making silica aerogel-coated samples is drying, where the liquid within the gel is removed, leaving only the linked silica network. The wet gel can be dried either by evaporation or by supercritical drying with CO_2 or alcohols. It is important to observe that the geometric characteristics of metal foam after coating change. The 5 PPI metal foam samples before and after coating process is shown in Figure 4.3. The geometric characteristics of metal foams samples before and after coating are presented in Table 4.1.

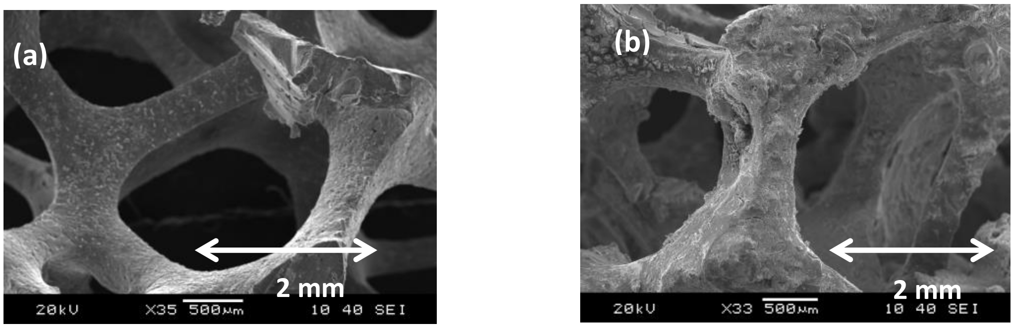

Figure 4.3 5 PPI metal foams (a) Uncoated and (b) Coated with silica aerogel (catalyst: ammonium hydroxide)

Table 4.1 Geometric Properties of Coated and Uncoated Metal Foams

Type of Foam (PPI)	Ligament Diameter (mm)		Pore Diameter (mm)	
	Uncoated	Coated	Uncoated	Coated
5	0.50	0.58	4.02	3.94
10	0.45	0.52	3.28	3.21
20	0.35	0.39	2.58	2.54

The process for the preparation of silica-aerogel-coated metal foams is summarized in the flow chart given in Figure 4.4.

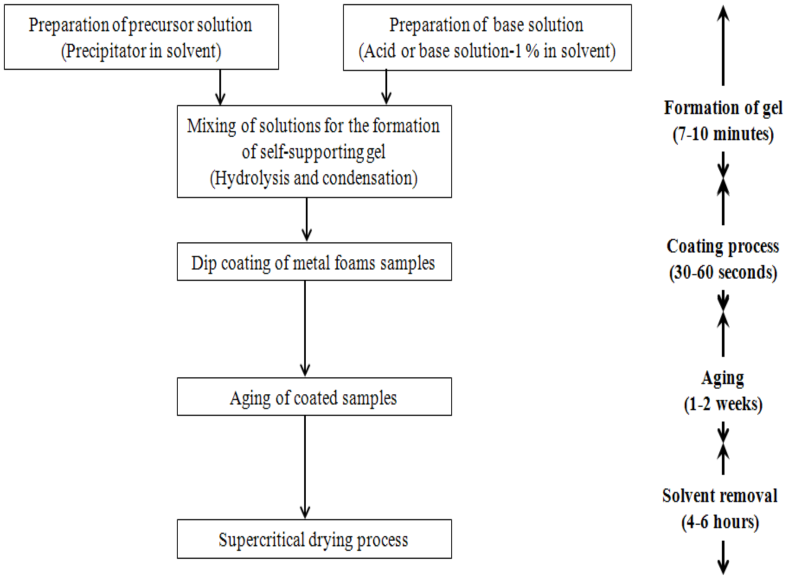

Figure 4.4 Manufacturing of silica aerogel coated metal foams (Adopted from Brinker and Scherer [3.22] and modified)

In order to confirm the successful coating, an EDX (Energy dispersive X-Rays) analysis (Jeol 6060LV-*Jeol Ltd*., Material Research Laboratory, University of Illinois at Urbana Champaign) was carried out where a coated flat aluminum surface was compared to a bare uncoated surface. The results (Figure 4.5) confirmed that the coated surface consisted of silicon oxide, the main ingredient of silica aerogel, whereas the bare surface (uncoated) showed the presence of aluminum oxide. The same procedure was repeated for metal foam surface and EDX analysis showed the successful coating on the metal foam surface as well.

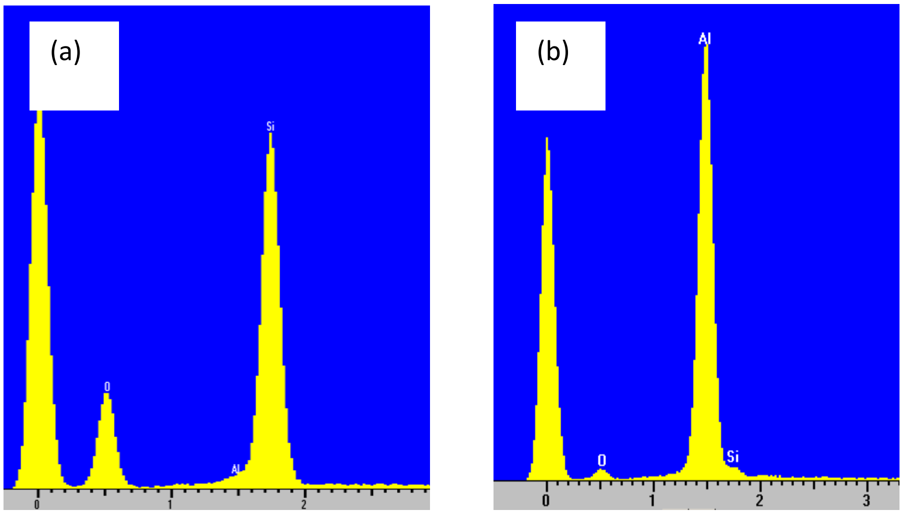

Figure 4.5 EDX analysis of two different aluminum surfaces (a) Dip coated with silica aerogel (b) Uncoated surface

4.4 Moisture diffusivity of silica aerogel coated metal foams

As both equilibrium and transient adsorption/desorption behavior of the desiccant are affected by the microstructure (pore size), it is important to determine which catalyst will result in an appropriate pore size range and hence will absorb/desorb more moisture at relatively faster rates compared to the others. Furthermore, as the substrate can also affect the adsorption/desorption rate, the effect of different types of metal foams used a substrates should be evaluated as well.

4.4.1 Determination of mass diffusion coefficient

One-dimensional transient diffusion equation for a thin cylindrical annulus is presented by equation (4.2)

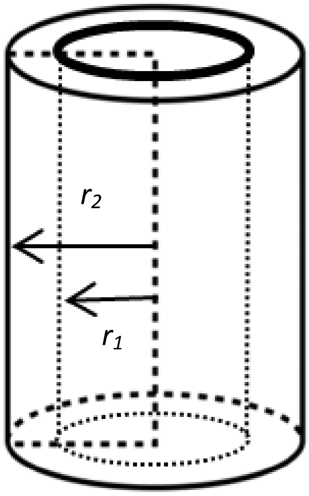

Figure 4.6 Sample geometry for the development of model

$$\frac{\partial \rho}{\partial t} = -D\left(\frac{\partial^2 \rho}{\partial r^2} + \frac{1}{r}\frac{\partial \rho}{\partial r}\right) \tag{4.2}$$

The appropriate initial and boundary conditions for the model used in this study are represented by equation (4.3a) and, (4.3b) and (4.3c) respectively,

$$\rho(r, t = 0) = \rho_o \tag{4.3a}$$

$$\rho(r = r_2, t) = \rho_\infty \tag{4.3b}$$

$$\frac{\partial \rho}{\partial r}(r = r_1, t) = 0 \tag{4.3c}$$

The initial water concentration (density) of water vapor in the sample was zero, as the sample was dried to remove any vapor. The initial and boundary conditions specified above correspond to typical conditions found in gravimetric adsorption experiments, where the sample is contained in a sample holder and water adsorption occurs across the outer surface of the sample. It is important to note the similarities and differences of current analysis with the study presented in Chapter 3. Current model involves a solid impermeable cylinder over which there is an annular desiccant coating, while the model developed in Chapter 3 is for a cylindrical solid desiccant. However the boundary condition at the surface presents the infinitely fast diffusion for both cases. The solution to Fick's second law for a dilute solution can be represented by equation (4.4) for the annular coating of desiccant on a circular cylinder.

$$\frac{\rho-\rho_\infty}{\rho_o-\rho_\infty}=\sum_{n=0}^{\infty}C_n[Y_0(\lambda_n\eta)J_0(\lambda_n)-Y_0(\lambda_n)J_0(\lambda_n\eta)]exp\left[-\frac{D{\lambda_n}^2t}{r_2^2}\right] \quad (4.4)$$

$$C_n=\frac{\int_{\eta_1}^{1}\eta[Y_0(\lambda_n\eta)J_0(\lambda_n)-Y_0(\lambda_n)J_0(\lambda_n\eta)\,]d\eta}{\int_{\eta_1}^{1}\eta[Y_0(\lambda_n\eta)J_0(\lambda_n)-Y_0(\lambda_n)J_0(\lambda_n\eta)\,]^2d\eta} \quad (4.5)$$

where λ_n are the eigenvalues satisfying the equation (4.6),

$$Y_0(\lambda_n)J_1(\lambda_n\eta_1)=Y_1(\lambda_n\eta_1)J_0(\lambda_n) \quad (4.6)$$

Where r_1 and r_2 are the radii of the bare metal foam ligament and the silica aerogel coated ligament, respectively. $\eta=r/r_2$ is the dimensionless length ($\eta_1=r_1/r_2$). J_0 and Y_0 are the Bessel functions of first and second kind of order zero, J_1 and Y_1 are the Bessel functions of first and second kind of order one, ρ is defined as the mass density of water uptake at time t, ρ_∞ is the mass density of water uptake as time approaches infinity, and ρ_o is the initial mass density at the start of the process.

Representative experimental data and the resulting curve fit for determining the diffusion coefficient are shown in Figures 4.7 and 4.8, respectively. The sample for these runs was prepared using ammonium hydroxide as the catalyst and methanol and tetra-methyl orthosilicate as the solvent and precipitator. The resulting diffusion coefficients were 4.63 (10^{-10}) m^2/s and 9.42 (10^{-10}) m^2/s for adsorption and desorption, respectively. By the same procedure, the diffusion coefficients for a sample prepared using hydrofluoric acid as the catalyst were determined to be 8.65 (10^{-10}) m^2/s and 1.37 (10^{-9}) m^2/s for adsorption and desorption, respectively. The uncertainty in calculating the diffusion coefficient was 1.5% based on the uncertainty of mass balance (10 micrograms).

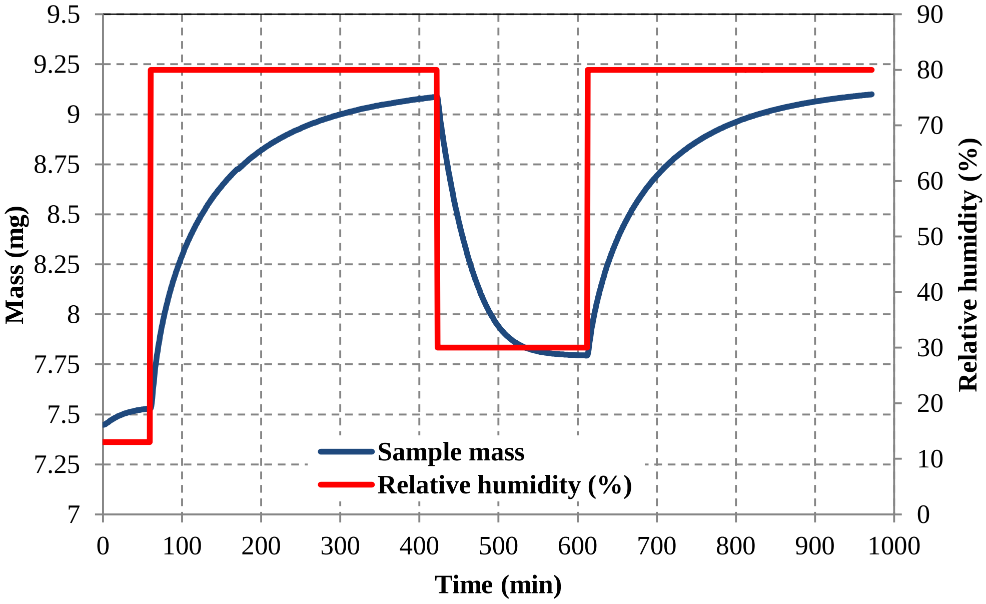

Figure 4.7 Mass variation of the sample due to step change in humidity

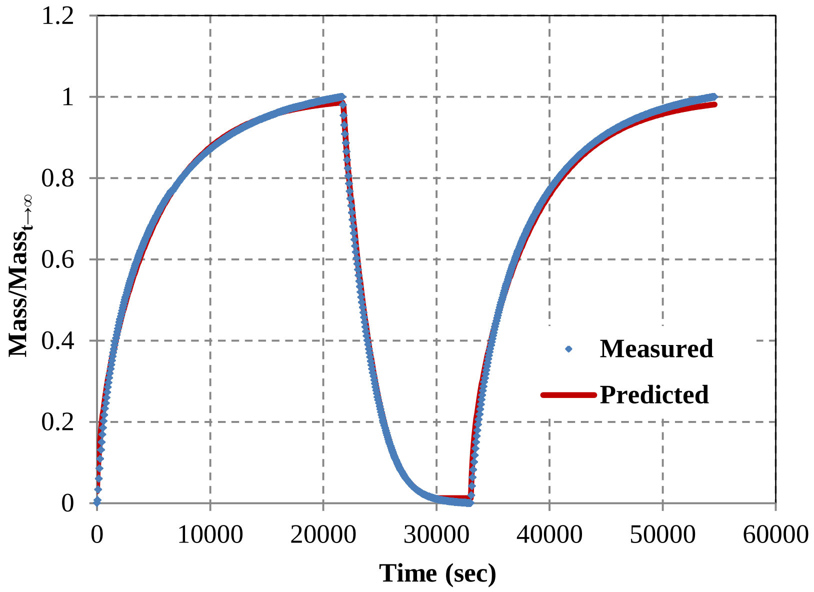

Figure 4.8 Measured and predicted mass variation (Equation 4 with D=4.698(10^{-10}) m^2/s for ammonium hydroxide (catalyst) sample)

4.4.2 Effect of catalyst used in sol-gel process on mass diffusivity

The diffusion coefficients for coated silica aerogels depend on the microstructure, which is affected by the catalyst used in the sol-gel process; hence, the diffusion coefficients for different silica-aerogel-coated metal foams prepared using different catalysts are also different. It can be observed that when hydrofluoric acid was used as the catalyst, the pore size was relatively small (Figure 4.9), and the adsorption diffusion coefficient determined is 8.65 (10^{-10}) m^2/s. However, if potassium hydroxide was used as a catalyst, the average pore size was relatively large (less dense structure) and the adsorption diffusion coefficient was smaller (9.13(10^{-11}) m^2/s) compared to the sample prepared using hydrofluoric acid. Similar trends can be observed for desorption diffusion coefficients.

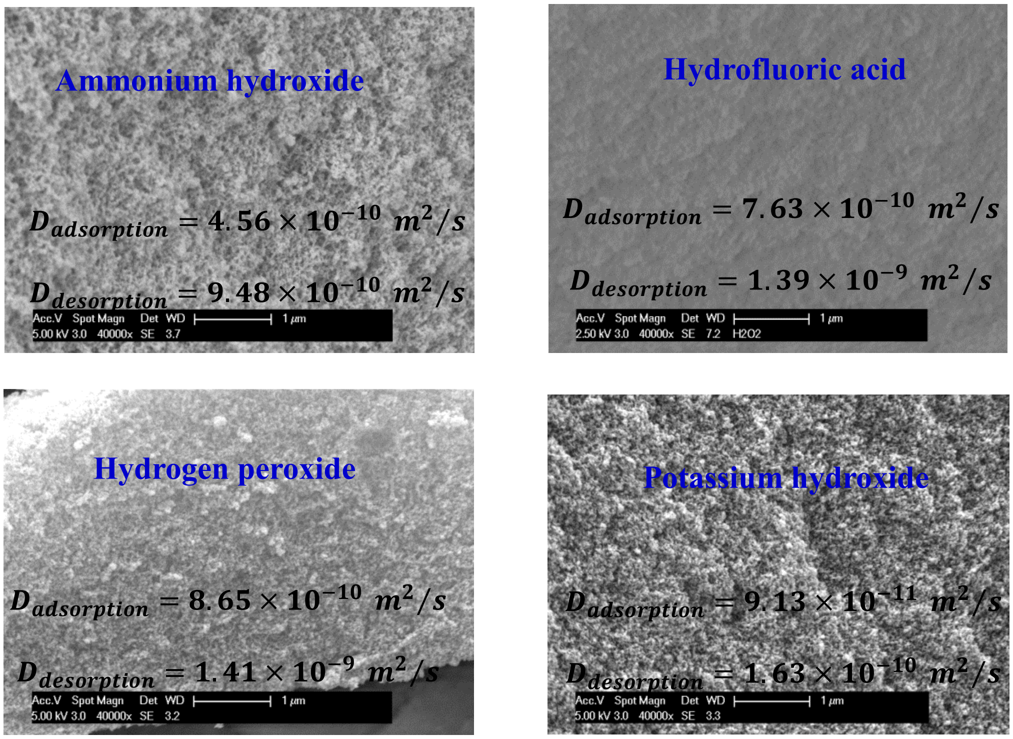

Figure 4.9 Bulk diffusion coefficients for silica aerogel coated metal foam samples prepared by different catalysts.

4.4.3 Effect of relative humidity on mass diffusion coefficient

In order to determine the dependence of the diffusion coefficient on the environmental humidity, and to analyze the variation in an adsorption/desorption cycle, the experimental regimen presented in Figure 8 was undertaken. A dry sample was suddenly exposed to 75% relative humidity. After reaching equilibrium, the sample was dried back to 40% RH for desorption. Then the RH was increased to 65% and after equilibrium was decreased back to 50%. During the next cycle, the RH was increased to 85% and then decreased back to 30% (Figure 4.10). The resulting diffusion coefficients for the aerogel coated metal foam samples prepared using different catalysts are presented in Table 4.2.

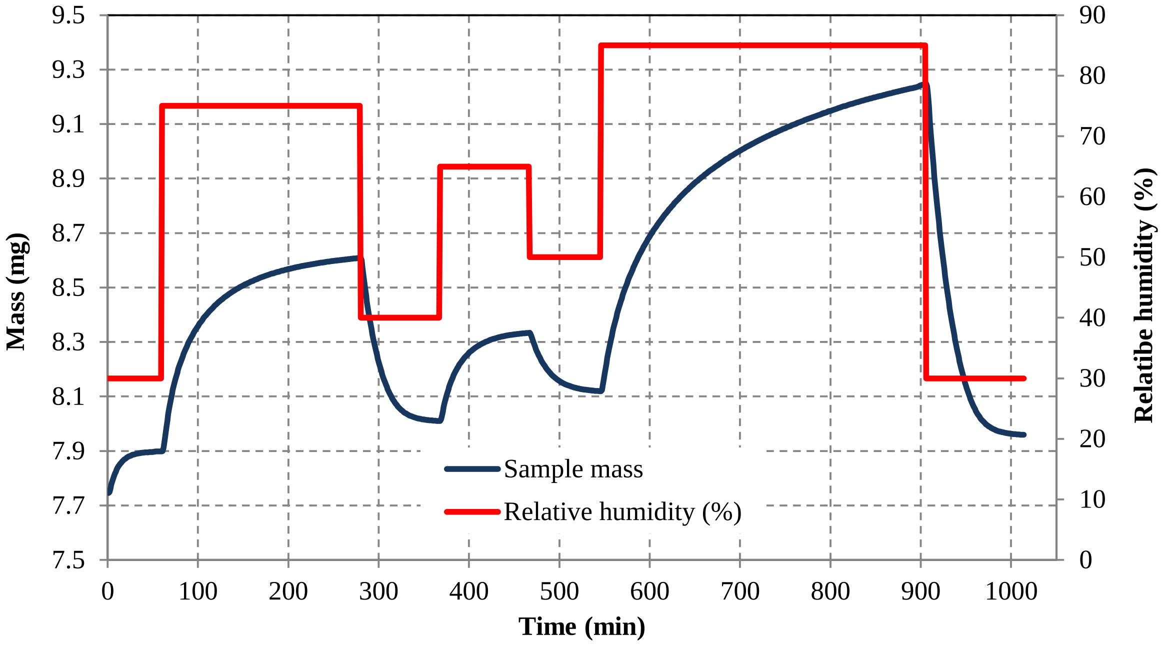

Figure 4.10 Mass variation of the aerogel sample due to step change in humidity for a cyclic adsorption and desorption process (Silica aerogel prepared by hydrofluoric acid coated on 5 PPI metal foam)

Table 4.2 Diffusion coefficients for silica aerogels coated metal foams

Foam type	Type of coating	Effective mass diffusion coefficients				
		30%-75%	75%-40%	40%-65%	65%-50%	50%-85%
5 PPI	NH_4OH	$4.55(10^{-10})m^2/s$	$9.58(10^{-10})m^2/s$	$4.37(10^{-10})m^2/s$	$9.26(10^{-10})m^2/s$	$4.47(10^{-10})m^2/s$
	HF	$8.65(10^{-10})m^2/s$	$1.23(10^{-9})m^2/s$	$8.73(10^{-10})m^2/s$	$1.27(10^{-9})m^2/s$	$8.56(10^{-10})m^2/s$
	H_2O_2	$7.53(10^{-10})m^2/s$	$1.21(10^{-9})m^2/s$	$7.21(10^{-10})m^2/s$	$1.34(10^{-9})m^2/s$	$7.42(10^{-10})m^2/s$
	KOH	$9.11(10^{-11})m^2/s$	$1.59(10^{-10})m^2/s$	$9.17(10^{-11})m^2/s$	$1.44(10^{-10})m^2/s$	$8.87(10^{-11})m^2/s$
10 PPI	NH_4OH	$4.65(10^{-10})m^2/s$	$9.28(10^{-10})m^2/s$	$4.57(10^{-10})m^2/s$	$9.23(10^{-10})m^2/s$	$4.49(10^{-10})m^2/s$
	HF	$8.66(10^{-10})m^2/s$	$1.27(10^{-9})m^2/s$	$8.64(10^{-10})m^2/s$	$1.38(10^{-9})m^2/s$	$8.53(10^{-10})m^2/s$
	H_2O_2	$7.51(10^{-10})m^2/s$	$1.37(10^{-9})m^2/s$	$7.17(10^{-10})m^2/s$	$1.29(10^{-9})m^2/s$	$7.35(10^{-10})m^2/s$
	KOH	$9.16(10^{-11})m^2/s$	$1.71(10^{-10})m^2/s$	$9.28(10^{-11})m^2/s$	$1.54(10^{-10})m^2/s$	$9.07(10^{-11})m^2/s$

20 PPI	NH_4OH	$4.36(10^{-10})m^2/s$	$8.99(10^{-10})m^2/s$	$4.39(10^{-10})m^2/s$	$9.20(10^{-10})m^2/s$	$4.38(10^{-10})m^2/s$
	HF	$8.58(10^{-10})m^2/s$	$1.19(10^{-9})m^2/s$	$8.71(10^{-10})m^2/s$	$1.29(10^{-9})m^2/s$	$8.52(10^{-10})m^2/s$
	H_2O_2	$7.39(10^{-10})m^2/s$	$1.25(10^{-9})m^2/s$	$7.23(10^{-10})m^2/s$	$1.31(10^{-9})m^2/s$	$7.42(10^{-10})m^2/s$
	KOH	$9.12(10^{-11})m^2/s$	$1.67(10^{-10})m^2/s$	$9.12(10^{-11})m^2/s$	$1.53(10^{-10})m^2/s$	$9.13(10^{-11})m^2/s$

It can be observed from Table 4.2 that the mass diffusion coefficient for desorption is higher than the mass diffusion coefficient for adsorption for all three cycles. The values were almost equal for each adsorption and desorption cycle, so it can be concluded that mass diffusion coefficient is independent of the relative humidity to which the sample is exposed.

4.4.4 Effect of substrate's surface area on mass diffusivity

The aerogel-coated metal foams had a thin coating of the silica aerogel on the substrate metal. Mass diffusion coefficients for coated metal foam samples are shown in Figure 4.11 and 4.12 fro adsorption and desorption respectively. The surface areas per unit volume for 5, 10, and 20 PPI foams are $700m^2/m^3$, $1100\ m^2/m^3$ and $1500\ m^2/m^3$ respectively [4.9]. It can be observed that the value for mass diffusion coefficient for adsorption and desorption does not depend on the foam type. Hence the substrate surface area does not affect the diffusion coefficients. By comparing these results to section 3.5.4 of Chapter 3, it can be concluded that the mass diffusion coefficient is a characteristic of the desiccant which does not depends on whether the desiccant is deployed as a solid block or it is spread over a larger surface area of some substrate. The mass diffusion coefficients for aerogel solid blocks and coatings on the metal foams are compared in Figure 4.13. Clearly the difference in the values is negligible for both adsorption and desorption diffusivity. Ancillary experiments performed on silica-aerogel-coated aluminum flat plates also confirmed the conclusion that mass diffusivity of the desiccant does not depend on the substrate surface area. The two samples used for this purpose were coated with silica aerogel prepared using ammonium hydroxide and hydrofluoric acid as catalysts in the sol-gel process. The mass diffusivities for the samples were determined to be 4.36(10^{-10})m^2/s (adsorption) and 9.06(10^{-10})m^2/s (desorption), and 8.66(10^{-10})m^2/s (adsorption) and 1.18(10^{-9})m^2/s (desorption) for ammonium hydroxide and hydrofluoric acid catalysts, respectively.

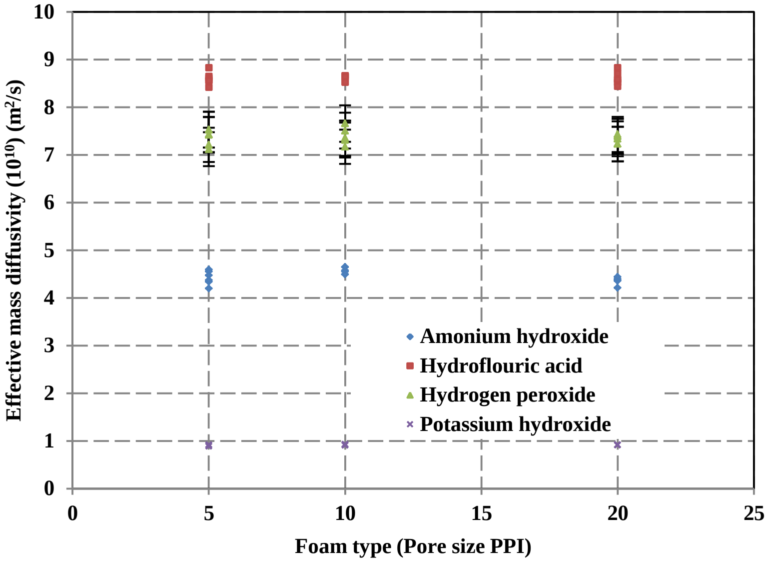

Figure 4.11 Bulk adsorption diffusion coefficients for silica aerogel coated metal foam samples prepared by different catalysts.

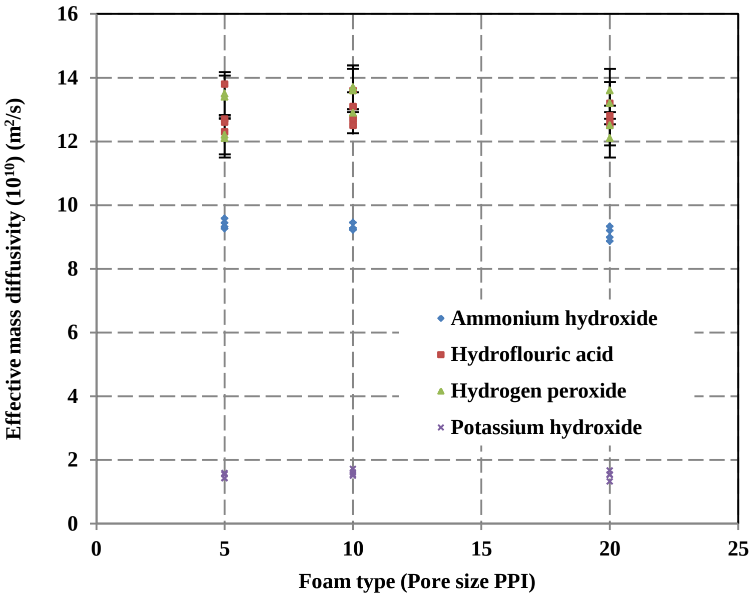

Figure 4.12 Bulk desorption diffusion coefficients for silica aerogel coated metal foam samples prepared by different catalysts.

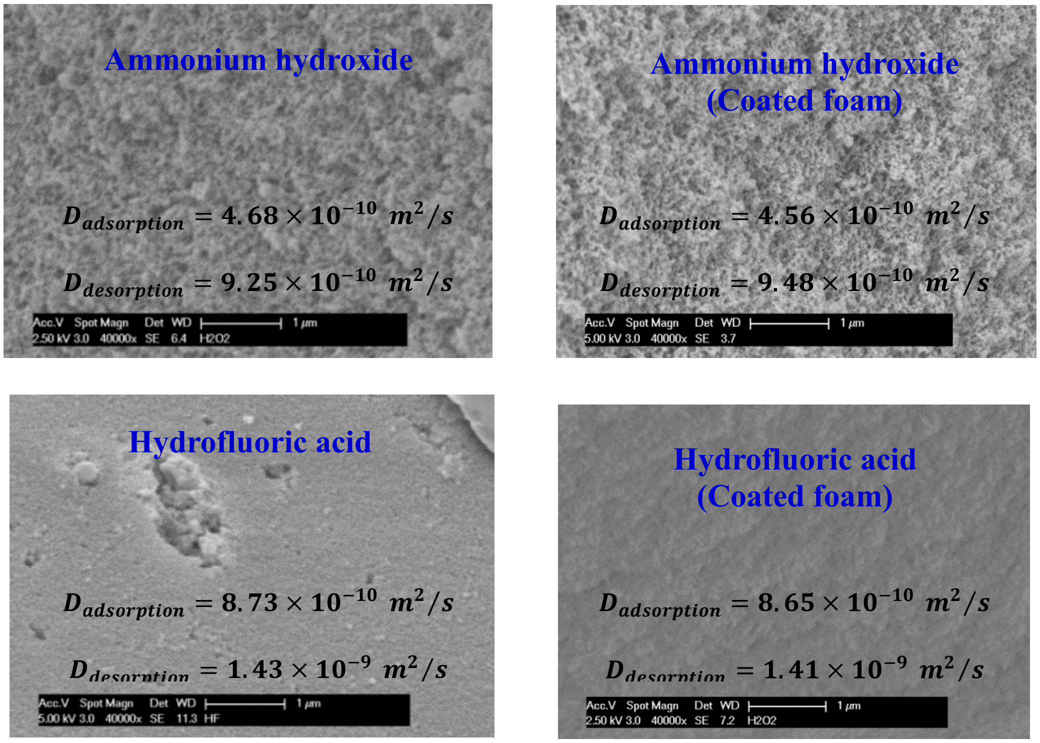

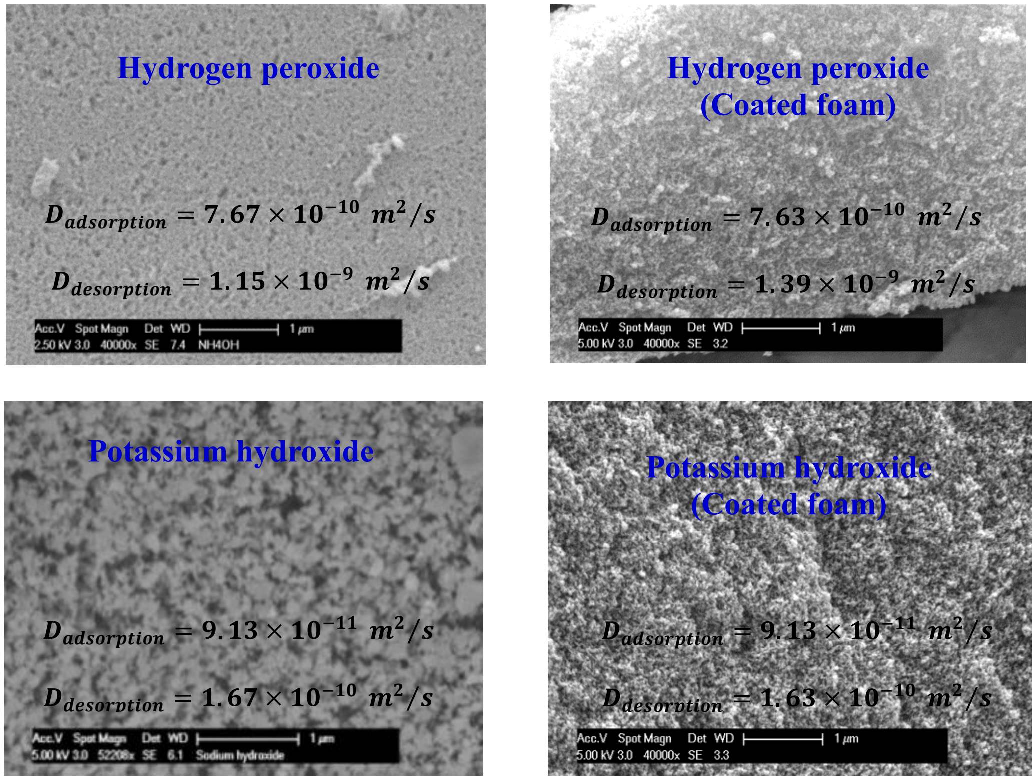

Figure 4.13 Bulk diffusion coefficients for silica aerogel samples prepared by different catalysts (a) solid silica aerogel blocks [Chap. 3] (b) coated silica aerogel on metal foams (5 PPI)

4.5 Adsorption and desorption isotherms of silica aerogel coated metal foams

Moisture adsorption and desorption isotherms of silica aerogels coated foams provide the information about the adsorption capacity of sample. As the adsorption capacity is affected by the desiccant type, silica aerogel coatings prepared using different catalysts in sol-gel process are expected to have different moisture adsorption capacity. The type of substrate is also important parameter as the surface area changes depending on the substrate structure.

4.5.1 Experimental method

The DVS sorption automatic operation (SAO) method was used to set both the desired percent relative humidity steps and the equilibrium criterion (Figure 4.14). A new sample was used for each relative humidity and temperature experimental run.

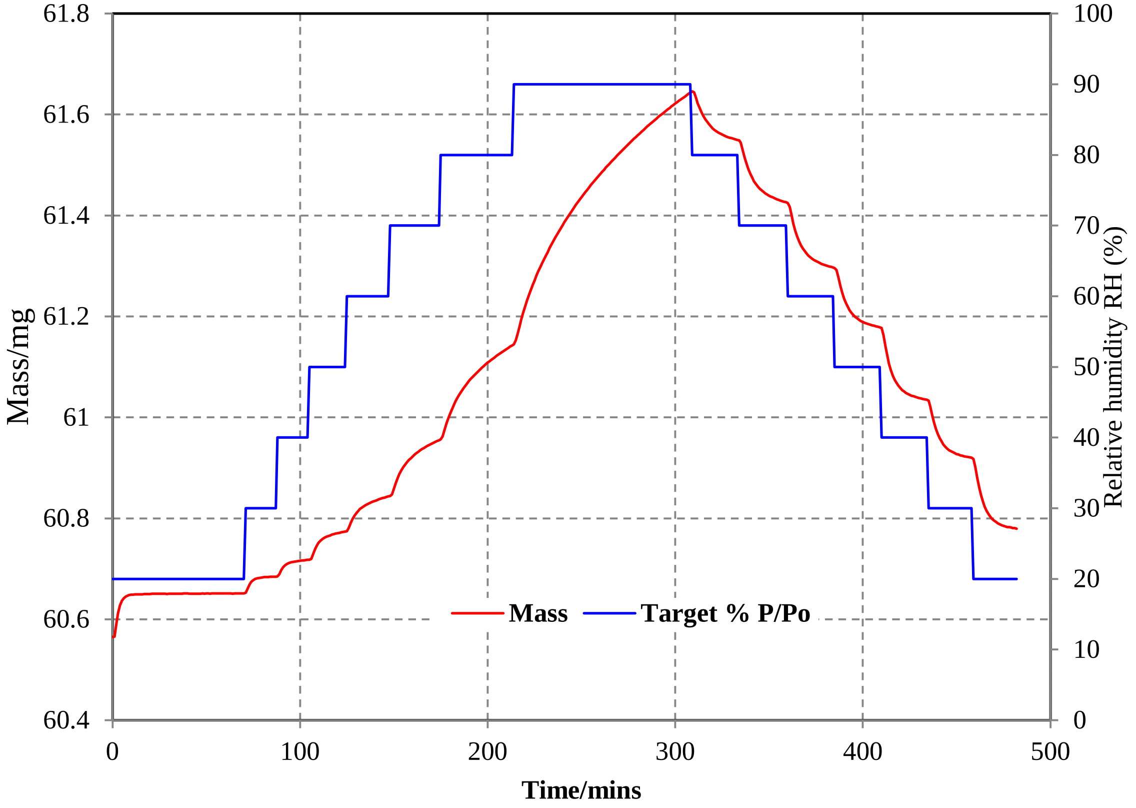

Figure 4.14 Mass change of the sample due to step change in relative humidity

4.5.2 Effect of catalyst used in the sol-gel process on adsorption/desorption isotherms

A representative adsorption/desorption isotherm for silica aerogel coated prepared using hydrofluoric acid as catalyst and coated on 10 PPI aluminum foam is presented in Figure 4.15. It is obvious that the equilibrium isotherm is of type IV, as classified by IUPAC. Like the isotherm for solid silica aerogel block, the adsorption and desorption isotherm do not follow the same path and there is a hysteresis, which exists due to the capillary condensation. The general shape of the isotherm is almost same as isotherm of a solid silica aerogel. However, when the adsorption capacity is compared clearly the coated silica aerogel can absorb almost 20% more moisture at equilibrium. Hence, the substrate affects the adsorption/desorption behavior of desiccant.

Adsorption and desorption isotherms for four different type of silica aerogel coated on 10 PPI metal foam are presented in Figures 4.16 and 4.17. All isotherms are of type IV and the hysteresis exists for all of them. Like the isotherms for solid desiccant, aerogel prepared by hydrofluoric acid and by ammonium hydroxide and coated on the 10 PPI aluminum foam have the maximum moisture retention capacity which can be upto 180% of the mass of the dry sample at 90% relative humidity when the equilibrium is reached. While the silica aerogel prepared by hydrogen peroxide and potassium hydroxide can retain moisture only about 90% of the mass of the dry desiccant under same conditions.

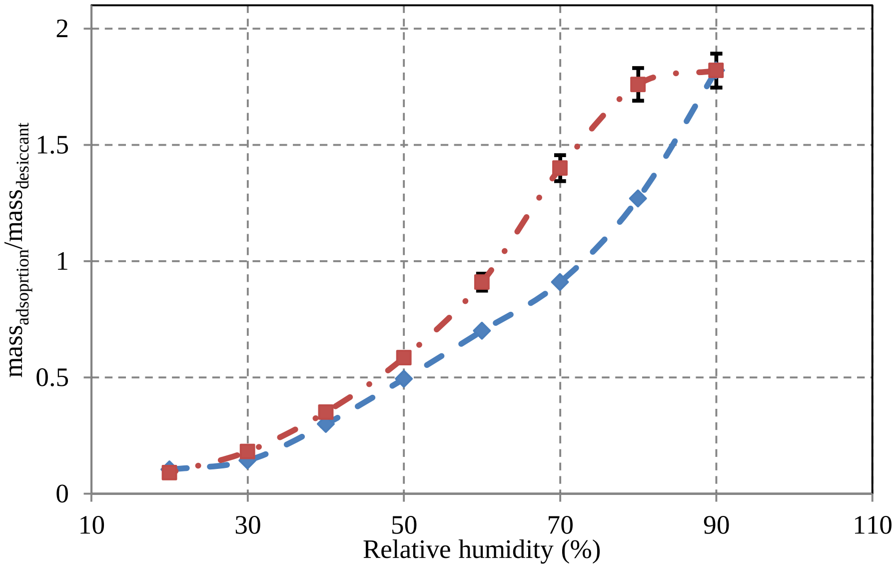

Figure 4.15 Hysteresis in adsorption and desorption isotherms (HF catalyst-10 PPI al foam)

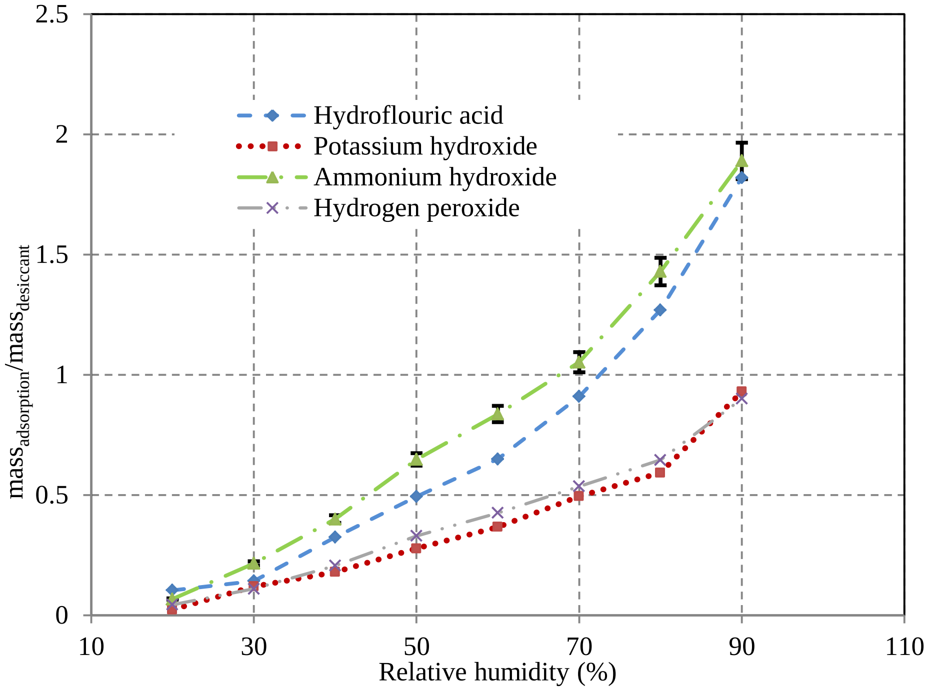

Figure 4.16 Adsorption isotherms of different silica aerogel coating on 10 PPI Al foam

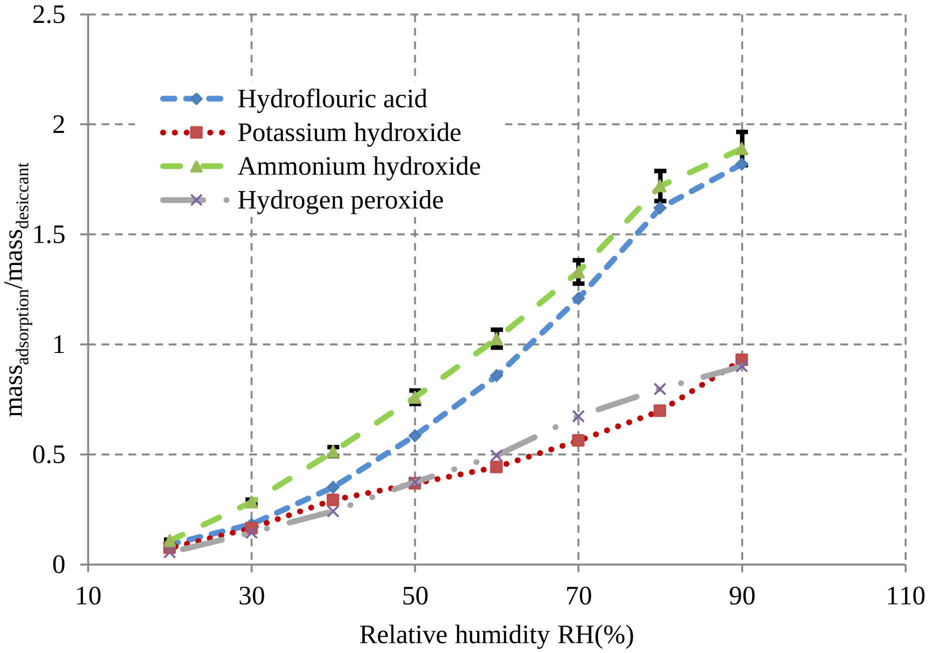

Figure 4.17 Desorption isotherms of different silica aerogel coating on 10 PPI Al foam

4.5.3 Effect of substrate on adsorption/desorption isotherms

Adsorption and desorption isotherms for four different cases (silica aerogel prepared by hydrofluoric acid) are presented in Figures 4.18 and 4.19 respectively. Three different of substrates have been used for comparison and to evaluate the effect of the substrate surface area for coating. As can be observed that unlike the diffusivity (mass diffusion coefficient), the adsorption capacity of the desiccant depends on the type of substrate. As the surface area increases (1200 m^2/m^3 for 10 PPI metal foam, 700 m^2/m^3 for 5 PPI al foam), the adsorption capacity increases. Compared to the solid aerogel block an aerogel coating on the 10 PPI aluminum foam can adsorb about 20% extra moisture for the same dry mass of the desiccant at 90% relative humidity. It is important to note that when the silica aerogel is coated on flat aluminum plate the adsorption capacity increases only about 2%, which is not a very significant increase. However the coating on the metal foams show about 7% and 20% increase for 5 PPI and 10 PPI metal foam respectively.

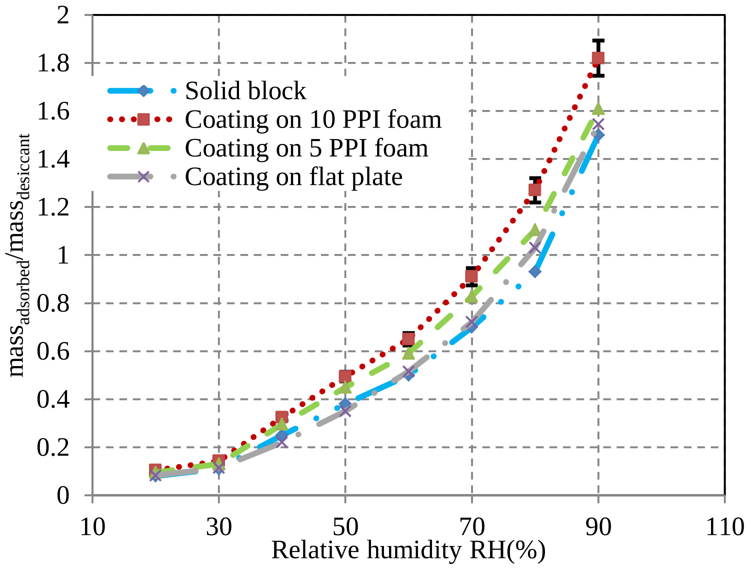

Figure 4.18 Effect of substrate on adsorption isotherms

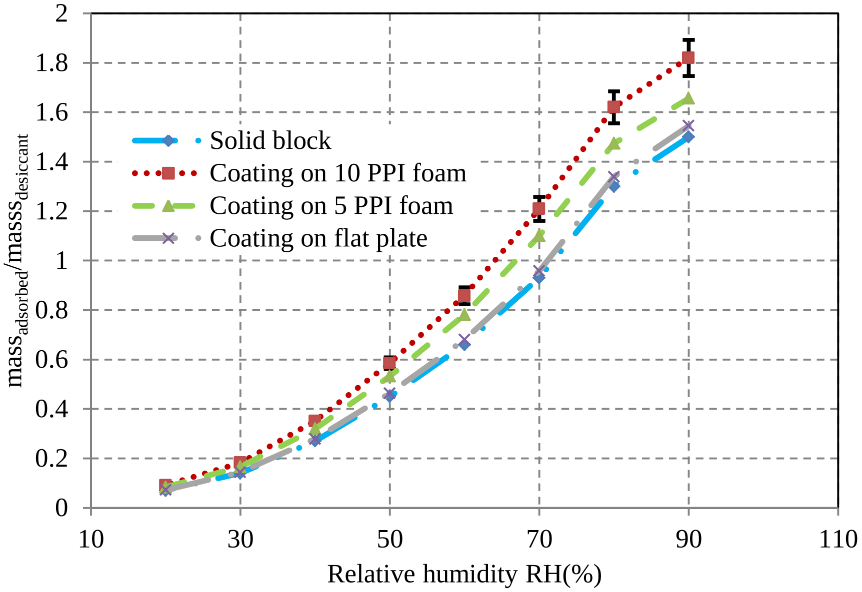

Figure 4.19 Effect of substrate on desorption isotherms

4.6 Conclusions

The sol-gel process was used to prepare a variety of silica-aerogel-coated metal foams. Different types of acidic and basic catalysts were used in the process. The wet samples were dried using the supercritical drying process with CO_2. Scanning Electron Microscopy was performed to analyze the pore structure of different aerogel-coated samples. It was found that the catalyst used in the process significantly affected the microstructure. Bulk diffusion is an important mass transport parameter. The diffusion coefficients were determined using a Dynamic Vapor Sorption instrument, in which an unsaturated or saturated sample was exposed to sudden changes in environmental humidity for adsorption and desorption experiments. A one-dimensional transient diffusion model was used to calculate the diffusivity of the silica aerogel samples from the measured data. The diffusion coefficient depended on coating type, due to different microstructures of the porous desiccants. It was found that silica aerogel coating prepared by hydrofluoric acid catalyst had higher diffusion coefficient by an order of magnitude compared to the aerogel coating prepared using potassium hydroxide. Thus, type of catalyst used in THE sol-gel process can change the mass transfer properties of the resulting aerogels. Samples prepared with basic catalysts (ammonium hydroxide) had more porous microstructure and relatively smaller value for diffusion coefficients, while the samples prepared with acidic catalysts (hydrofluoric acid, hydrogen peroxide) had dense microstructure and relatively larger values for diffusion coefficients. The mass diffusivity was found to be independent of the relative humidity to which the sample was exposed. Experiments on silica aerogel coated metal foam samples prepared using different type of metal foams (with different surface areas and pore sizes) showed that the surface area of the substrate does not affect the mass diffusion coefficients.

Adsorption and desorption isotherms of the coated metal foams samples follow type IV isotherm (IUPAC) with hysteresis due to the capillary condensation. The catalyst used in the coating process has significant affect on the adsorption capacity of the coated sample. The adsorption capacity of silica aerogels when coated on metal foams was found to be almost 20% higher compared to the adsorption capacity of solid desiccant blocks. Hence, the substrate type significantly affects the adsorption capacity of the coating.

4.7 References

[4.1] Y. Aristov, G. Restuccia, G. Cacciola, V.N. Parmon, A family of new working materials for solid sorption air conditioning systems, Applied Thermal Engineering 22 (2002) 191–204.

[4.2] B. Dawoud, Y. Aristov, Experimental study on the kinetics of water vapor sorption on selective water sorbents, Silica gel and alumina under typical operating conditions of sorption heat pumps, International Journal of Heat and Mass Transfer 46 (2003) 273–81.

[4.3] X.J. Zhang, K. Sumathy, Y.J. Dai, R.Z. Wang, Parametric study on the silica gel–calcium chloride composite desiccant rotary wheel employing fractal BET adsorption isotherm, International Journal of Energy Research 29(1) (2005) 37–51.

[4.4] R.W. Besant, C. Simonson, Air-to-air exchangers, ASHRAE Journal 45 (4) (2003) 42–52.

[4.5] K. Nawaz, J. Bock, A.M. Jacobi, Thermal-hydraulic performance of metal foam heat exchangers, International Journal of Heat and Mass Transfer (Under review)

[4.6] Z. Dai, K. Nawaz, Y. Park, C. Qi, A.M. Jacobi, A comparison of metal-foam heat exchangers to compact multi-louver designs for air-side heat transfer applications, Heat Transfer Engineering 33 (2012) 21-30.

[4.7] K. Nawaz, J. Bock, A.M. Jacobi, Experimental studies to evaluate the use of metal foams in highly compact air-cooling heat exchangers, 13th International Refrigeration and Air Conditioning Conference, July 2010, Purdue University Lafayette, IN.

[4.8] K. Nawaz, J. Bock, A.M. Jacobi, Thermal-hydraulic performance of metal foam heat exchangers, 14th International Refrigeration and Air Conditioning Conference, July 2012, Purdue University Lafayette, IN.

[4.9] K. Nawaz, S.J. Schmidt, A.M. Jacobi**,** Aerogel-coated metal foams for dehumidification applications, ASHRAE 2014 Winter Conference January 18-22, 2014, New York, NY USA.

[4.10] C.J. Brinker, A.J. Hurd, P.R. Schunk, G.C. Frye and C.S. Ashley, Review of sol-gel thin film formation, Journal of Non-Crystalline Solids 147 and 148 (1992) 424-436.

[4.11] L.D. Landau and B.G. Levich, Acta Physiochim, U.R.S.S. 17 (1942) 42-54.

[4.12] S.D.R. Wilson, The drag-out problem in film coating theory, Journal of Engineering Mathematics, 16 (1982) 209-221

[4.13] L.E. Scriven, Better Ceramics Through Chemistry III, ed. C.J. Brinker, D.E. Clark and D.R. Ulrich, *Materials Research Society* Symposium *Proceedings*., Vol. 121 (Materials Research Society, Pittsburgh, 1988) 717-729.

[4.14] C. Zhai, Performance Modeling of Desiccant Wheel Design and Operation, PhD Thesis, Carnegie Mellon University 2008.

[4.15] J.W. Jeong, Simplified ceiling radiant cooling panel and enthalpy wheel models for dedicated outdoor air system design, Pennsylvania State University, PhD Thesis 2004.

[4.16] S.J. Slayzak, J.P. Ryan, Desiccant Dehumidification Wheel Test Guide, National Renewable Energy Laboratory 2000.

[4.17] T.S. Ge, Y. Li, R.Z. Wang, Y.J. Dai, A review of the mathematical models for predicting rotary desiccant wheel, Renewable and Sustainable Energy Reviews 12 (2008) 1485–1528.

[4.18] J.W. Jeong, S.A. Mumma, Practical thermal performance correlations for molecular sieve and silica gel loaded enthalpy wheels, Applied Thermal Engineering 25 (2005) 719-740.

[4.19] L.A. Sphaier, L.M. Worek, Analysis of heat and mass transfer in porous sorbents used in rotary regenerators, International Journal of Heat and Mass Transfer 47 (2004) 3415-3430.

[4.20] Nawaz K., Schmidt S.J., and Jacobi A.M. Effect of catalysts used in the sol-gel process on the microstructure and absorption/desorption performance of silica aerogels, ASME 2013 International Mechanical Engineering Congress & Exposition, November 15-21, 2012 -San Diego, CA.

Chapter 5- Heat and mass transfer modeling for desiccant coated substrates

5.1 Introduction

Solid desiccants, such as a molecular sieve, activated carbon, and silica aerogel *etc*, employed for humidity control have microscopic porous structures [5.1, 5.2]. The solid desiccant can be deployed by coating a solid surface (a substrate). The characteristics of the substrate, such as surface area and thermal conductivity affect the moisture removal performance considerably, as well as regeneration. Therefore, an appropriate selection of desiccant and substrate is important to the overall performance of the dehumidifying system.

Metal foam is a candidate substrate for deploying desiccants such as silica aerogels. There has been considerable interest in establishing the thermal-hydraulic performance of metal foams when used as a heat exchanger [5.3-5.7]. The open porosity, low relative density, high thermal conductivity, large surface area per unit volume, and the ability to enhance fluid mixing can make metal foam thermal management devices efficient, compact, and light-weight. Due to their better thermal conductivity they can remove the heat of adsorption and provide heat for regeneration, and hence have potential to make the dehumidification system, more efficient and compact. After determining their thermal-hydraulic performance as heat exchangers, metal foams can be used as substrates for silica aerogel desiccants, and this method of dehumidification is a promising alternative to mechanical vapor-compression systems. The main advantage of desiccant systems is the separate handling of latent and sensible energy loads, thus improving efficiency by up to 50% in air cooling and dehumidification [5.8]. The work reported in this chapter is focused on modeling the dehumidification performance of aerogel-coated metal substrates.

5.2 Literature review

Many mathematical models have been developed to predict the heat and mass transfer behavior in air humidifying/dehumidification applications with solid desiccants. A comprehensive literature review focused on heat and mass transfer modeling in porous media was presented by Ge *et al.* [5.9]. They suggested the existing theoretical models of solid desiccant systems can be broadly classified into two categories, which are based on the inclusion of various resistances considered for building the model. The gas-side resistance model considers the heat and mass transfer resistances only in the bulk gas, while solid-side resistances are ignored. Zhang *et al.* [5.10] developed a one-dimensional coupled heat and mass transfer model to design a honeycomb rotary desiccant wheel. The mathematical model was validated using experimental data. Sharqawaki and Lior [5.11, 5.12] developed a conjugate, transient, three-dimensional heat and mass transfer model for a laminar humid air stream flowing in ducts coated with silica gel; they considered ducts with different cross-sectional geometries: square, circular, and triangular. They modified their earlier numerical model of solid-bed desiccant systems (plates and narrow channels) to include parameters such as permeability and inertia coefficient, which were neglected in their earlier work of heat and mass transfer in porous media.

Among the gas and solid-side resistance models, most of them consider heat conduction and mass diffusion in one dimension only, but a few consider two dimensional transport. Some investigators consider ordinary (Fickian) diffusion, Knudsen diffusion, and surface diffusion on the solid-side, but a few consider only Knudsen and surface diffusions and some consider only surface diffusion. Ruivo *et al.* [5.13, 5.14] assessed the accuracy of different simplifying assumptions commonly adopted in the modeling of the thermodynamic behavior of porous desiccant media. They proposed simplified numerical methods to predict the behavior of hygroscopic rotors, most of them assuming negligible internal resistances to heat and mass transfer and/or constant properties of the desiccant wall. Sphaier and Worek [5.15] developed a dimensionless correlation that accounted for local heat conduction and mass diffusion in solid sorbent materials occurring in either enthalpy exchangers or desiccant wheels. The governing equations were normalized using classical dimensionless groups for heat and mass transfer. Simonson and Besant [5.16] presented a numerical model of coupled heat and moisture transfer during adsorption and desorption processes occurring in enthalpy wheels. The energy transfer associated with phase change can be up to six times the energy transfer due to temperature difference; therefore, the governing energy equations were developed to include the fact that the energy released during the moisture transfer processes can be delivered to air. The model used the heat and mass transfer analogy to determine the heat transfer coefficients. Nóbrega and Brum [5.17] developed a mathematical model for simultaneous heat and mass transfer. The model was solved employing a fully implicit finite volume technique. The different adsorption isotherms were represented by a general equation characterized by a single parameter (the separation factor R, related to the moisture absorbent capacity at different levels of relative humidity), the variation of which allows the behavior of three different desiccant materials (silica-gel, molecular sieve) to be simulated. The results showed that the separation factor R has a significant influence over the dehumidification effectiveness, for given regeneration conditions.

The reliable evaluation of moisture transfer in porous materials is essential in many engineering applications, and the dehumidification process is one of them. One key aspect is a correct description of transport phenomena and the transport potentials. While considerable research has been carried out on the process of moisture transmission through porous materials due to a concentration gradient at isothermal conditions, limited experimental data are available on the influence of temperature gradients on moisture transfer rates. Baker *et al.* [5.18] investigated the significance of non-isothermal effects on the total moisture transfer through porous building materials. The investigation concluded that the vapor pressure gradient is the critical driving potential for moisture transfer, and thermal diffusion is not significant. Janssen [5.19] presented a critical analysis of the investigations supporting the occurrence of thermal diffusion and found that most of the previous studies were flawed. The correct reinterpretation of previous measurements allowed him to conclude that no consistent nor significant thermal diffusion can be observed. This conclusion also agreed with a thermodynamic analysis of the process, which confirmed the existence of thermal diffusion, but also indicated its negligible magnitude [5.19]. In conclusion it can be stated that thermal diffusion is not significant for moisture transfer in desiccant materials for building dehumidification applications, leaving vapor pressure (concentration gradient) as the sole significant transport potential for the diffusion of water vapor in these porous materials.

5.3 Heat and mass transfer modeling

5.3.1 Determination of effective diffusion coefficient

The moisture diffusion coefficients for silica aerogel coated metal foams were determined using the DVS apparatus by exposing unsaturated or saturated samples to environments of differing relative humidity. The details of the process can be found in section 4.3 (Chapter 4).

5.3.2 Determination of friction factor-*f* and Colburn *j*-factor

The pressure gradient and heat transfer rate in metal foams depends on the characteristics of the foams, such as pore and ligament size. Based on experimental results, empirical correlations were developed in section 2.5.3 (Chapter 2) to predict the thermal-hydraulic performance of metal foam heat exchangers. These correlations (equations 2.18 and 2.19) were based on thermal-hydraulic performance of 5, 10, 20 and 40 PPI metal foams. The mass transfer coefficient can be determined using the heat and mass transfer analogy.

$$j_{m,Dp} = \frac{h_m}{V}\left(\frac{D_p}{D_h}\right) Sc^{2/3} = 2Re_{Dh}^{-0.5611}\left(D_p/D_h\right)^{0.3213} \qquad (5.1)$$

Table 5.1 provides surface area per unit volume for different types of foams before and after the coating.

Table 5.1 Surface area per unit volume of coated and uncoated metal foams

Type of Foam (PPI)	Surface Area per unit Volume (m^2/m^3)	
	Uncoated	Coated
5	700	950
10	1000	1350
20	2000	2500
40	2800	3400

5.3.3 Simultaneous heat and mass transfer model (Cartesian coordinates)

In order to determine the dehumidification performance of desiccant coated on foam substrate, a model was developed based on the conservation of energy and species.

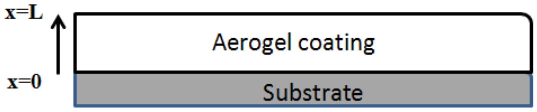

Figure 5.1 Schematic for model development for coating on flat plate

The following equations describe the energy balance with appropriate initial and boundary conditions.

$$\rho c_p \frac{\partial T}{\partial t} = k_{eff} \frac{\partial^2 T}{\partial x^2} + \alpha (C(x,t) - C_\infty) \qquad (5.2a)$$

$$T(x,0) = T_i \qquad (5.2b)$$

$$T(0,t) = T_o \qquad (5.2c)$$

$$k_{eff} \frac{\partial T}{\partial x}(L,t) = -h_T [T(L,t) - T_\infty] \qquad (5.2d)$$

The heat generated due to adsorption is presented by the last term in equation (5.2b). α (W/kmol) is the thermal diffusion coefficient. Equation (5.2c) represents an isothermal surface condition, while equation (5.2d) provides a convection boundary condition at the surface of the coating. Similarly, the following set of equations describe the diffusion of moisture in desiccant coating,

$$\frac{\partial C}{\partial t} = D \frac{\partial^2 C}{\partial x^2} \qquad (5.3a)$$

$$C(x,0) = C_i \qquad (5.3b)$$

$$\frac{\partial C}{\partial x}(0,t) = 0 \qquad (5.3c)$$

$$D_{eff} \frac{\partial C}{\partial x}(L,t) = -h_m [C(L,t) - C_\infty] \qquad (5.3d)$$

In equation (5.3a), thermal-diffusion term (mass diffusion due to temperature difference) has been ignored. The species conservation equation is thus independent of energy equation and can be solved analytically. Equation (5.3c) represents a boundary condition for impermeable surface and equation (5.3d) represents the convection boundary condition at the coating surface.

For the given boundary/initial conditions, moisture concentration in the desiccant coating is given by equation 5.4.

$$C = (C_0 - C_\infty) \sum_{n=0}^{\infty} \frac{4 sin\lambda_n}{2\lambda_n + \sin(2\lambda_n)} \cos\left(\frac{\lambda_n x}{L}\right) e^{-\frac{{\lambda_n}^2 Dt}{L^2}} \qquad (5.4)$$

λ_n are the eigenvalues of the equation (5.5)

$$\lambda_n \tan(\lambda_n) = Bi_m = \frac{h_m L}{D_{eff}} \qquad (5.5)$$

Similarly, the solution for the energy conservation gives the temperature variation in the coating layer,

$$T = T_0 + \left(\frac{(T_\infty - T_o)h_T}{k_{eff} + L h_T}\right) x + \sum_{m=0}^{\infty} \left[\begin{array}{c} f_m(0) + \frac{\alpha L^2}{\rho c_p D_{eff}} (C_0 - C_\infty) \times \\ \sum_{j=0}^{\infty} \left\{ B_j L_{mj} \left(\frac{e^{-\frac{{\lambda_j}^2 Dt}{L^2}} - e^{-\frac{\kappa}{D_{eff}} \frac{{\mu_m}^2 Dt}{L^2}}}{\frac{\kappa}{D_{eff}} {\mu_m}^2 - {\lambda_j}^2} \right) \right\} \end{array} \right] sin(\mu_m {}^{x}/_{L}) \quad (5.6)$$

$$B_j = \frac{4 sin\lambda_j}{2\lambda_j + \sin(2\lambda_j)} \qquad (5.6b) \qquad\qquad L_{mj} = \frac{\int_0^1 \cos\lambda_j \sin(\mu_m \eta)\, d\eta}{\int_0^1 sin^2(\mu_m \eta) d\eta} \qquad (5.6c)$$

$$f_m(0) = \left[\frac{(T_i - T_o)\cos(\mu_m)}{(2\mu_m - \sin(2\mu_m))} + \left(\frac{(T_\infty - T_o)h_T}{k_{eff} + Lh_T}\right)\left(\frac{\sin(\mu_m) - \mu_m\cos(\mu_m)}{(2\mu_m - \sin(2\mu_m))\mu_m{}^2}\right)\right] 4\mu_m e^{-\frac{\kappa \quad \mu_m Dt}{D_{eff} \quad L^2}} \quad (5.7d)$$

μ_m are the eigenvalues calculated based on the Bi_t.

$$-\frac{\mu_m}{\tan(\mu_m)} = Bi_t = \frac{h_t L}{k_{eff}} \qquad (5.8)$$

The saturation time for the desiccant coating can be found using the following correlation.

$$\frac{C}{C_{max}} = 1 - \frac{\sin\xi}{\xi} K e^{-\xi^2 \frac{D_{eff} t}{L^2}} \qquad (5.9)$$

When the Bi_m is large the values of the constants of equation (5.9) are

$$\xi = 1.5708, K = 1.2733$$

It is important to note that due to smaller magnitude of mass diffusion coefficient, the mass transfer Biot number is always higher than 200. However for the cases with relatively smaller mass transfer Biot numbers values of ξ and K can be determined from Appendix H.

5.3.4 Simultaneous heat and mass transfer model (cylindrical coordinates)

In order to more accurately account for the geometry of the foam ligament as substrate for desiccant, a model in cylindrical coordinates was developed (Figure 5.2).

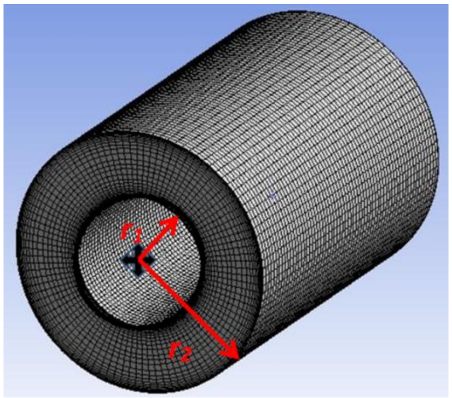

Figure 5.2 Schematic for model development for aerogel coated metal foam

The following equations describe the energy balance with appropriate initial and boundary conditions.

$$\rho c_p \frac{\partial T}{\partial t} = k\left(\frac{1}{r}\frac{\partial}{\partial r}\left(r\frac{\partial T}{\partial r}\right)\right) + \alpha(C(r,t) - C_\infty) \qquad (5.10a)$$

$$T(r_1 \le r \le r_2, 0) = T_i \qquad (5.10b)$$

$$T(r_1, t) = T_o \qquad (5.10c)$$

$$k_{eff}\frac{\partial T}{\partial x}(r_2, t) = -h_t[T(r_2, t) - T_\infty] \qquad (5.10d)$$

Equation (5.10c) represents an isothermal surface condition, while equation (5.10d) provides a convection boundary condition at the surface of the coating. Similarly, the following sets of equations describe the diffusion of moisture in desiccant coating. Similar to the model for rectangular coordinates the thermal-diffusion term has been ignored due to its relatively smaller magnitude

$$\frac{\partial C}{\partial t} = D_{eff}\left(\frac{1}{r}\frac{\partial}{\partial r}\left(r\frac{\partial C}{\partial r}\right)\right) \qquad (5.11a)$$

$$C(r, 0) = C_i \qquad (5.11b)$$

$$\frac{\partial C}{\partial t}(r_1, t) = 0 \tag{5.11c}$$

$$D_{eff}\frac{\partial C}{\partial r}(r_2, t) = -h_m[C(r_2, t) - C_\infty] \tag{5.11d}$$

For the given boundary/initial conditions, moisture concentration in the desiccant coating is given by equation 5.12a.

$$C = (C_0 - C_\infty)\sum_{n=0}^{\infty} C_n\left[Y_0\left(\frac{\lambda_n r}{r_2}\right)J_1\left(\frac{\lambda_n r_1}{r_2}\right) - J_0\left(\frac{\lambda_n r}{r_2}\right)Y_1\left(\frac{\lambda_n r_1}{r_2}\right)\right]e^{-\frac{\lambda_n{}^2 Dt}{r_2{}^2}} + C_\infty \tag{5.12a}$$

Where J_0, Y_0 are the Bessel functions of first and second kind of order zero. λ_n are the eigenvalues satisfying Equation 5.12b.

$$Y_1\left(\frac{\lambda_n r_1}{r_2}\right)[\lambda_n J_1(\lambda_n) - Bi_m J_0(\lambda_n)] = J_1\left(\frac{\lambda_n r_1}{r_2}\right)[\lambda_n Y_1(\lambda_n) - Bi_m Y_0(\lambda_n)] \tag{5.12b}$$

$$C_n = \frac{\int_{\eta_1}^{1} C_0(\lambda_n \eta)d\eta}{\int_{\eta_1}^{1} C_0{}^2(\lambda_n \eta)d\eta} \tag{5.12c}$$

$$C_0(\lambda_n \eta) = Y_0(\lambda_n \eta)J_1(\lambda_n \eta_1) - J_0(\lambda_n \eta)Y_1(\lambda_n \eta_1) \tag{5.12d}$$

Where C_0 is the cylinder function, $\eta = r/r_2$ and $\eta_1 = r_1/r_2$. Similarly the temperature distribution in the coating is given as:

$$T(r,t) = T^*(r,t) + \bar{T}(r) \tag{5.13}$$

$$\bar{T}(r) = T_o + \frac{h_T(T_o - T_\infty)}{\left(\frac{k_{eff}}{r_2} + h_T ln\left(\frac{r_2}{r_1}\right)\right)} ln\left(\frac{r_1}{r}\right) \tag{5.14}$$

$$T^*(r,t)=\sum_{m=0}^{\infty}\sum_{n=0}^{\infty}D_{mn}\left[Y_0\left(\frac{\lambda_n r}{r_2}\right)J_1\left(\frac{\mu_m r_1}{r_2}\right)-J_0\left(\frac{\mu_m r}{r_2}\right)Y_1\left(\frac{\lambda_n r_1}{r_2}\right)\right]\left[Y_0\left(\frac{\mu_m r}{r_2}\right)J_1\left(\frac{\lambda_n r_1}{r_2}\right)\right.$$

$$\left.-J_0\left(\frac{\lambda_n r}{r_2}\right)Y_1\left(\frac{\mu_m r_1}{r_2}\right)\right]e^{-\frac{({\lambda_n}^2-{\mu_m}^2)Dt}{{r_2}^2}} \qquad (5.15a)$$

J_1 and Y_1 are the Bessel function of first and second kind of order one. μ_m are the eigenvalues satisfying the following equation (5.15b)

$$-Y_0\left(\frac{\mu_m r_1}{r_2}\right)[\mu_m J_1(\mu_m)-Bi_T J_0(\mu_m)]=J_0\left(\frac{\mu_m r_1}{r_2}\right)[Bi_T Y_0(\mu_m)-\mu_m Y_1(\mu_m)] \qquad (5.15b)$$

The saturation time for the desiccant coating can be found using the following correlation.

$$\frac{C}{C_{max}}=1-\frac{2K}{\xi}J_1(\xi)e^{-\xi^2\frac{D_{eff}t}{r_2^2}} \qquad (5.16)$$

When the Bi_m is large the values of the constants of equation (5.16) are given as following, (Please consult Appendix H to determine ξ and K when $Bi_m \leq 100$)

$$\xi=2.4050, K=1.6018$$

5.4 Results

5.4.1 Temperature and concentration variation

The heat and mass transfer model was used to predict the temperature and moisture concentration distribution in the desiccant (aerogel) coating. The moisture concentrations at two different times for two thicknesses of desiccant coating are presented in Figure 5.3. For these simulations the characteristics of a 10 PPI metal foam coated with silica aerogel (D_{eff}=4.87 (10^{-10}) m^2/s) were used. The initial desiccant temperature and the substrate surface temperature were assumed to be 273K. The air was assumed to be 298K with 70% relative humidity. The desiccant coating was assumed to be completely dry at the start of process. The heat of adsorption of water vapor in silica aerogel was assumed to be 50kJ/kmol. For smaller thicknesses (0.5 mm) the concentration became uniform after 500s; however, for larger thicknesses the moisture concentration was found to be changing even at 500s. The temperature variation is presented in Figure 5.4, which continues to change due to the heat of adsorption till the concentration becomes uniform in the coating.

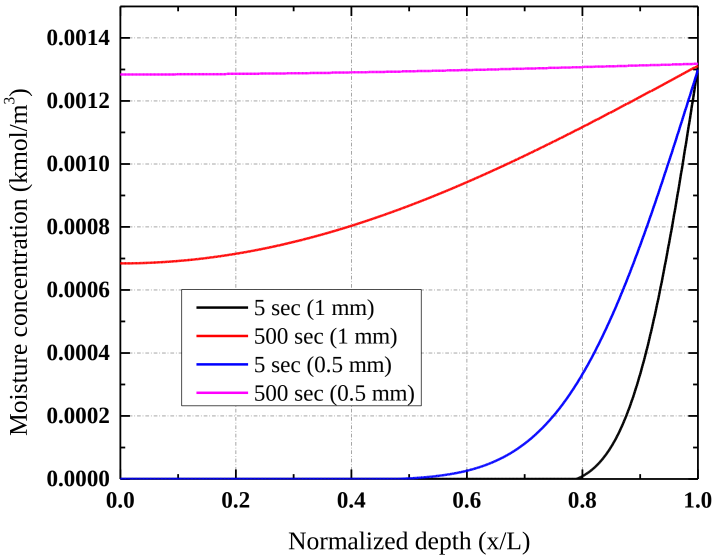

Figure 5.3 Concentration distributions in the desiccant coating

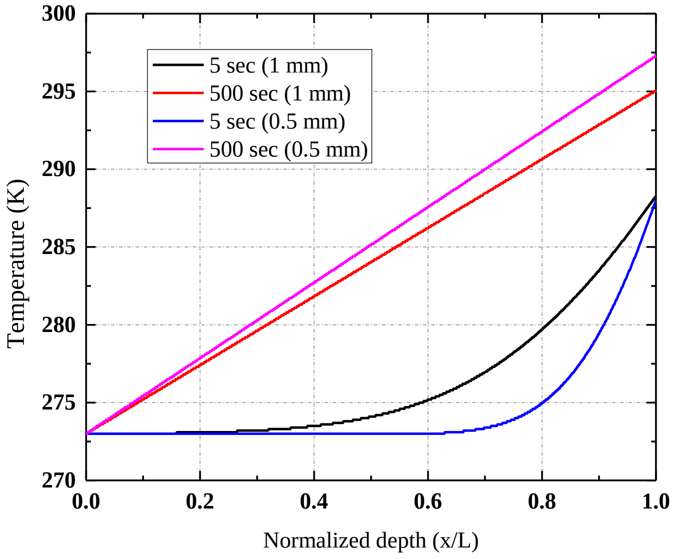

Figure 5.4 Temperature distributions in the desiccant coating

5.4.2 Thermal-hydraulic and mass transfer performance of coated metal foams

It is important to evaluate the transport parameters such as the convective coefficients for the coated substrate system, as they determine the heat and moisture removal rate. The heat transfer coefficients (equation 2.19) for aerogel coated metal foams samples for varying face velocity are shown in Figures 5.5. When the desiccant coated on the metal foam with smaller pore size, the resulting heat transfer coefficient is higher as a better mixing occurs in foam with smaller pore size (larger PPI). Similarly, based on heat and mass analogy, the mass transfer coefficient (equation 5.1) for the coated foams with smaller pore size have higher mass transfer coefficients as presented in Figure 5.6. However, the foam with smaller pore size have larger pressure gradient (Figure 5.7) and require more fan power (pressure gradients determined by equation 2.18). It is important to note that at larger face velocities (more than 4m/s), the increase in the pressure gradient for all foam type is relatively larger compared to the corresponding increments in the heat and mass transfer coefficients.

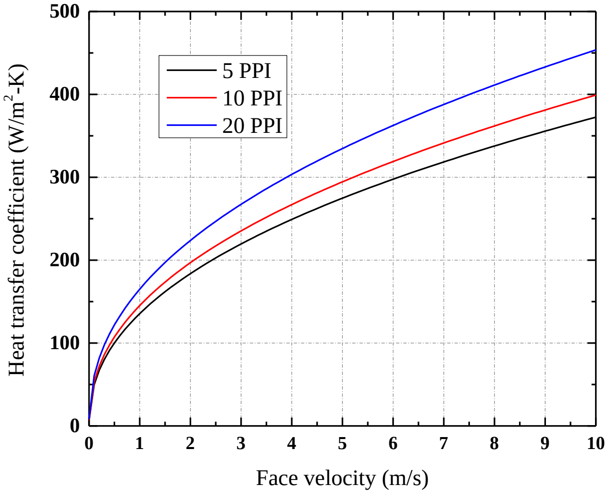

Figure 5.5 Dependence of heat transfer coefficients on foam type

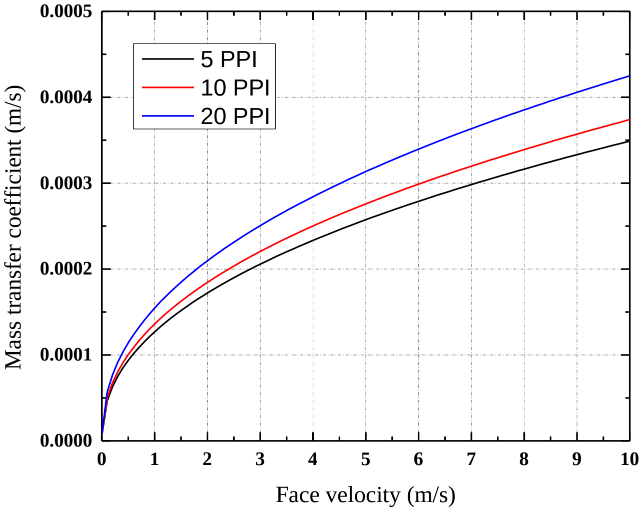

Figure 5.6 Dependence of mass transfer on foam type

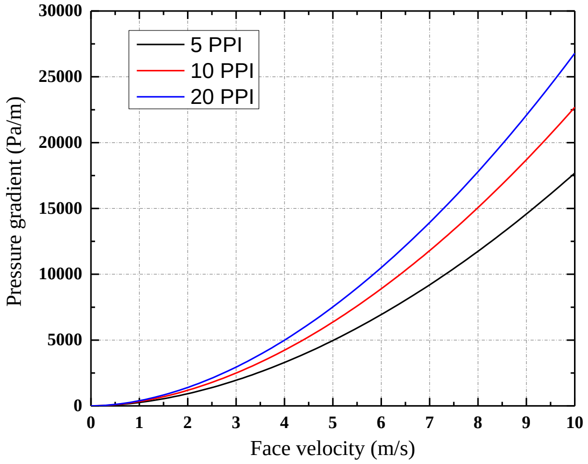

Figure 5.7 Dependence of pressure gradient on foam type

5.4.3 Saturation time for the coating

The saturation times (the time required to reach a certain percent of equilibrium moisture adsorbed, equation 5.9) for different types of desiccants coated on the metal foam are presented in Figure 5.8. For Sample 1, the coating on the 10 PPI metal foam was manufactured using hydrofluoric acid as the catalyst in the Sol-Gel process, while for sample 2, the coating was prepared using ammonium hydroxide as the catalyst. As shown in Figure 5.8, both diffusivity and the coating thickness affect the saturation time. The experimentally determined desorption diffusion coefficients for both samples were almost twice the value of the adsorption diffusion coefficients (Chapter 4). Thus, the time required for desorption could be smaller compared to the time required for adsorption process if the processes take place at the same regeneration temperature.

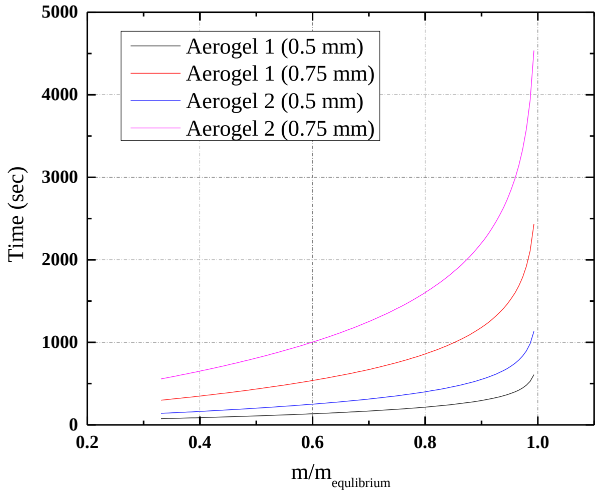

Figure 5.8 Moisture saturation time for different aerogel types

5.4.4 Comparison of different substrates

Substrate characteristics have a significant effect on the moisture adsorption rate and capacity of dehumidification system. Mass transfer coefficients for metal foam substrates were determined by heat and mass transfer analogy. Using the same technique, the mass transfer characteristics of some other substrate candidate geometries have been analyzed and compared to the metal foams for moisture removal rate. In particular, the convective resistance to mass transport was determined by equation (5.17).

$$\frac{\dot{m}}{\Delta\rho} = A_{substrate} h_m \tag{5.17}$$

$A_{substrate}$ (m^2/m^3) is substrate surface area, $\Delta\rho$(kg/m^3) is the driving potential and $\dot{m}$ (kg/s) is the moisture removal rate. For comparison, two plain-fin-round-tube and one louvered-fin heat exchanger have been considered. The plain-fin-round-tube heat exchanger along with the dimensions is presented in Figure 5.9. Both samples had the same geometry (face area, flow depth etc.) but had different fin spacing (Fin pitch-2mm *vs.* 5 mm). The third sample was a louver-fin heat exchanger (Park and Jacobi [5.25] - Chapter 2).

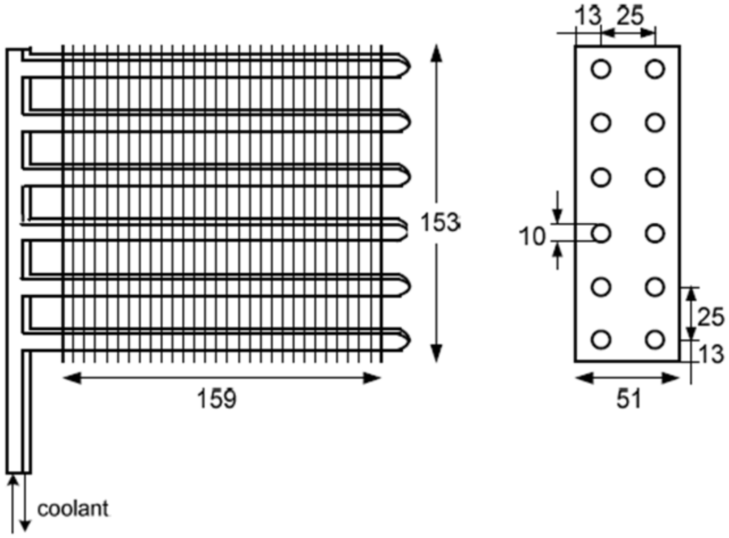

Figure 5.9 Plain fins round tube mass exchanger [5.23]

The surface areas for the samples were 188 m^2/m^3, 500 m^2/m^3, 850 m^2/m^3, 700 m^2/m^3, 1200 m^2/m^3 and 2000 m^2/m^3 for plain fin sample 1, plain fin sample 2, louver fin, 5 PPI metal foam, 10 PPI metal foam and 20 PPI metal foam, respectively. The moist inlet air (25^oC dry bulb temperature, 75% RH) was assumed to be dried to comfortable moisture level (25^oC dry bulb temperatures, 40% RH). The moisture removal rates due to mass convection through different mass exchangers are presented in Figure 5.10, and the fan power required to accomplish the process is shown in Figure 5.11

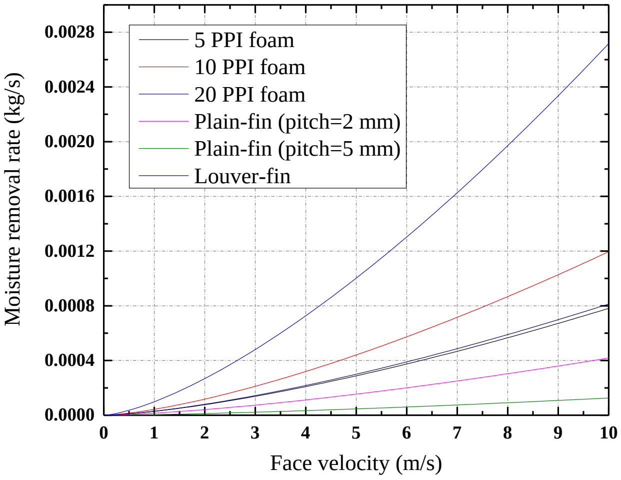

Figure 5.10 Comparison of moisture removal rate for different mass transfer exchangers

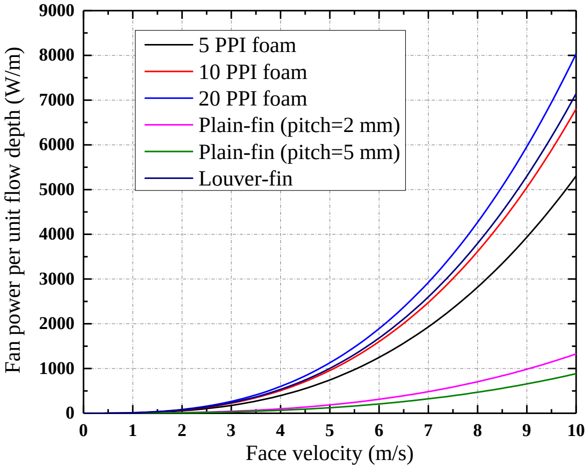

Figure 5.11 Comparison of fan power requirement for different mass transfer exchangers

Among different substrate candidates, metal foams with 10 and 20 PPI foams resulted in the largest moisture removal rate per unit volume of dehumidification device when all the results were normalized to the same driving potential ($\Delta\rho$, defined as $\Delta\rho = \rho_{inlet} - \rho_{exit}$). This happens due to two factors, first metal foams with 10 and 20 PPI foam has quite large surface area to volume ratio, second the mass transfer coefficients are also larger than for the other geometries.

However the fan power required to achieve the moisture removal rate is high as well (Figure 5.11). The performance of louver-fin mass exchanger is similar to the 5 PPI metal foams. However, for the plain fin mass exchanger, the mass transfer rate is quite low compared to louvered-fin or metal foam mass exchangers.

In Chapter 4 adsorption/desorption isotherm were presented for coated substrates. These properties affect the adsorption capacity of the dehumidifying device. For comparison, 5 substrates candidates have been considered: two plain fin heat exchangers, a louver fin heat exchanger, and 5 and 10 PPI metal foams. All samples were assumed to have a uniform coating of 0.05 mm desiccant. The adsorption capacities of resulting systems are presented in Figure 5.12.

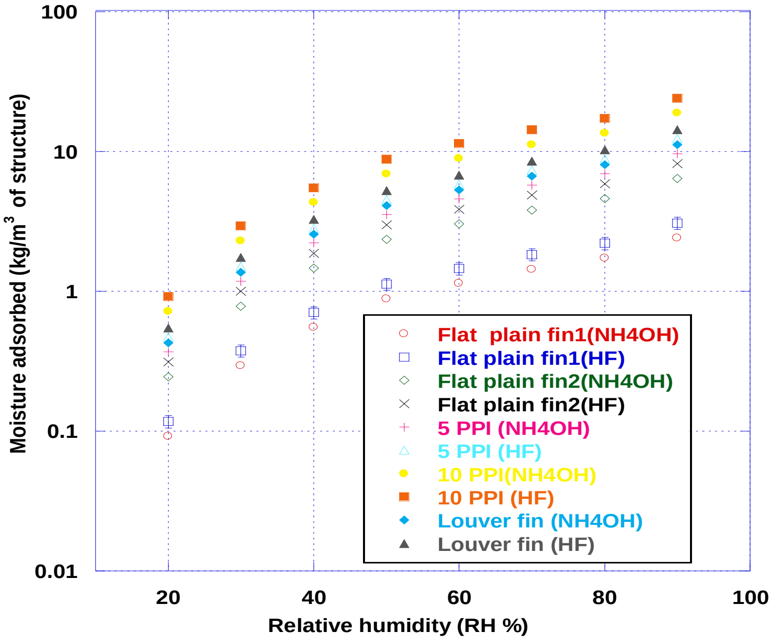

Figure 5.12 Comparison of moisture adsorption capacity for different mass transfer exchangers

Two desiccant types have been used in the analysis. It is obvious that metal foam substrates coated with the silica aerogel have the largest adsorption capacity per unit volume among all candidates considered. A 20 PPI metal foam mass exchanger can adsorb 10 times more than can a flat plain-fin type heat exchangers due to larger surface area and better adsorption capacity as presented in chapter 4 (adsorption isotherm for metal foam vs. for the flat plate). The power required for the regeneration process are presented in Figure 5.13 considering that the regeneration energy of 4500 kJ/kg is provide during a desorption time of ten minutes. It can be seen that when metal foams are deployed as substrates, the energy for regeneration is substantial, because the desiccant holds more water. Regeneration sources other than low-temperature waste heat may need to be considered so that regeneration times can be held short.

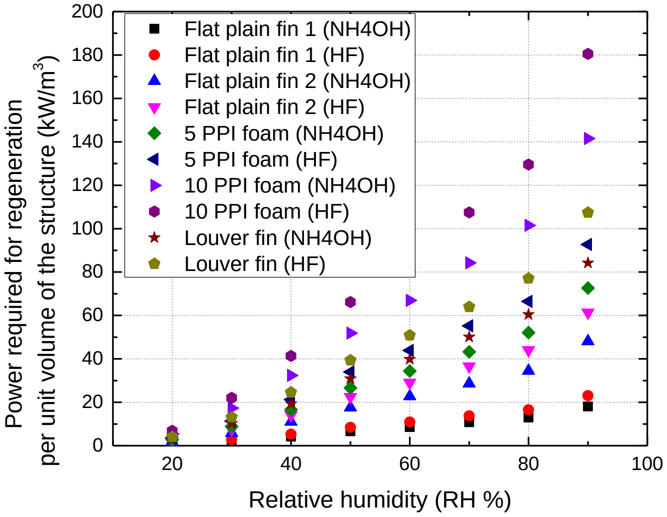

Figure 5.13 Comparison of moisture regeneration power required for different mass transfer exchangers

5.5 Conclusions

A mathematical model was developed to predict the performance of aerogel-coated metal foams. The effect of thermal-diffusion was neglected. The coupled heat and mass conservation equations were solved and the results were used to predict the variation of temperature and concentration in the coated desiccants on the metal foam surface. Due to better thermal diffusivity, the temperature profile should become steady in less time than that required for the concentration profile to become steady however this did not happen due to the heat of adsorption which generates continuously till the concentration become uniform in the coating. Based on experimental data for bare metal foams (Chapter 2), the dehumidification performance of aerogel coated metal foams was predicted. The effect of the type of foam was investigated on the heat and mass transfer coefficients and the pressure gradient. It was found that metal foams with smaller pore sizes when coated with desiccant, provide higher heat and mass transfer coefficients, but the pressure drop per unit length was higher as well. The model was used to determine the saturation time for different desiccant types and coating thicknesses. Samples with larger coating thicknesses and small diffusivity took longer to saturate with moisture. It was found that metal foams when coated with silica aerogel desiccants have higher adsorption capacities and moisture removal rates per unit volume for the same thickness of the coating. However due to larger adsorption capacity, the conventional use of low-grade heat might need to be reconsidered.

5.6 References

[5.1] U.S. Department of Energy 2008. Energy efficiency trends in residential and commercial buildings, Energy Efficiency and Renewable Energy.

[5.2] ASHRAE 2009. ASHRAE Handbook-Fundamentals. Atlanta: American Society of Heating Refrigeration and Air Conditioning Engineers, Inc.

[5.3] X. Han, Q. Wang, Y. Park , C. T'Joen, A. Sommers, A.M. Jacobi, A review of metal foam and metal matrix composites for heat exchangers and heat sinks: Review, Heat Transfer Engineering 133 (2012) 991-1009.

[5.4] Z. Dai, K. Nawaz, Y. Park, C. Qi, A.M. Jacobi, A comparison of metal-foam heat exchangers to compact multi-louver designs for air-side heat transfer applications, Heat Transfer Engineering 33 (2012) 21-30.

[5.5] K. Nawaz, J. Bock, A.M. Jacobi, Thermal-hydraulic performance of metal foam heat exchangers, International Journal of Heat and Mass Transfer (Under review)

[5.6] K. Nawaz, J. Bock, A.M. Jacobi, Experimental studies to evaluate the use of metal foams in highly compact air-cooling heat exchangers, 13th International Refrigeration and Air Conditioning Conference, July 2010, Purdue University Lafayette, IN.

[5.7] K. Nawaz K., J. Bock, A.M. Jacobi, Thermal-Hydraulic Performance of Metal Foam Heat Exchangers, 14th International Refrigeration and Air Conditioning Conference, July 2012, Purdue University Lafayette, IN.

[5.8] P. Mazzei, F. Minichiello, D. Palma, HVAC dehumidification systems for thermal comfort: A critical review, Applied Thermal Engineering 25 (2005) 677–707.

[5.9] T.S. Ge, Y. Li, R.Z. Wang, Y.J. Dai, A review of the mathematical models for predicting rotary desiccant wheel, Renewable and Sustainable Energy Reviews 12 (2008)1485-1528.

[5.10] X.J. Zhang, Y.J. Dai, R.Z. Zhang R.Z., A simulation study of heat and mass transfer in a honeycombed rotary desiccant dehumidifier, Applied Thermal Engineering 23 (2003) 989-1003.

[5.11] H.S. Al-Sharqawi, N. Lior, Effect of flow-duct geometry on solid desiccant dehumidification, Industrial and Engineering Chemistry Research 47 (2008) 1569-1585.

[5.12] H.S. Al-Sharqawi, N. Lior, Transient two-dimensional dehumidification and desorption behavior of plate desiccants under humid air flow: a conjugate model that includes diffusion and adsorption/desorption within the desiccant, Industrial and Engineering Chemistry Research 50 (2011) 8859–8880.

[5.13] C.R. Ruivo, J.J. Costa, A.R. Figueiredo, Numerical study of the cyclic behavior of a desiccant layer of hygroscopic rotor, Numerical Heat Transfer 48 (2008) 1037-1053.

[5.14] C.R. Ruivo, J.J. Costa, A.R. Figueiredo, On the behavior of hygroscopic wheels: part 1: Channel modeling, International Journal of Heat and Mass Transfer 50 (2007) 4812-4822.

[5.15] L.A. Sphaier, L.M. Worek, Analysis of heat and mass transfer in porous sorbents used in rotary regenerators, International Journal of Heat and Mass Transfer 47 (2004) 3415-3430.

[5.16] C.J. Simonson, R.W. Besant, Heat and moisture transfer in desiccant coated rotary energy exchangers: part I – numerical model, International Journal of HVAC&R Research 3 (1997) 325-350.

[5.17] C.E. Nóbrega, N.C.L., Modeling and simulation of conjugated heat and mass transfer in desiccant materials, 5th European Thermal-Sciences Conference, The Netherlands, 2008.

[5.18] P.H. Baker, G.H. Galbraith, R.C. McLean, Temperature gradient effects on moisture transport in porous building materials, Building Service Engineering Research and Technology 30 (2009) 37-48.

[5.19] H. Janssen, Thermal diffusion of water vapor in porous materials: Fact or fiction? International Communication in Heat and Mass Transfer 54 (2011) 1548-1562.

[5.20] Kays W.M., London A.L., Compact heat exchangers, 2nd edition, 1964, McGraw-Hill, New York.

[5.21] K. Nawaz, S.J. Schmidt, A.M. Jacobi, Effect of catalysts used in the Sol-Gel process on the microstructure and absorption/desorption performance of silica aerogels, ASME 2013 International Mechanical Engineering Congress & Exposition, November 15-21, 2012-San Diego, CA.

[5.22] K. Nawaz, S.J. Schmidt, A.M. Jacobi, Effect of catalysts used in the Sol-Gel process on the absorption/desorption performance of silica aerogel coated metal foams, International Journal of Heat and Mass Transfer (Under review)

[5.23] L. Liu, Effect of air-side surface wettability on the performance of dehumidifying heat exchangers, PhD thesis, University of Illinois at Urbana Champaign, Urbana, IL 2011.

Chapter 6- Conclusions

6.1 Summary of the research

A new method to control the indoor humidity has been suggested. The deployment of silica aerogel on metal foam as substrates is a novel way to build an efficient dehumidifying system. The system makes independent control of sensible and latent loads possible and is better than conventional SSLC systems, such as enthalpy wheels, due to its flexibility of operation. The use of metal foams as substrate provides better thermal conductivity and higher surface area to volume ratio, enhancing the performance of the dehumidifying device by removing the heat of adsorption from the desiccant coating. The substrate can also conduct heat during the regeneration process, enhancing the desorption cycle.

6.1.1 Thermal-hydraulic performance of metal foam

Wind tunnel experiments have been conducted to determine the thermal-hydraulic performance of metal-foam heat exchangers. The face velocity, metal foam pore size and base material, and heat exchanger geometry affect the thermal-hydraulic performance. It was found that at face velocities above 3m/s the relative increment in the pressure gradient is higher than is the increase in the heat transfer rate. A 40PPI metal foam with the pore size of about 1.5mm provides better flow mixing which results in higher heat transfer coefficient compared to the heat transfer coefficients manifested by 5PPI metal foam (pore size=4mm) for the same flow conditions. However the pressure gradient for metal foam with a smaller pore size (larger PPI) is higher than for the one with larger pore size (Smaller PPI). One way to mitigate the pressure drop is to modify the geometry of the metal foam heat exchangers in a way that does not seriously compromise the heat transfer performance. The heat transfer coefficients for copper foam are higher than for the aluminum foam. Although the pressure drop is considerably higher, the overall thermal hydraulic performance of metal foam heat exchangers can surpass that of existing designs such as louvered fins. There are correlations available in the literature to predict the pressure drop and heat transfer coefficient of metal foams, but they are based on non-realistic geometries, and they cannot predict the performance accurately. On the basis of the data presented in this thesis, and an analysis of the relevant length scales, curve fits for the friction factor f and Colburn j factor based on pore diameter were developed. The new correlations provide predictions with reasonable engineering accuracy over a broader parametric range than did the previously available correlations.

6.1.2 Adsorption/desorption characteristics of silica aerogels

Many types of silica aerogel samples were prepared using the sol-gel process by using different catalysts during synthesis. The solvent (methanol) in the wet samples was removed using a supercritical drying process with carbon dioxide. A study of the microstructure of the resulting samples showed that the catalyst used in the process significantly affects the micro pore size (pore size can vary from ~30nm to 150nm). The basic catalysts (NH_4OH, KOH, *etc.*) resulted in a less porous structure, while the acidic catalysts (HF, steric acid, *etc.*) showed a structure with a higher pore density. Adsorption and desorption characteristics of the micro porous media depended on the microstructure. The diffusion coefficients were determined using a Dynamic Vapor Sorption instrument, in which the dry or wet samples were exposed to sudden changes in the humidity of the surrounding air. It was found that some silica aerogels prepared by particular catalysts have relatively higher diffusion coefficients compared to others. Samples prepared with basic catalysts had relatively smaller value for diffusion coefficients, while the samples prepared with acidic catalysts had larger values for diffusion coefficients. The mass diffusivity of silica aerogels depended on the process direction. The mass diffusion coefficient for desorption was almost twice that for adsorption, which indicates that the moisture desorption process can be performed at faster rate compared to adsorption. Mass diffusion coefficients were found to be independent of the environment humidity. Over the relatively small temperature variation (15^oC-35^oC) of this study, temperature had no significant impact on the mass diffusivity of silica aerogels. The equilibrium isotherms indicated that the adsorption capacity of the silica aerogels also depends on the microstructure of the porous media, which is affected by the catalysts used in the sol-gel process. The silica aerogel prepared by hydrofluoric showed capacities of about 150% the dry mass of the desiccant at about 90% RH while the adsorption capacity of the silica aerogel prepared by potassium hydroxide was 80% of the dry mass of desiccant at the same equilibrium conditions (RH=90%, Temperature= 25^oC) . Adsorption/desorption isotherms for all samples were of type IV (IUPAC) and showed hysteresis, which resulted due to capillary condensation. The largest hysteresis was observed for the sample prepared using hydrofluoric acid, which is the aerogel with better adsorption capacity (larger surface area and high pore density).

6.1.3 Adsorption/desorption characteristics of silica aerogels coated metal foams

The performance of a solid desiccant can be affected by the characteristics of the substrate material. Silica aerogel coated metal foams were prepared using the sol-gel process. Different types of acidic and basic catalysts and metal foams were used in the in a dip coating process of samples. The values of diffusion coefficient ware determined using a Dynamic Vapor Sorption instrument, where an unsaturated or saturated sample was exposed to sudden change in environmental humidity for adsorption and desorption experiments, respectively. The diffusion coefficient depended on the coating type, due to different microstructure of the porous desiccant. The mass diffusivity was found to be independent of the relative humidity to which the sample was exposed. Experiments on silica aerogel coated metal foam samples prepared using different types of metal foams (with different surface areas and pore sizes) showed that the surface area of the substrate does not affect the mass diffusion coefficients as the values were comparable to the diffusion coefficients for the silica aerogel solid blocks prepared using the same catalyst in the sol-gel process. Adsorption and desorption isotherms of the coated metal foams samples follow type IV isotherm (IUPAC) with hysteresis due to capillary condensation. It was found that both the catalyst used in the synthesis and the substrate type affected the adsorption capacity of silica aerogels. Silica aerogel coated on metal foam showed an increase of 20% when compared to the adsorption capacity of solid desiccant blocks. Hence, the substrate type significantly affects the adsorption capacity of the coating.

6.1.4 Simultaneous heat and mass transfer

A model of simultaneous heat and mass transfer was developed to predict the performance of desiccant-coated substrates. Thermal-diffusion in the mass conservation equation was neglected. The coupled heat and mass conservation equations were solved and the results were used to predict the variation of temperature and concentration in the coated desiccants on the metal foam surface. The better thermal diffusivity compared to the mass diffusivity indicated that the temperature profile should become steady in shorter time compared to the time required to achieve the uniform moisture concentration in coating, however it did not happens due to the generation of heat of adsorption during. The dehumidification and thermal-hydraulic performance of aerogel coated metal foams was predicted using the heat and mass transfer analogy and using the correlations for friction factor *f* and Coburn *j* factor for bare metal foam (developed in Chapter 2). The effect of the type of foam was investigated on the heat and mass transfer coefficients and the pressure gradient. It was found that metal foams with smaller pore sizes when coated with desiccant, provide higher heat and mass transfer coefficients, but the pressure drop per unit length was high as well. The model was used to determine the saturation time for different desiccant types and coating thicknesses. The time required for a 0.5 mm thick silica aerogel coating prepared using hydrofluoric acid on a 5 PPI metal foam for 90% moisture saturation was about 40 minutes; however, the desorption time was estimated to be about 12 minutes due to the relatively large diffusion coefficient under desorption conditions.

6.2 Future work

Metal foams have large surface-area-to-volume ratios and complex cell structures which enhance the heat transfer performance, but the pressure drop and hence the required fan power is high. The geometry of the heat exchanger can be modified to mitigate the pressure drop. The thermal-hydraulic performance of metal foam heat exchangers under dry conditions showed promising performance. However, it would be interesting to determine the performance is affected under wet and frosted conditions.

Different types of silica aerogels were prepared by changing the catalyst. Some of them are superior to others, due to better adsorption/desorption performance. The performance might be enhanced by using them in mixtures with other desiccants. The resulting desiccants should be designed to have better adhesive characteristics and improved longevity.

Another important aspect is the performance comparison to the excising dehumidifation systems such (as enthalpy wheels) to quantify the benefits in terms of the energy usage to achieve the desired dehumidification performance.

Appendix A-Metal foam heat exchangers

(Sample manufacturing)

Metal foam heat exchanger were build in different confrigurations. These heat exchangers were tested in a closed loop-wind tunnels for the thermal-hydraulic performacne analysis. The design of samples along with the detailed specifications are described in this section.

Figure A.1 Metal foam heat exchanger-flat tube configuration

Table A.1 Design specifications (Flat tube configuration)

Sample	1-3
Base metal	Al 6061 alloy
Porosity	10 PP
Tube side configuration	Flat tube
Number of fins	10
Fin depth	15 mm
Fin thickness	15 mm
Bonding method	Artic silver, thermal compound
Face area	200 mm×174 mm
Tube width	25.4 mm
Tube wall thickness	0.5 mm

Figure A.2 Metal foam heat exchanger-Round copper tube annular configuration

Table A.2 Design specification (Round copper tube annular configuration)

Sample	8
Porosity	10 PPI
Base metal	Copper alloy
Tube side configuration	Round tube
Bonding method	brazed
Face area	200 mm×150 mm
Tube diameter	10 mm
Tube thickness	0.5 mm
Fin thickness	10 mm
Number of tubes passes	10

Figure A.3 Metal foam heat exchanger-Round aluminum tube annular configuration

Table A.3 Design specification (Round aluminum tube annular configuration)

Sample	9
Porosity	10 PPI
Base metal	Aluminum
Tube side configuration	Round tube
Bonding method	brazed
Face area	200 mm×150 mm
Tube diameter	10 mm
Tube thickness	0.5 mm
Fin thickness	10 mm
Number of tubes passes	10

Figure A.4 Metal foam heat exchanger-Round aluminum tube continuous block configuration

Table A.4 Design specification (Round aluminum tube continuous block configuration)

Sample	10
Porosity	10 PPI
Base metal	Aluminum
Tube side configuration	Round tube
Bonding method	brazed
Face area	200 mm×150 mm (continuous block)
Tube diameter	10 mm
Tube thickness	0.5 mm
Number of tubes passes	10

Appendix B- Thermal-hydraulic performance of metal foams under wet conditions

B.1 Introduction

In many applications, air-cooling heat exchangers operate with the heat-transfer surface below the dew point of the air, in order to dehumidify the conditioned air. Condensate accumulates on the surface and is retained by surface tension unless removed by gravitational or air-flow forces. Retained condensate profoundly affects the heat transfer and pressure drop performance and plays an important role in the overall performance of the air-conditioning system. It also has implications on air quality: condensate blown off the heat exchanger surface can directly affect occupant comfort, and water provides a medium for biological activity on air-handling surfaces. With growing concerns about the quality of conditioned air, designers often strive for heat exchanger designs that provide efficient condensate drainage in off-cycle operation.

B.2 Data reduction methods

To determine the wet and dry air-side heat transfer coefficients for the heat exchanger, the following data reduction procedure was used.

$$Q_{air} = \dot{m}_{air} c_{pair} \left(T_{airdown} - T_{airup} \right) + \dot{m}_{condensate} h_{fg} \tag{B.1}$$

$$Q_{cool} = \dot{m}_{cool} c_{pcool} \left(T_{coolin} - T_{coolout} \right) \tag{B.2}$$

For a metal foam heat exchanger of the wet condition, LMED is used to calculate the heat transfer coefficient [B.1].

$$q = HA\Delta h_{LM} \tag{B.3}$$

$$\Delta h_{LM} = F\frac{\left(h_{air,in} - h_{coolant,out}\right) - \left(h_{air,out} - h_{coolant,in}\right)}{ln\left(\frac{h_{air,in} - h_{coolant,out}}{h_{air,out} - h_{coolant,in}}\right)} \qquad (B.4)$$

$$\frac{1}{HA} = \frac{1}{\left(\eta_o hA/C_p\right)_{air}} + \frac{1}{(hA/b)_{coolant}} + bD_h R_{bond} \qquad (B.5)$$

$$\eta_o = 1 - \frac{A_{foam}\left(1 - \eta_f\right)}{A_{foam} + \varepsilon A_{foam}} \qquad (B.6)$$

$$\eta_f = \frac{tanh\left(m_{foam} L_f\right)}{m_{foam} L_f} \qquad (B.7)$$

$$m_{foam} = \sqrt{\frac{3\pi D_f}{D_p^2 k_{eff}} . \frac{C_{p,air}}{b}} \qquad (B.8)$$

Where q is the heat transfer rate (Q_{cool} minimum uncertainty), Δh_{LM} is the log-mean enthalpy difference, HA is the overall heat transfer coefficient based upon the enthalpy difference, C_{pa} the air side sensible heat transfer coefficient, D_h is the hydraulic diameter of the tube, R_{bond} is the contact resistance and b is slope of saturated enthalpy line for air evaluated at average tube internal surface temperature.

$$b = \left(\frac{\partial h_{air,s}}{\partial T}\right)_{T_w} \qquad (B.9)$$

B.3 Results

Results for experiments conducted under wet conditions are presented in Figure B.1a. As with dry surfaces, the pressure gradient increases when the face velocity increases. Porosity plays an important role, as it does under dry conditions. Foam with 40 PPI showed higher pressure drop compared to a 10 PPI metal foam sample. An interesting feature, which was considerably different from the results for tests under dry-surface conditions, is that whereas under dry conditions the pressure gradient increases in a quadratic manner with velocity, for wet conditions the pressure gradient increased almost linearly with velocity. The relative differences for different foams under wet conditions were smaller than those observed for dry conditions. Due to condensation, both latent and sensible heat transfer are involved. The resulting air-side heat transfer coefficients when the metal foam heat exchangers were tested conducted under wet conditions are presented in Figure B.1b. As in the dry-surface case, the foam with smaller pores (larger PPI) showed a heat transfer rate higher than the foam with larger pores. As the face velocity increased the heat transfer coefficient also increased. The rate of increase with face velocity for specific type of foam heat exchanger was relatively higher compared to the increase under dry conditions.

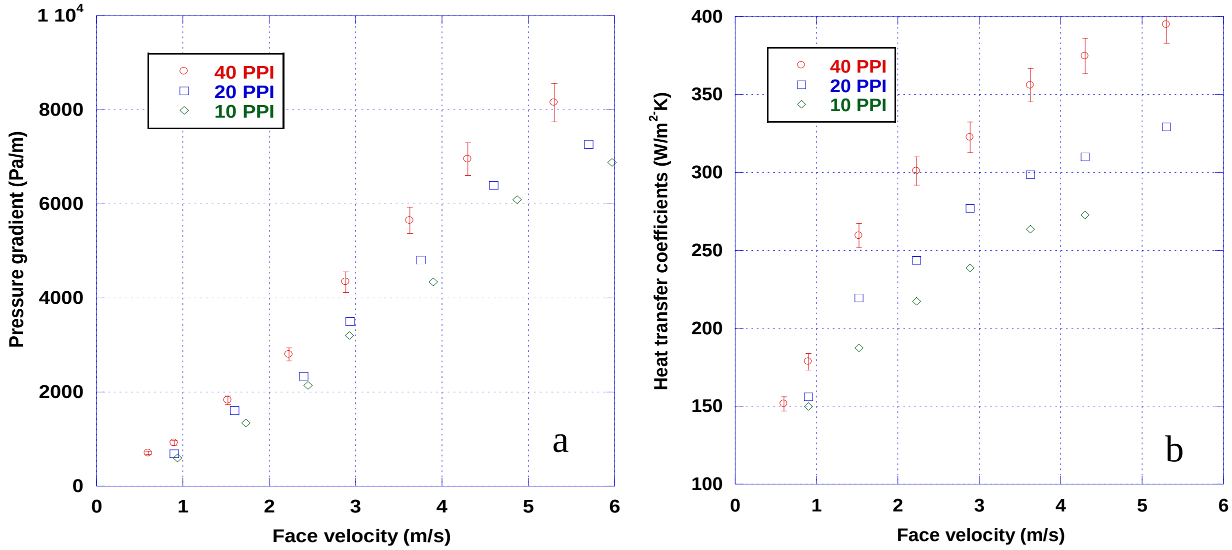

Figure B.1 Hydraulic performance (a), thermal performance (b) under wet conditions

An important feature was observed when the pressure gradient results for dry and wet conditions were compared to each other (10 PPI foam), as shown in Figure B.2 (for representative data). Surprisingly, the pressure drop is only slightly larger under wet conditions when compared to dry conditions. These experiments were conducted under condensing conditions, using the same sample used for dry conditions. Many compact configurations for heat exchangers manifest a significant increase in pressure gradient under wet-surface conditions, because accumulated condensate blocks the air flow passages. However, that does not occur for these metal foams, making them promising for use under wet-surface conditions. This behavior is due to the good condensate removal ability of metal foams, which was also observed when dynamic-dip tests were performed to compare the drainage behavior to that of louver-fins

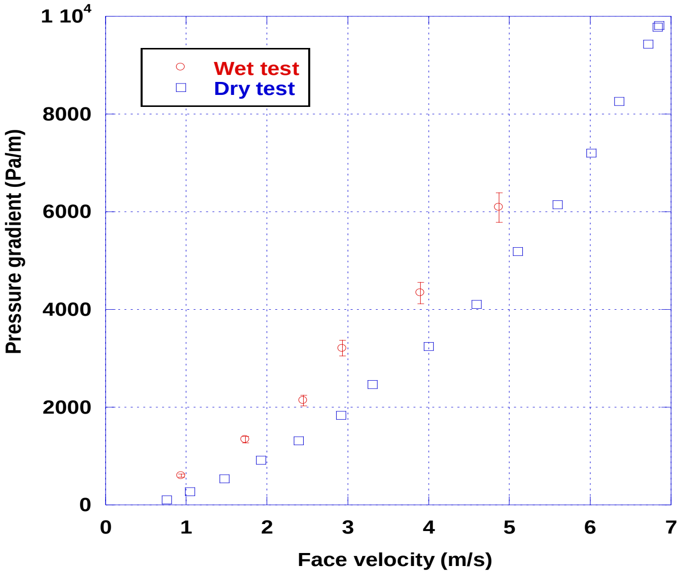

Figure B.2 Comparison of pressure gradients under dry and wet tests

B.4 Reference

[B.1]. L. Xia, M.Y. Chan, S.M. Deng, X.G. Xu, A modified logarithmic mean enthalpy difference (LMED) method for evaluating the total heat transfer rate of a wet cooling coil under both unit and non-unit Lewis Factors, International Journal of Thermal Sciences 48 (2009) 2159–2164.

Appendix C-Frost formation on metal foams

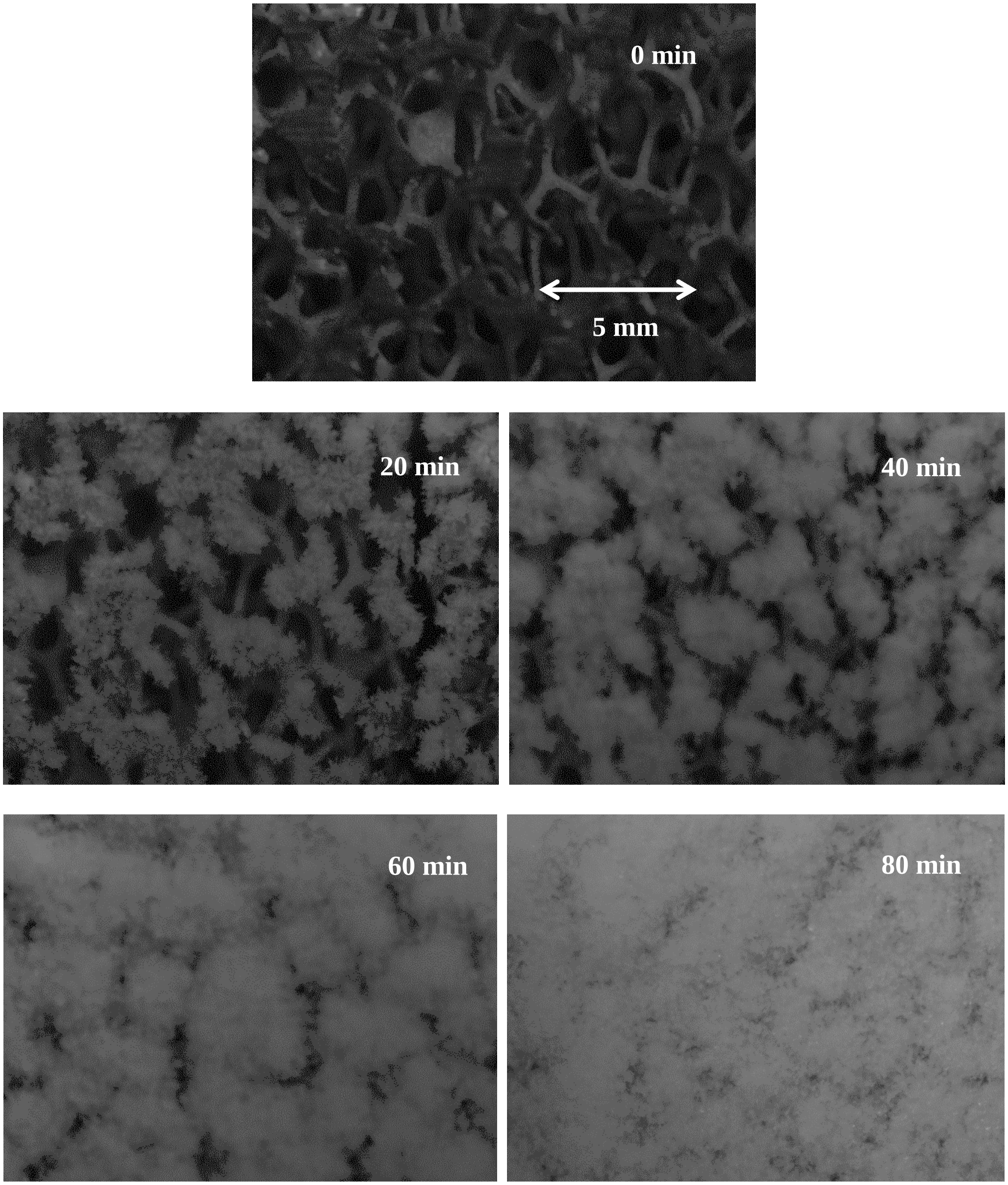

Figure C.1 Frost growth on 10 PPI copper foam

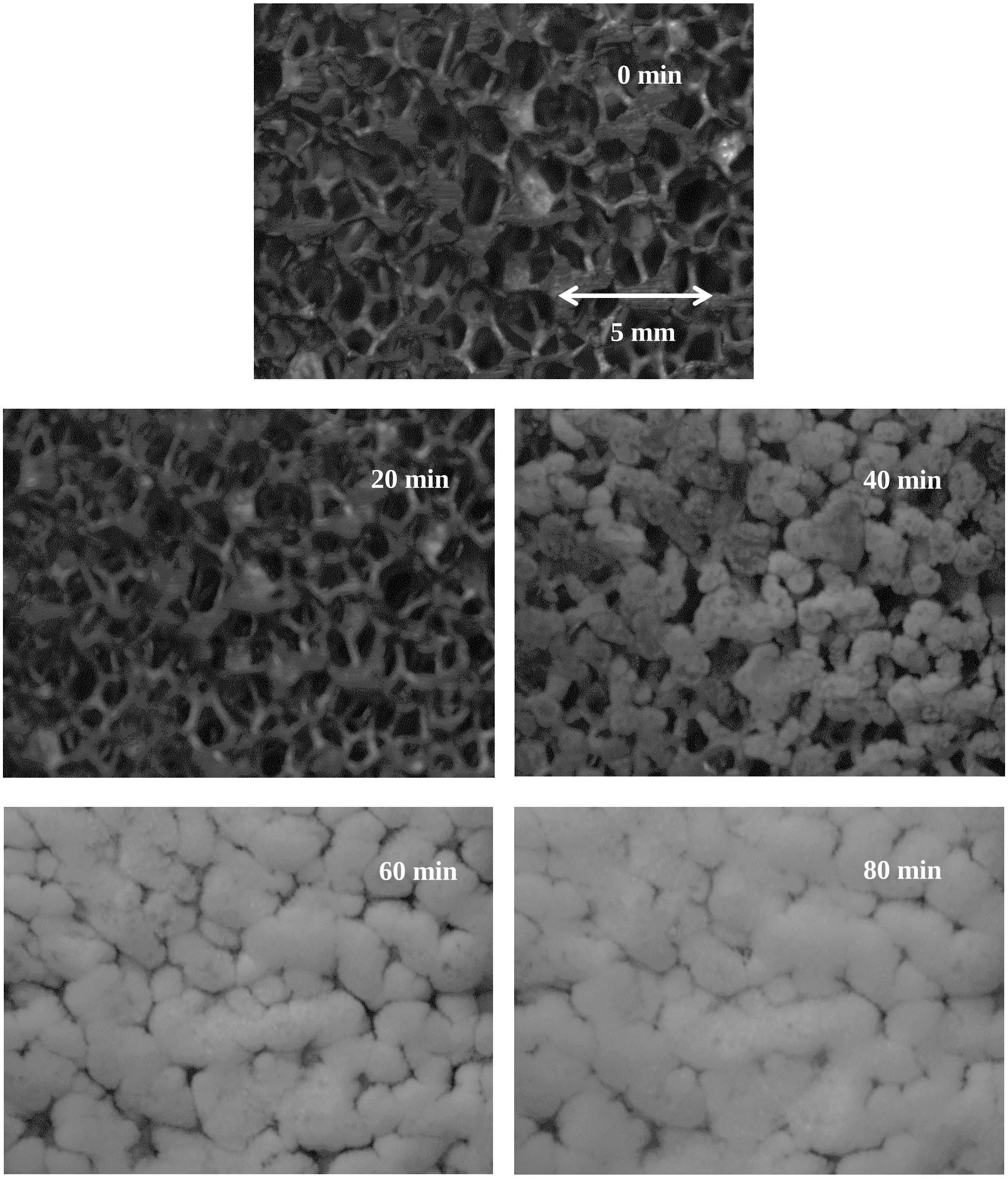

Figure C.2 Frost growth on 20 PPI copper foam

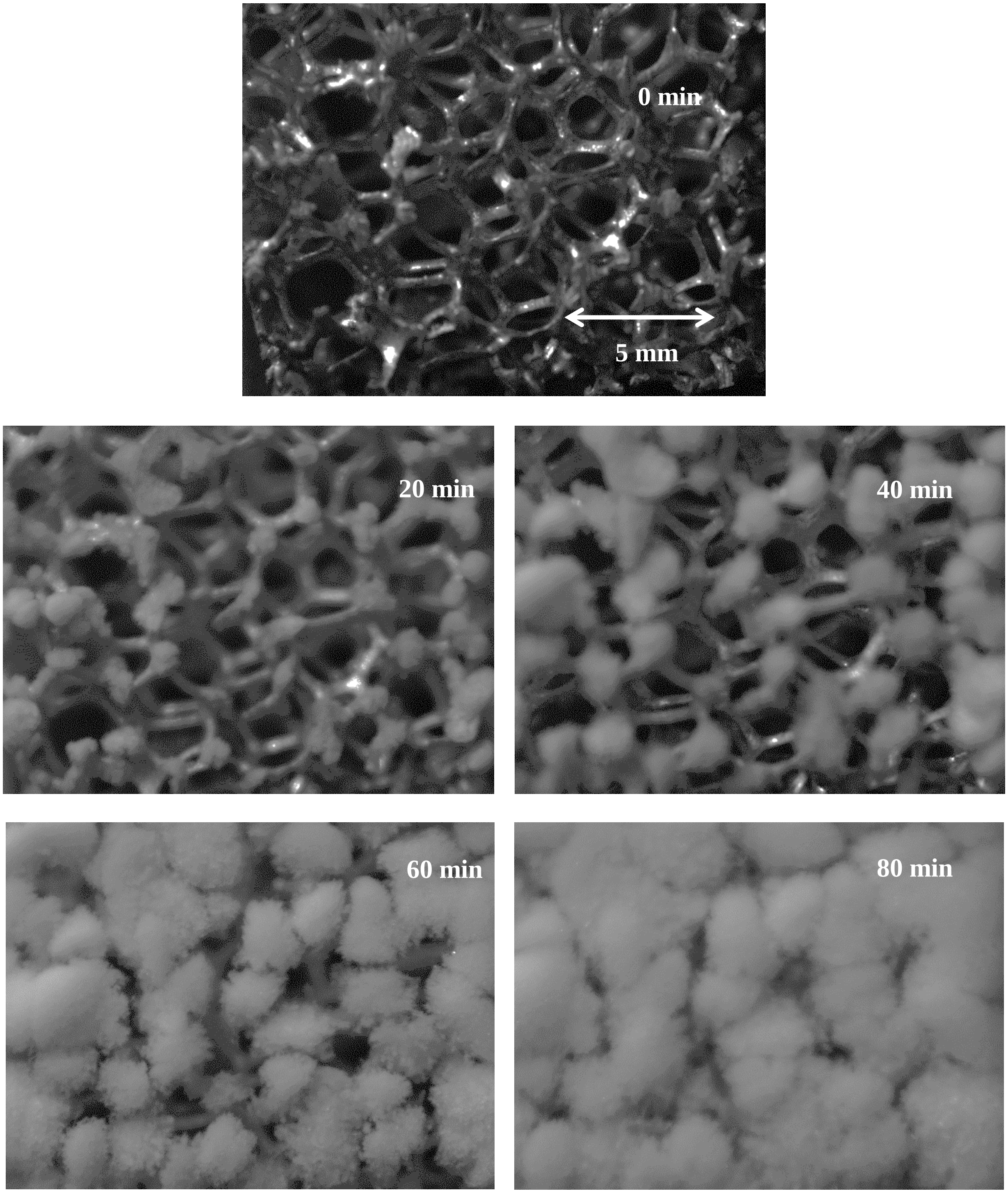

Figure C.3 Frost growth on 10 PPI aluminum foam

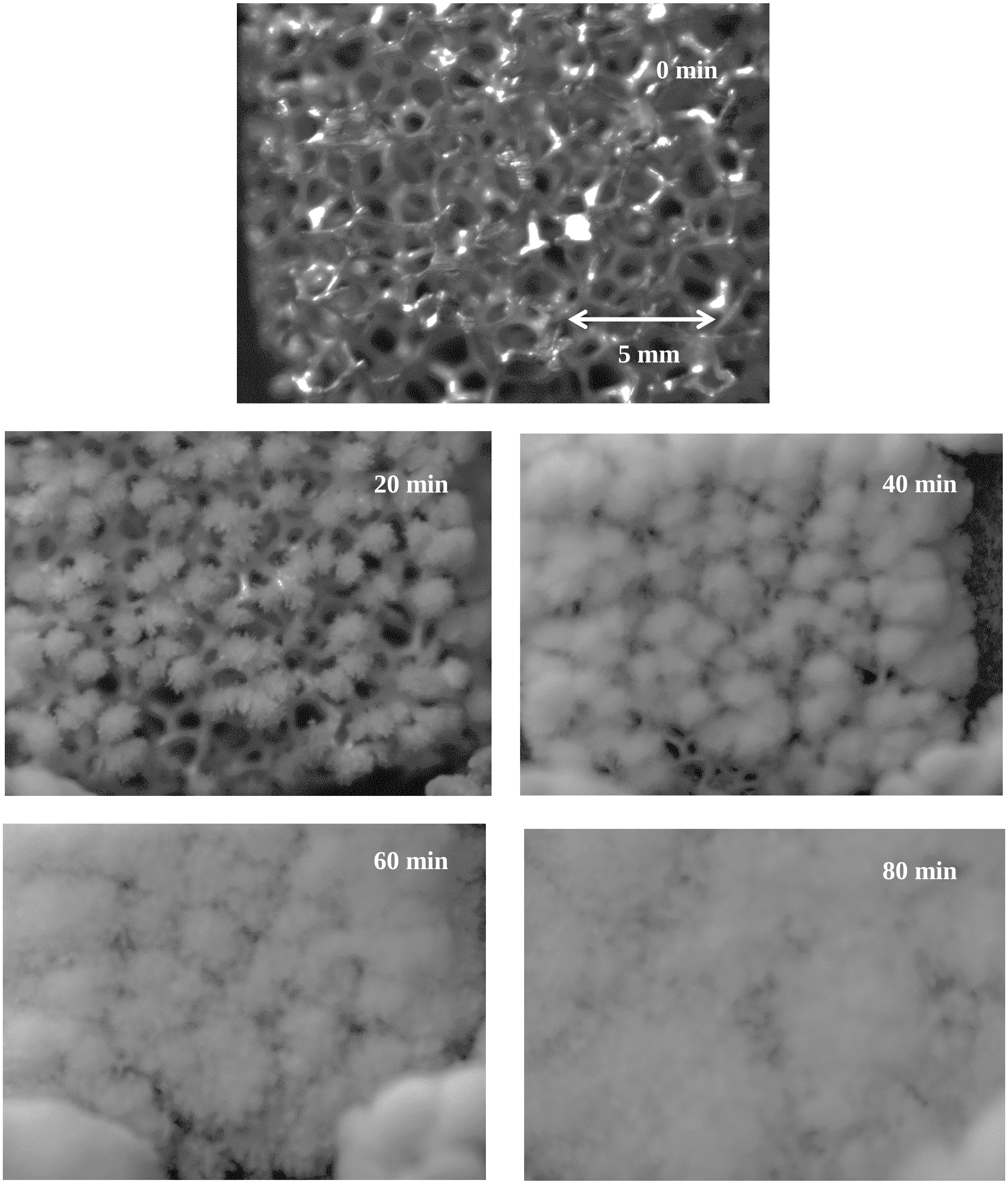

Figure C.4 Frost growth on 20 PPI aluminum foam

Appendix D-Synthesis of silica aerogels

D.1 Introduction

Silica aerogels are manufactured by the sol-gel process. An appropriate solvent is mixed with precipitator (Solution A). An appropriate amount of diluted catalyst is mixed with solvent (solution B). Solution A and B are mixed together and after certain amount of time, depending on the ingredients, a wet gel is formed. Some suitable solvents, precipitators and catalyst for manufacturing silica aerogels are presented in Table D.1.

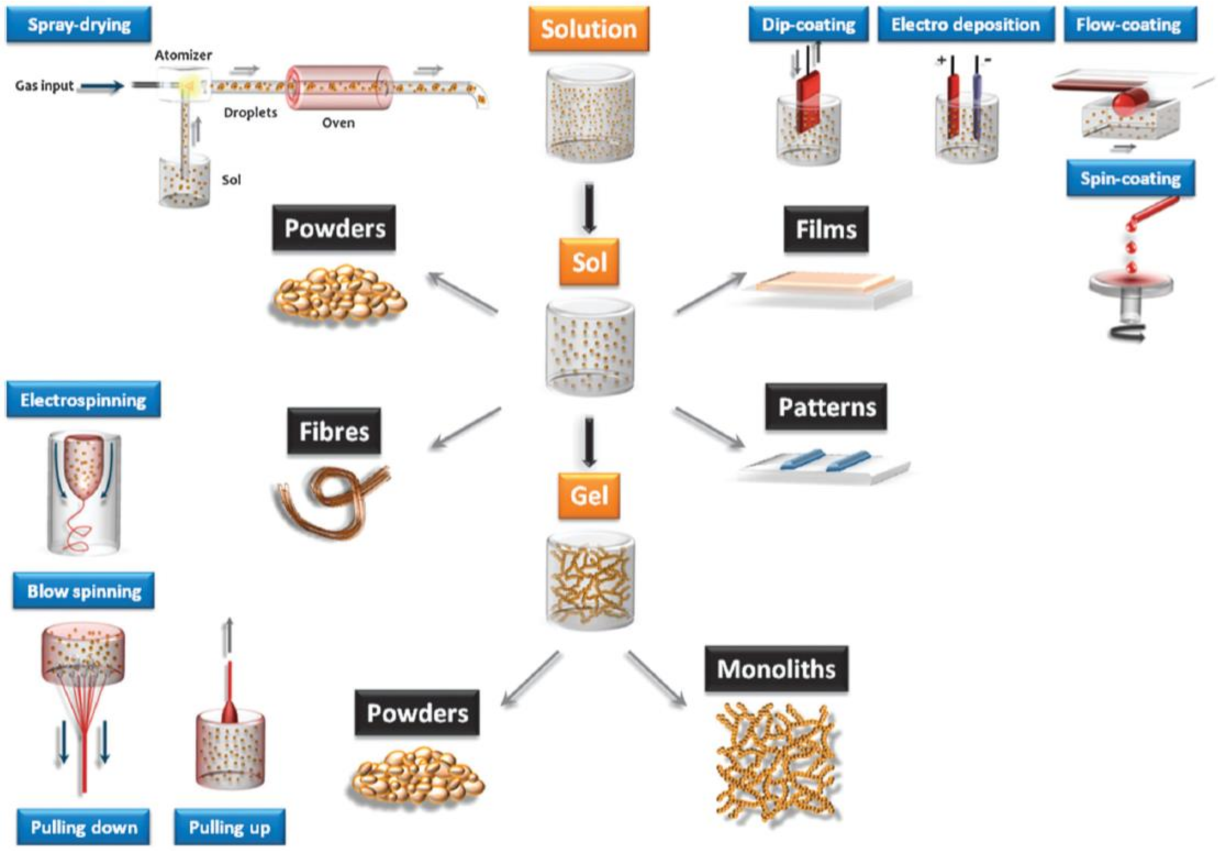

Figure D.1 Processing routes to materials using sol–gel methods [D.1]

Table D.1 Preparation scheme of silica aerogels

Solvent	**Precipitator**	**Catalysts**
Methanol	TMOS	HCl, HF, HNO_3,Citric acid, H_2O_2, NH_4F, NH_4OH, KOH, NaOH
	TOES	HCl, HF, HNO_3, NH_4OH, KOH, NaOH
Ethanol	TMOS	HCl, HF, HNO_3,Citric acid, H_2O_2, NH_4F, NH_4OH, KOH, NaOH
	TOES	HCl, HF, HNO3, NH_4OH, KOH, NaOH
Propanol	TOES	HCl, HF, HNO_3,Citric acid, H_2O_2, NH_4F, NH_4OH, KOH, NaOH
Isopropanol	TMOS	HCl, HF, HNO_3,Citric acid, H_2O_2, NH_4F, NH_4OH, KOH, NaOH
	TOES	HCl, HF, HNO_3, NH_4OH, KOH, NaOH

D.2 Sol-gel chemistry

The kinetics of the sol-gel process is presented by following equations

Hydrolysis

$$Si(OCH_3)_4 + 4H_2O \rightarrow Si(OH)_4 + 4CH_3OH \qquad (D.1)$$

Condensation

$$Si(OH)_4 + Si(OH)_4 \rightarrow \equiv Si - O - Si \equiv +4H_2O \qquad (D.2)$$

$$Si(OH)_4 + Si(OCH_3)_4 \rightarrow \equiv Si - O - Si \equiv +4CH_3OH \qquad (D.3)$$

The simplified structure of silica aerogel network is presented in Figure D.2.

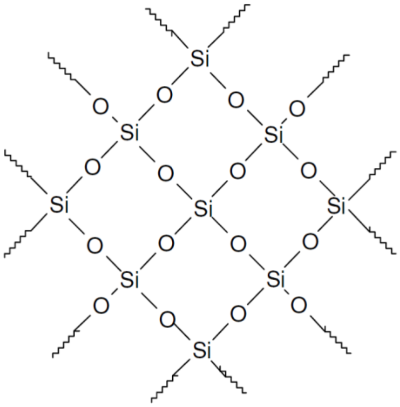

Figure D.2 Structure of silica aerogel network [A.1]

D.3 Super-critical drying process

After obtaining the wet gel, sample is dried to remove the solvent. In order to avoid the cracking and shirking of the resulting structure, solvent is removed by supercritical drying process to avoid the surface tension effects causing the internal pressure (Figure D.3). Freeze drying process is another option, where the solid solvent is sublimated from the structure. Though commonly observed in drying of food product, it is seldom used for application related to organic solvent removal due to the cost and time required for the completion of the process

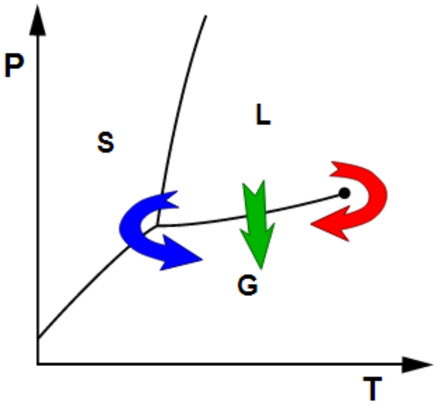

Figure D.3 Supercritical drying, drying through evaporation, freeze drying

Most of the times the solvent in the structure is replaced with carbondioxide and the drying process are carried out under super-critical conditions for CO_2 to dry the sample through an economical and safer process (Figure D.4).

It can be observed in Table D.2 that the critical temperature and pressure for CO_2 is relatively lower than most of the solvent and other replacing fluids used in sol-gel process.

Table D.2 Critical point temperatures and pressures of some fluids

Fluid	Critical temperature T_C (^oC)	Critical pressure P_C (MPa)	Remarks
Carbon dioxide	31.2	7.38	-
Ammonia	132.4	11.29	Toxic
Water	374.1	22.1	High T_C, Corrosive
Ethane	32.5	4.91	Flammable
Propane	96.8	4.26	Flammable
Cyclohenxane	279.9	4.03	High T_C
Methanol	240.0	7.95	High T_C
Ethanol	243.1	6.39	High T_C
Isopropanol	235.6	5.37	High T_C
Acetone	235.0	4.76	High T_C

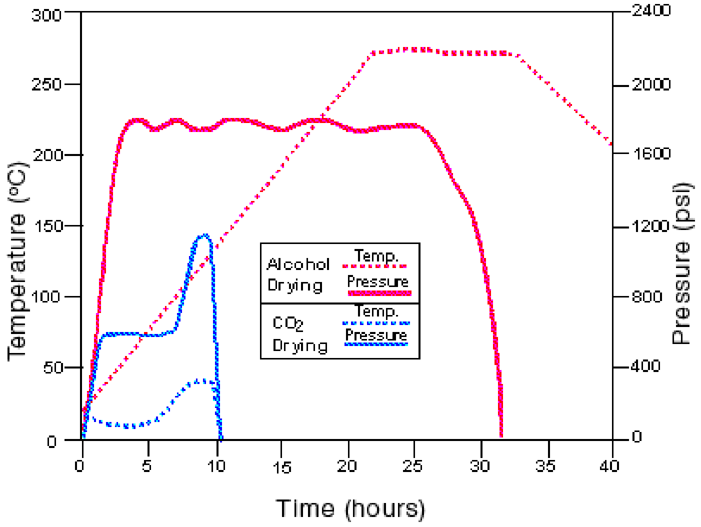

Figure D.4 Critical drying process

The critical drying process is performed in special autoclaves. One such apparatus is presented in Figure D.5.

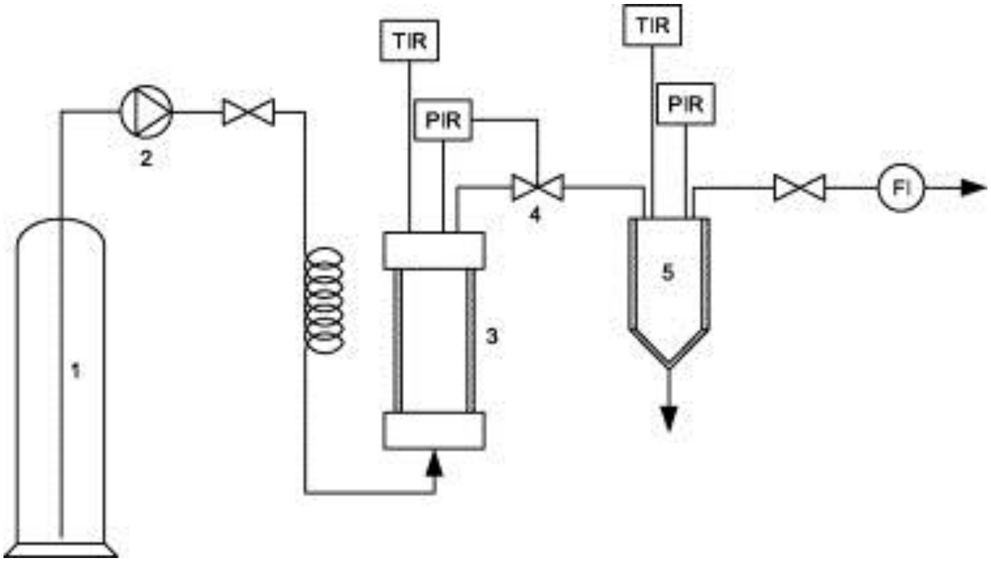

Figure D.5 Experimental apparatus for super critical CO_2 drying: (1) liquid CO_2 cylinder, (2) high-pressure pump, (3) autoclave, (4) micrometering valve, (5) separator, TIR, temperature indicator and regulator, PIR, pressure indicator and regulator, FI, flow indicator.[A2]

Some silica aerogel samples are prepared by different catalyst used in the sol-gel process are presented in Figure D.6.

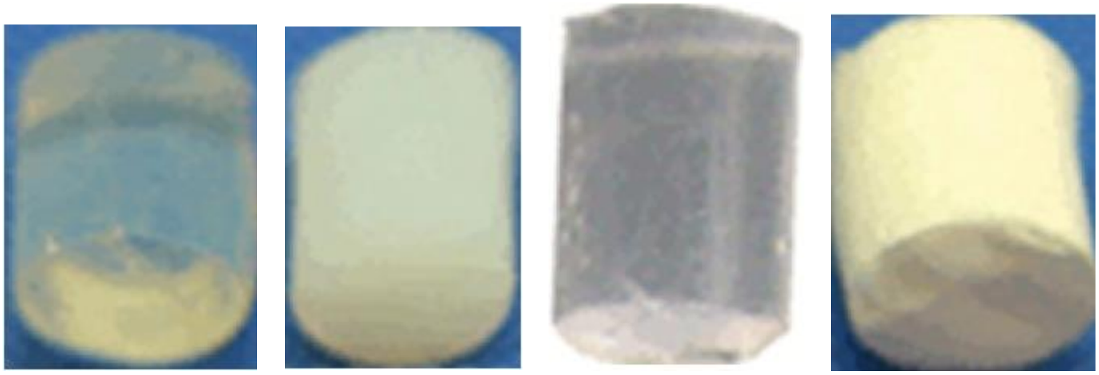

Hydrofluoric acid Sodium hydroxide Ammonium hydroxide Potassium hydroxide

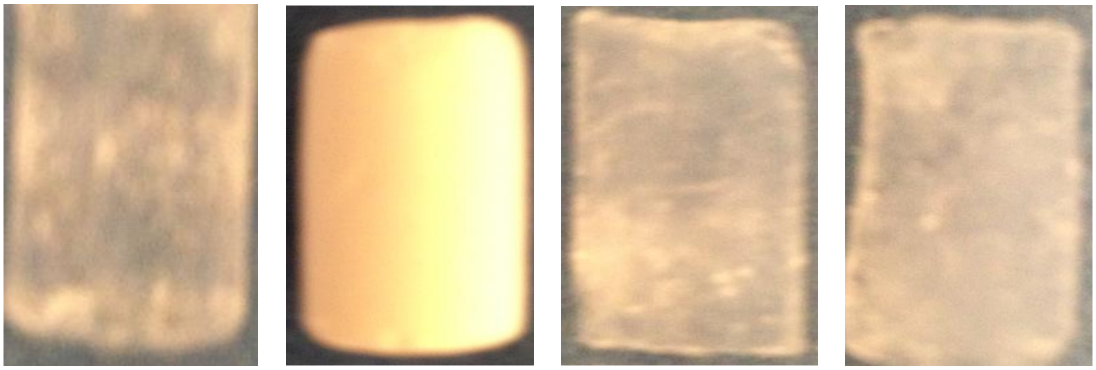

Sulphuric acid Hydrochloric acid Nitric acid Hydrogen peroxide

Figure D.6 Silica aerogel samples prepared by different catalysts

D.4 References

[D.1]. C. Sanchez, P. Belleville, M. Popall, L. Nicole, Applications of advanced hybrid organic–inorganic nanomaterials: from laboratory to market (A critical review), Chemical Society Reviews 4 (2) (2011) 696-753.

[D.2]. K. Kupiec, P. Konieczka, J. Namiesnik, Characteristics, Chemical Modification Processes as well as the Application of Silica and its Modified Forms, Critical Reviews in Analytical Chemistry 39 (2009) 60–69.

[D.3]. M. Paljevac, M. Primozic, M. Habulin, Z. Novak, Z. Knez, Hydrolysis of carboxymethyl cellulose catalyzed by cellulase immobilized on silica gels at low and high pressures, Journal of Supercritical Fluids 43 (1) (2007) 74-80.

Appendix E- Cyclic dynamic vapor sorption (DVS) experiments

These tests were conducted to determine the repeatability of adsorption/desorption performance of silica aerogel coated foams. Representative data for sample coated with silica aerogel prepared by ammonium hydroxide catalyst is presented.

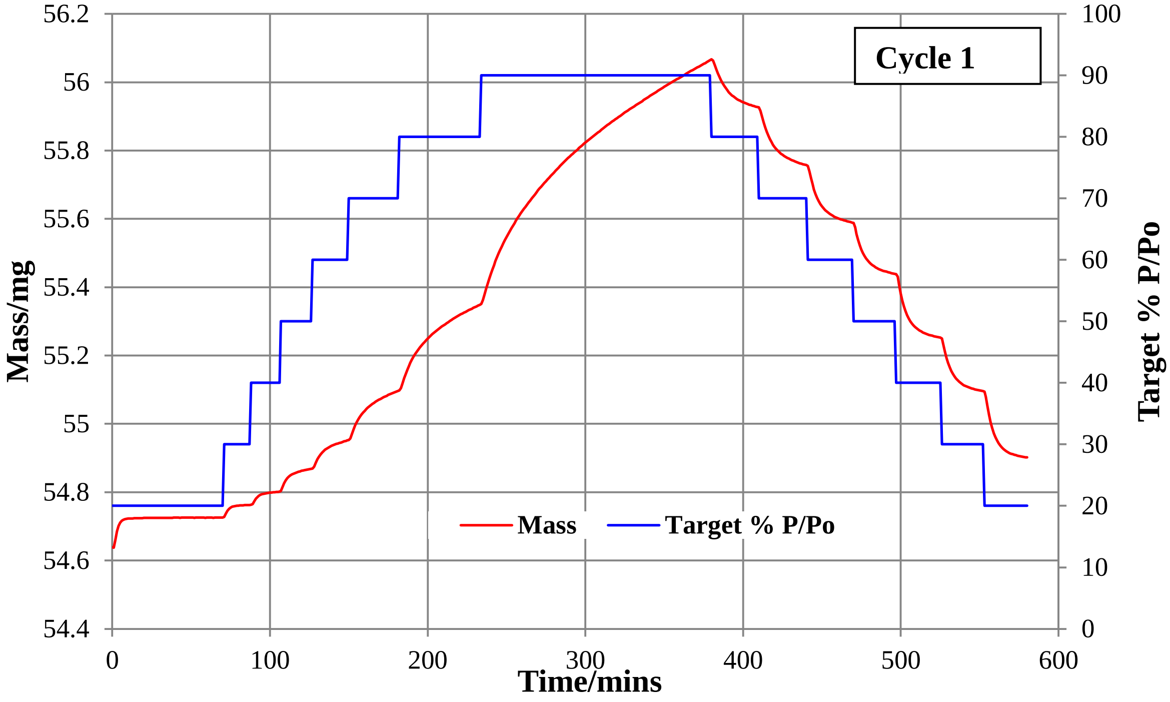

Figure E.1 Cyclic dynamic vapor sorption data (Cycle 1)

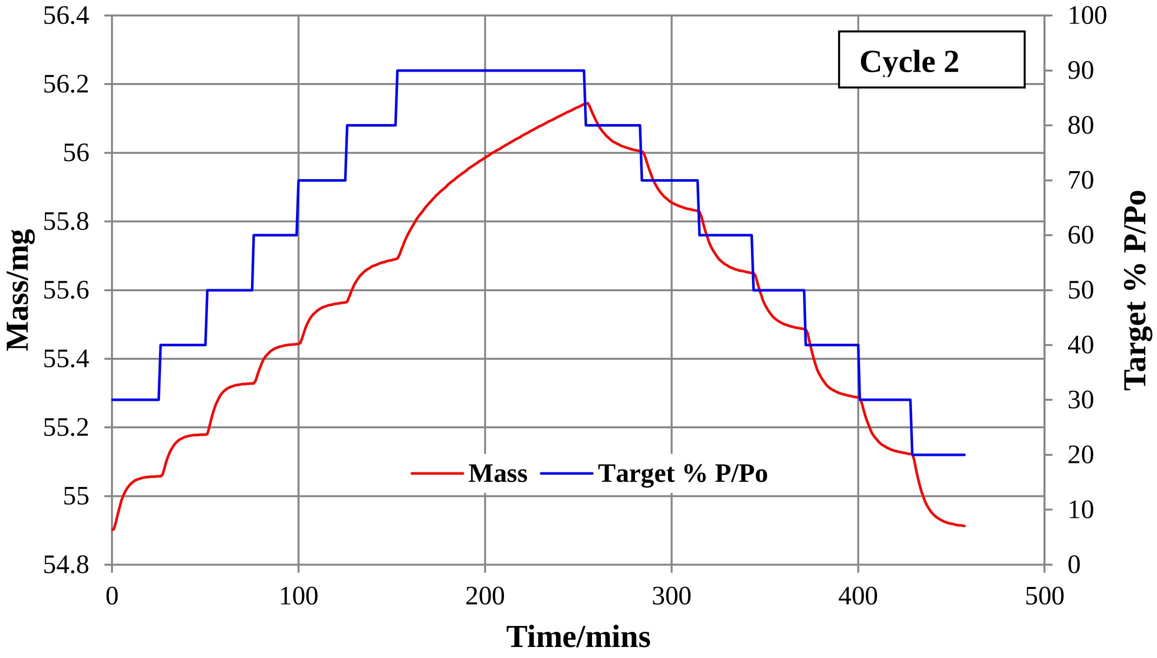

Figure E.2 Cyclic dynamic vapor sorption data (Cycle 2)

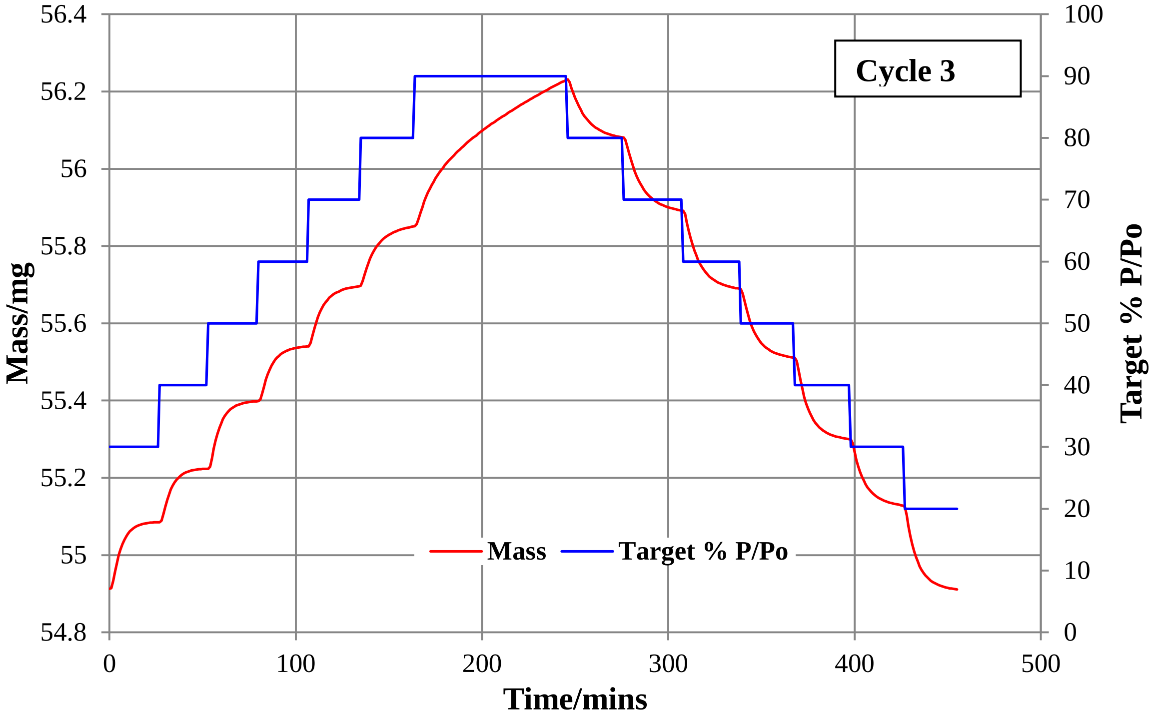

Figure E.3 Cyclic dynamic vapor sorption data (Cycle 3)

Appendix F- Non-equilibrium adsorption and desorption isotherms

F.1 Experimental apparatus

In order to evaluate the dynamic performance of aerogels as desiccants, transient (non-equilibrium) test were conducted. For such experiments an AquaSorp (*Decagon Devices*) was used, which is a standard device used to determine the sorption and desorption isotherms.

The AquaSorp creates isotherms using a water activity and gravimetric analysis method called Dynamic Dewpoint Isotherm (DDI). The apparatus controls neither water content nor water activity, but dries or wets the sample and measures water activity and water content during the wetting or drying process. Water content is determined by weighing the sample using a high precision magnetic force balance. Water activity is determined using a chilled-mirror dewpoint sensor. Drying of the sample is imposed by flowing dry air from a desiccant tube across the sample. Wetting of the sample is achieved by saturating the air with water before it enters the chamber and flows across the sample. The water reservoir is used to ensure humidity saturation and minimize temperature fluctuation. The AquaSorp consists of a case which houses the power supply, air pump, balance, temperature controlled sample chamber, sensor block, sensor and temperature control electronics, water reservoir, and desiccant supply (Figure F.1).

The range for changing the relative humidity in the chamber is 3%-95% (RH), with an accuracy of 0.5% and a repeatability of 0.3%. The temperature can be changed between 0^{o}C to 60^{o}C.

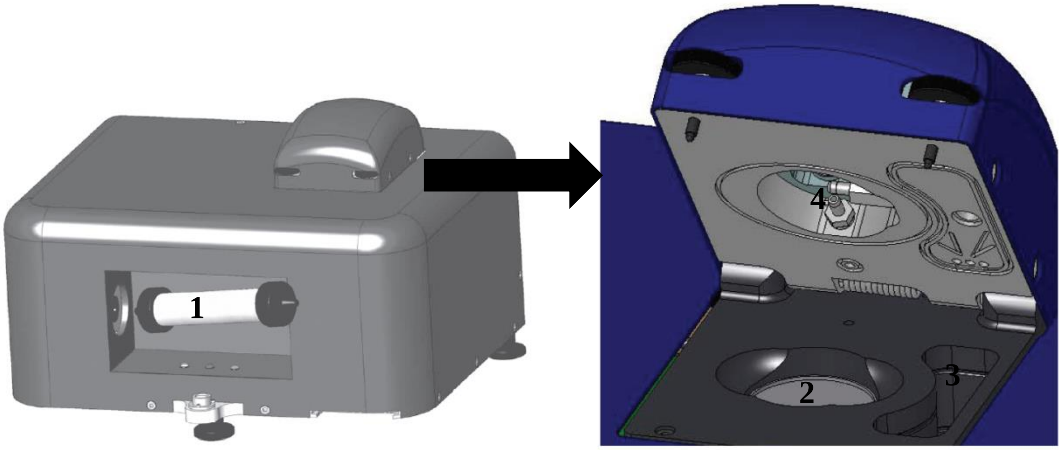

Figure F.1 Aquasorp apparatus (*Decagon Devices Inc*.) (1) desiccant (2) sample pan on the fine microbalance (3) water reservoir (4) humidity sensors

F.2 Brunauer classification of moisture adsorption isotherms

Brunauer has classified the dynamics isotherms into three classes as shown in Figure.

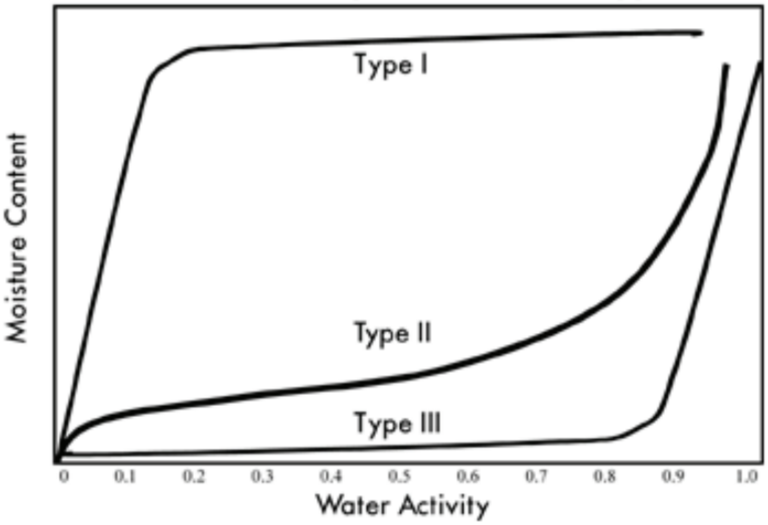

Figure F.2 Moisture adsorption isotherm types

Type I isotherms are typical of anti-caking agents. These types of ingredients absorb water onto polar sites and into non-swelling capillaries, which results in high amounts of moisture being held at low water activities. Type II isotherms describes most types of products. The isotherms shape for these types of products is sigmoidal, characterized by sharp changes in moisture content at low and high water activities, but small changes in moisture content over the intermediate moisture range. Type III isotherms are typical of crystalline substances. For this type of isotherm, there is very little moisture gain initially because water is only interacting with the surface of the crystal through hydrogen bonds. Increasing the surface area of the crystal will increase the moisture content at low water activities. Eventually, as water activity increases, the water will dissolve the crystal (often called deliquescence). At this point, the moisture content starts to increase dramatically as the material goes into solution.

F.3 Isotherm models

Different isotherm models have been proposed and compared in the literature. These models are necessary to predict the moisture content at a given water activity and are used to evaluate thermodynamic functions of water in adsorbents. The most commonly used models are the GAB and BET. Since the BET model is only applicable up to 0.50, the GAB model is widely accepted as the most useful for characterizing isotherms across the entire water activity range. A new model called the Double Log Polynomial (DLP) has proven to be even better than the GAB at characterizing complex isotherms. The model equations are shown below.

$$\text{BET: } m = \frac{a_w m_0 c}{(1-a_w)[1+a_w(c-1)]} \qquad (F.1)$$

Where m is the moisture in g/100 solids or g/g solids at water activity a_w and m_0 is the monolayer value in same units. The constant (c) is calculated by $c = e^{\frac{\Delta H}{RT}}$ Where ΔH is the surface interaction energy cal/mole, R is the gas constant and T is the Kelvin temperature.

$$\text{GAB:} m = \frac{m_0 k_b C_1 a_w}{(1-k_b a_w)[1-k_b a_w+k_b C_1 a_w]} \qquad (F.2)$$

Where (m) is the moisture in g/100 solids or g/g solids, k_b is a constant in the range of 0.70 to 1 and C_1 is a constant in the range of 1 to 2000. In addition, m_0 is the monolayer water content in the same units as m and $a_w$is the water activity at moisture m.

$$\text{DLP:} m = b_3x^3 + b_2x^2 + b_1x + b_0 \qquad (F.3)$$

Where (m) is the moisture in g/100 solids or g/g solids, $x = ln(-ln(a_w))$ and b_0 - b_3 are empirical constants.

F.4 Non-equilibrium adsorption desorption isotherms

Non-equilibrium adsorption/desorption isotherms and the associated DLP model for four different silica aerogel coated metal foam samples are presented in following Figures.

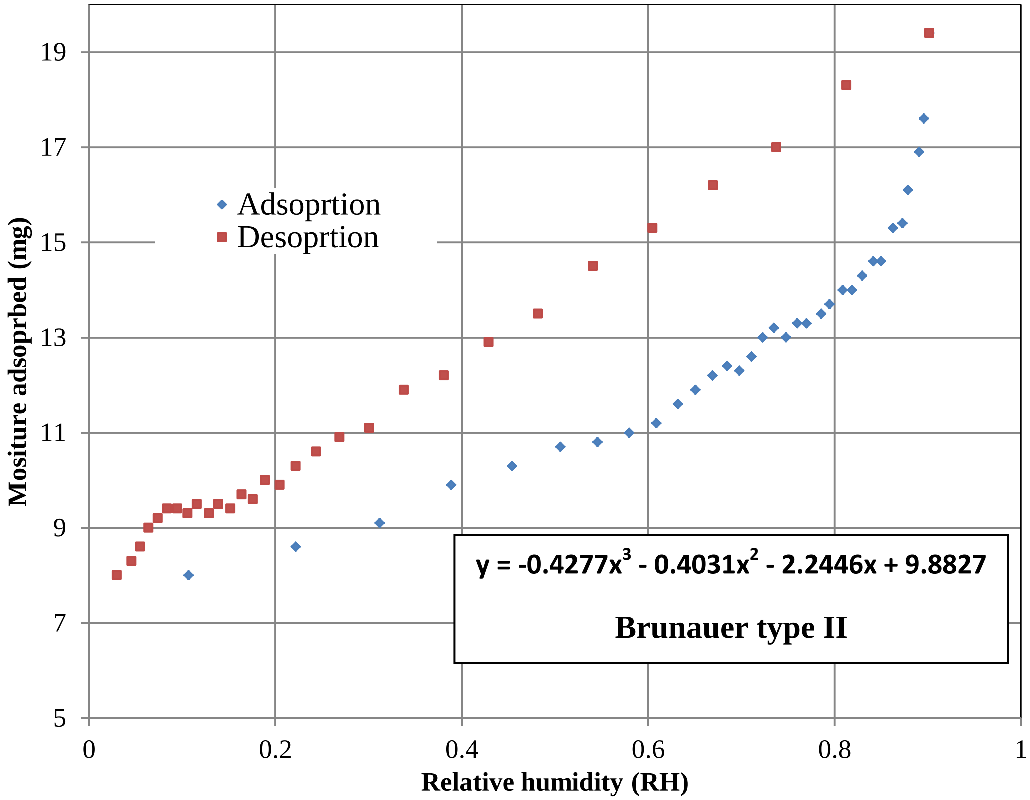

Figure F.3 Moisture adoption isotherm (Potassium hydroxide)

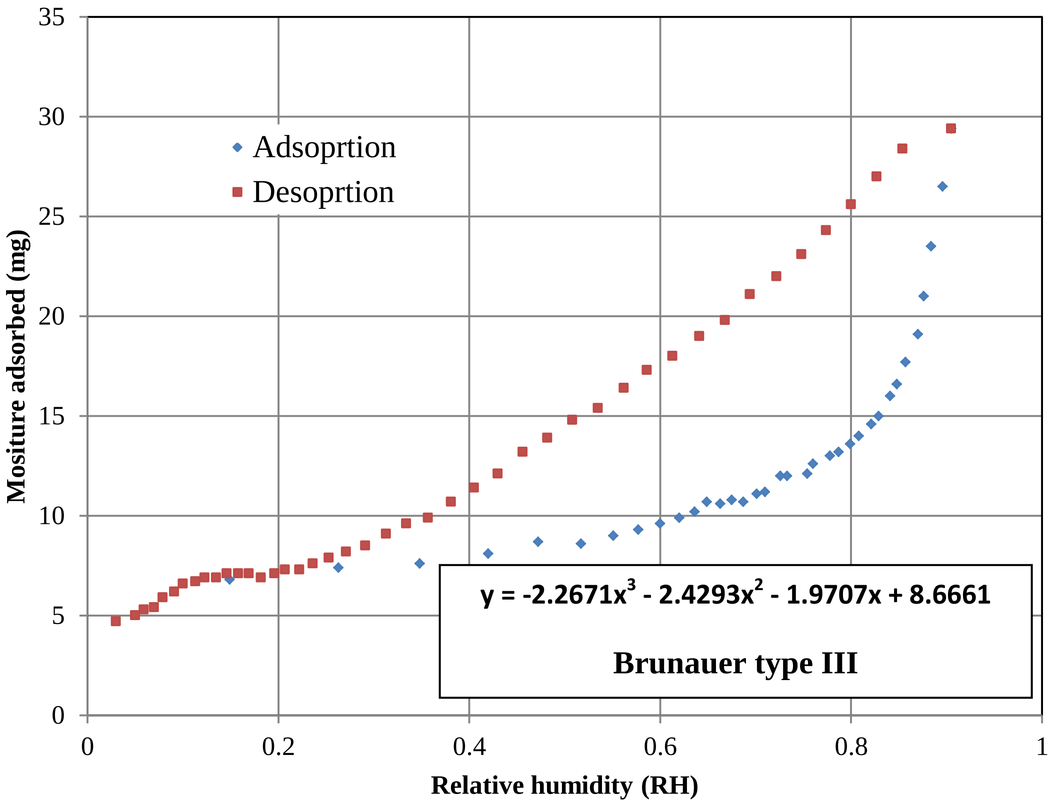

Figure F.4 Moisture adoption isotherm (Hydrofluoric acid)

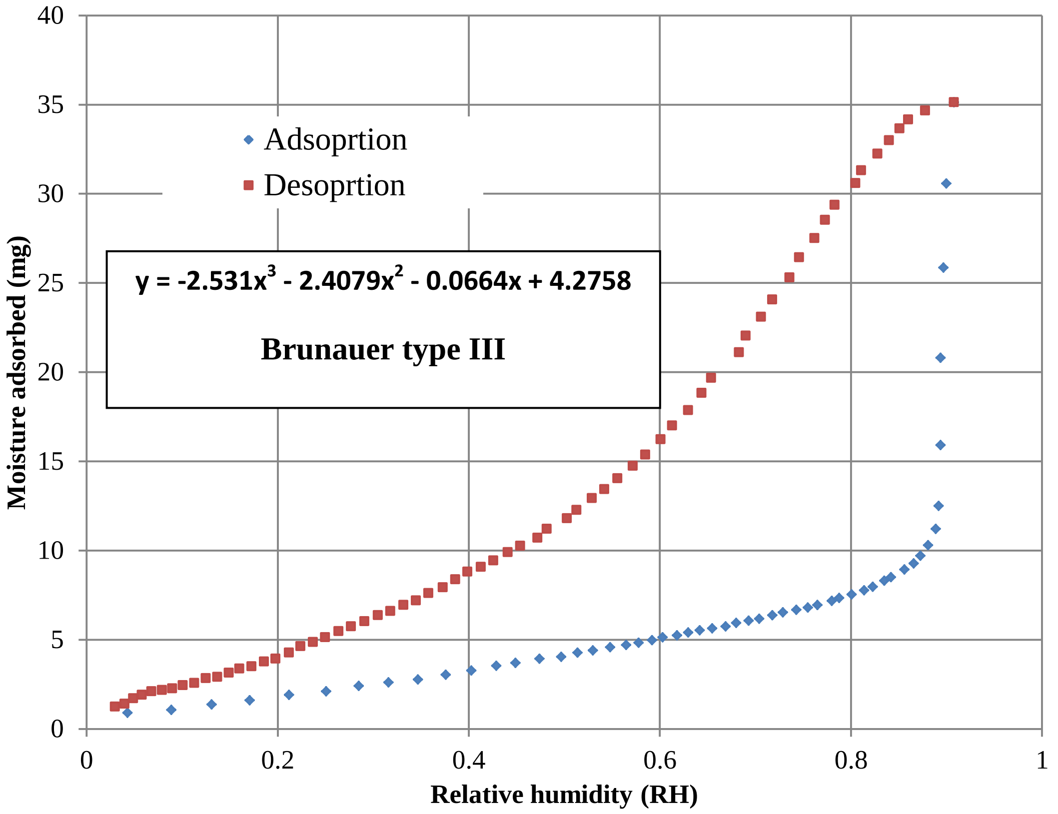

Figure F.5 Moisture adoption isotherm (Ammonium hydroxide)

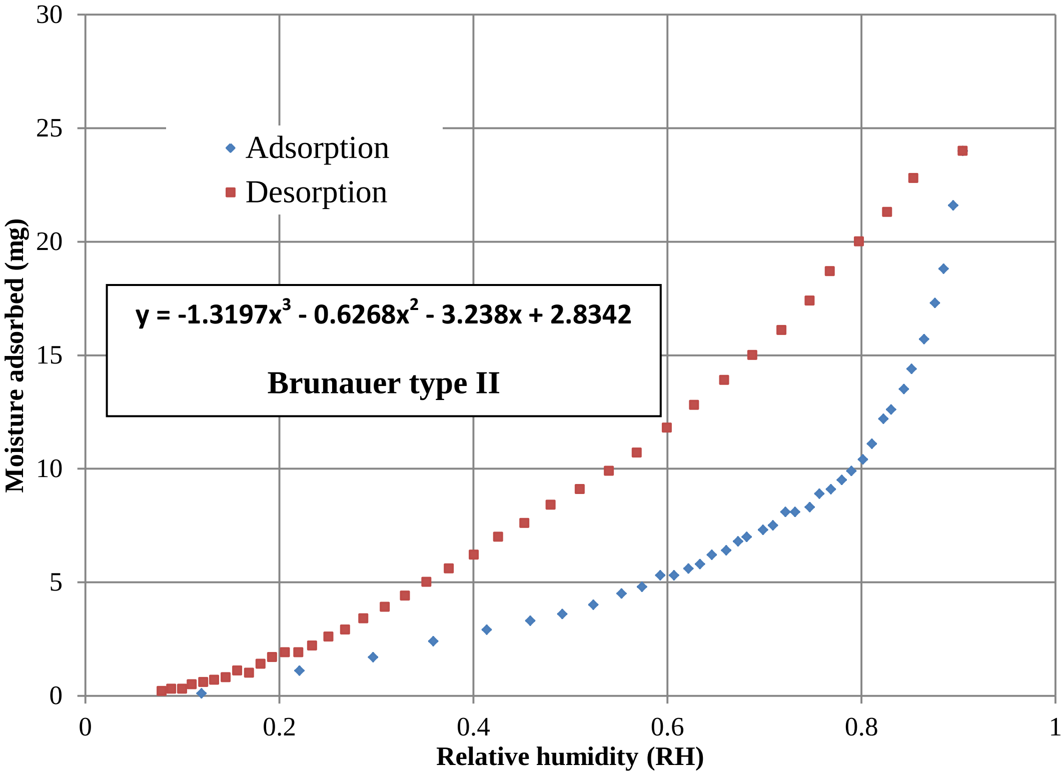

Figure F.6 Moisture adoption isotherm (Hydrogen peroxide)

Appendix G- Deformation of silica aerogels upon adsorption and desorption

Desiccators were prepared using the saturated salt solutions. The values for relative humidity for specific salt solution at 25°C are presented in Table G.1

Table G.1 Relative humidity values for different salt solutions at 25°C

Salt solution	**Relative humidity (%)**	**Salt solution**	**Relative humidity (%)**
LiBr	6.37	KI	68.86
LiCl	11.30	NaCl	75.29
CH_3COOK	22.51	KCl	84.34
$MgCl_2$	32.78	$BaCl_2$	90.30
K_2CO_3	43.16	KNO_3	93.58
NaBr	57.57	K_2SO_4	97.30

Silica aerogel samples at equilibrium with room humidity of 40% were exposed to different values of relative humidity in desiccators. The deformations of the samples were observed from the images (Figure G.1). Sample samples were passed through an adsorption and desorption cycle. Images of the samples are presented in Figure G.2. Sample 1 and 2 were synthesized from potassium hydroxide and ammonium hydroxide respectively, which were used in sol-gel process as catalysts.

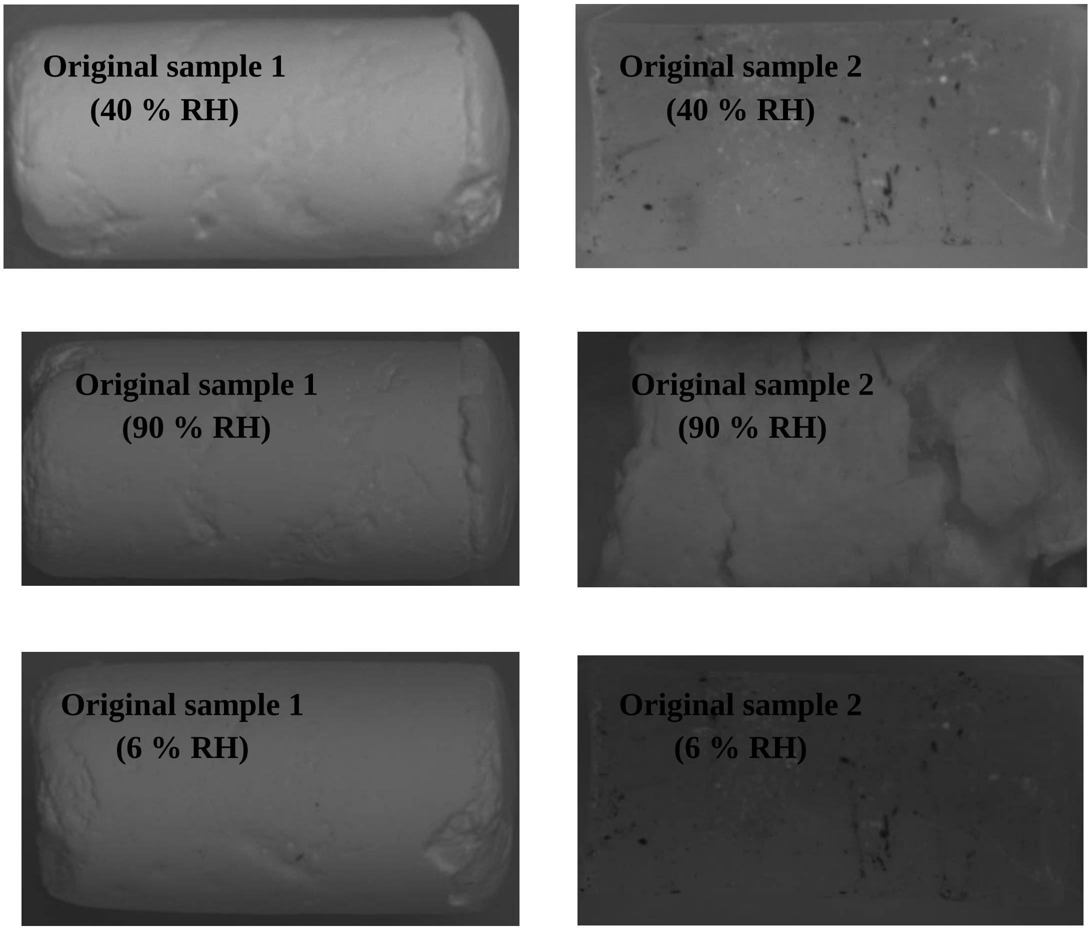

Figure G.1 Adsorption/desorption in desiccators

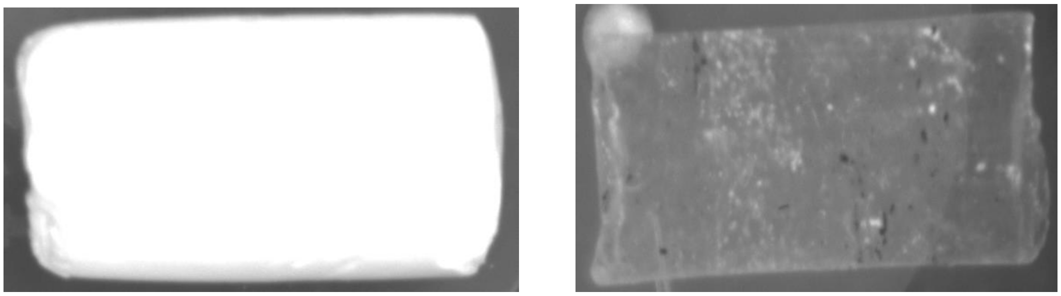

Figure G.2 Adsorption/desorption cycle in DVS apparatus

Appendix H-Roots of Eigen equations

$$\lambda_n \tan(\lambda_n) = Bi_m$$

Bi_m	λ_1	λ_2	λ_3	λ_4	λ_5	λ_6	λ_7	λ_8	λ_9	λ_{10}
10	1.429	4.306	7.228	10.2	13.21	16.5	19.33	22.41	25.51	28.61
30.2	1.52	4.562	7.607	10.66	13.71	16.77	19.84	22.91	25.99	29.08
50.41	1.54	4.621	7.702	10.78	13.87	16.95	20.04	23.13	26.22	29.32
70.61	1.549	4.647	7.745	10.84	13.94	17.04	20.14	23.24	26.35	29.45
90.82	1.554	4.661	7.769	10.88	13.98	17.09	20.2	23.31	26.42	29.53
111	1.557	4.67	7.784	10.9	14.01	17.13	20.24	23.35	26.47	29.58
131.2	1.559	4.677	7.795	10.91	14.03	17.15	20.27	23.39	26.5	29.62
151.4	1.56	4.681	7.803	10.92	14.04	17.17	20.29	23.41	26.53	29.65
171.6	1.562	4.685	7.809	10.93	14.06	17.18	20.3	23.43	26.55	29.67
191.8	1.563	4.688	7.813	10.94	14.06	17.19	20.31	23.44	26.57	29.69
212	1.563	4.69	7.817	10.94	14.07	17.2	20.32	23.45	26.58	29.71
232.2	1.564	4.692	7.82	10.95	14.08	17.2	20.33	23.46	26.59	29.72
252.4	1.565	4.694	7.823	10.95	14.08	17.21	20.34	23.47	26.6	29.73
272.7	1.565	4.695	7.825	10.96	14.09	17.22	20.35	23.48	26.61	29.74
292.9	1.565	4.696	7.827	10.96	14.09	17.22	20.35	23.48	26.61	29.74
313.1	1.566	4.697	7.829	10.96	14.09	17.22	20.36	23.49	26.62	29.75
333.3	1.566	4.698	7.83	10.96	14.09	17.23	20.36	23.49	26.62	29.76
353.5	1.566	4.699	7.832	10.96	14.1	17.23	20.36	23.5	26.63	29.76
373.7	1.567	4.7	7.833	10.97	14.1	17.23	20.37	23.5	26.63	29.77
393.9	1.567	4.7	7.834	10.97	14.1	17.24	20.37	23.5	26.64	29.77
414.1	1.567	4.701	7.835	10.97	14.1	17.24	20.37	23.51	26.64	29.77
434.3	1.567	4.702	7.836	10.97	14.1	17.24	20.37	23.51	26.64	29.78
454.5	1.567	4.702	7.837	10.97	14.11	17.24	20.38	23.51	26.64	29.78
474.7	1.567	4.702	7.837	10.97	14.11	17.24	20.38	23.51	26.65	29.78
494.9	1.568	4.703	7.838	10.97	14.11	17.24	20.38	23.51	26.65	29.79
515.1	1.568	4.703	7.839	10.97	14.11	17.25	20.38	23.52	26.65	29.79
535.3	1.568	4.704	7.839	10.98	14.11	17.25	20.38	23.52	26.65	29.79
555.5	1.568	4.704	7.84	10.98	14.11	17.25	20.38	23.52	26.66	29.79
575.7	1.568	4.704	7.84	10.98	14.11	17.25	20.38	23.52	26.66	29.79
595.9	1.568	4.704	7.841	10.98	14.11	17.25	20.39	23.52	26.66	29.8
616.1	1.568	4.705	7.841	10.98	14.11	17.25	20.39	23.52	26.66	29.8
636.3	1.568	4.705	7.842	10.98	14.11	17.25	20.39	23.52	26.66	29.8
656.5	1.568	4.705	7.842	10.98	14.12	17.25	20.39	23.53	26.66	29.8
676.7	1.568	4.705	7.842	10.98	14.12	17.25	20.39	23.53	26.66	29.8
696.9	1.569	4.706	7.843	10.98	14.12	17.25	20.39	23.53	26.67	29.8
717.1	1.569	4.706	7.843	10.98	14.12	17.25	20.39	23.53	26.67	29.8
737.3	1.569	4.706	7.843	10.98	14.12	17.26	20.39	23.53	26.67	29.8
757.6	1.569	4.706	7.844	10.98	14.12	17.26	20.39	23.53	26.67	29.81

777.8	1.569	4.706	7.844	10.98	14.12	17.26	20.39	23.53	26.67	29.81
798	1.569	4.706	7.844	10.98	14.12	17.26	20.39	23.53	26.67	29.81
818.2	1.569	4.707	7.844	10.98	14.12	17.26	20.4	23.53	26.67	29.81
838.4	1.569	4.707	7.845	10.98	14.12	17.26	20.4	23.53	26.67	29.81
858.6	1.569	4.707	7.845	10.98	14.12	17.26	20.4	23.53	26.67	29.81
878.8	1.569	4.707	7.845	10.98	14.12	17.26	20.4	23.54	26.67	29.81
899	1.569	4.707	7.845	10.98	14.12	17.26	20.4	23.54	26.67	29.81
919.2	1.569	4.707	7.845	10.98	14.12	17.26	20.4	23.54	26.67	29.81
939.4	1.569	4.707	7.846	10.98	14.12	17.26	20.4	23.54	26.68	29.81
959.6	1.569	4.707	7.846	10.98	14.12	17.26	20.4	23.54	26.68	29.81
979.8	1.569	4.708	7.846	10.98	14.12	17.26	20.4	23.54	26.68	29.81
1000	1.569	4.708	7.846	10.98	14.12	17.26	20.4	23.54	26.68	29.82

$$-\frac{\mu_m}{\tan(\mu_m)} = Bi_t$$

Bi_t	μ_1	μ_2	μ_3	μ_4	μ_5	μ_6	μ_7	μ_8	μ_9	μ_{10}
0.001	0	1.571	4.713	7.854	11	14.14	17.28	20.42	23.56	26.7
1.021	0	2.036	4.917	7.981	11.09	14.21	17.34	20.47	23.61	26.74
2.042	0	2.297	5.094	8.101	11.18	14.28	17.4	20.52	23.65	26.78
3.062	0	2.464	5.241	8.211	11.26	14.35	17.45	20.57	23.69	26.82
4.083	0	2.578	5.363	8.311	11.34	14.41	17.51	20.62	23.73	26.85
5.103	0	2.661	5.464	8.4	11.42	14.48	17.56	20.66	23.77	26.89
6.123	0	2.723	5.547	8.479	11.49	14.54	17.61	20.71	23.81	26.93
7.144	0	2.772	5.617	8.55	11.55	14.59	17.66	20.75	23.85	26.96
8.164	0	2.81	5.676	8.613	11.61	14.65	17.71	20.79	23.89	27
9.184	0	2.842	5.726	8.668	11.66	14.7	17.76	20.84	23.93	27.03
10.2	0	2.868	5.769	8.718	11.71	14.74	17.8	20.88	23.96	27.06
11.23	0	2.89	5.806	8.762	11.76	14.79	17.84	20.91	24	27.1
12.25	0	2.908	5.838	8.802	11.8	14.83	17.88	20.95	24.03	27.13
13.27	0	2.925	5.867	8.837	11.84	14.87	17.92	20.98	24.07	27.16
14.29	0	2.939	5.892	8.869	11.87	14.9	17.95	21.02	24.1	27.19
15.31	0	2.951	5.914	8.898	11.91	14.93	17.98	21.05	24.13	27.22
16.33	0	2.962	5.935	8.925	11.94	14.97	18.02	21.08	24.16	27.24
17.35	0	2.972	5.953	8.949	11.96	15	18.04	21.11	24.18	27.27
18.37	0	2.981	5.969	8.97	11.99	15.02	18.07	21.14	24.21	27.3
19.39	0	2.989	5.984	8.991	12.01	15.05	18.1	21.16	24.24	27.32
20.41	0	2.996	5.997	9.009	12.03	15.07	18.12	21.19	24.26	27.34
21.43	0	3.002	6.01	9.026	12.05	15.09	18.15	21.21	24.28	27.37
22.45	0	3.008	6.021	9.042	12.07	15.12	18.17	21.23	24.31	27.39
23.47	0	3.014	6.032	9.057	12.09	15.14	18.19	21.26	24.33	27.41
24.49	0	3.019	6.041	9.07	12.11	15.15	18.21	21.28	24.35	27.43
25.51	0	3.024	6.05	9.083	12.12	15.17	18.23	21.3	24.37	27.45
26.53	0	3.028	6.059	9.095	12.14	15.19	18.25	21.31	24.39	27.47
27.55	0	3.032	6.066	9.106	12.15	15.2	18.26	21.33	24.41	27.49
28.57	0	3.036	6.074	9.116	12.16	15.22	18.28	21.35	24.43	27.51
29.59	0	3.039	6.081	9.126	12.18	15.23	18.3	21.37	24.44	27.53
30.61	0	3.043	6.087	9.135	12.19	15.25	18.31	21.38	24.46	27.54
31.63	0	3.046	6.093	9.143	12.2	15.26	18.32	21.4	24.47	27.56
32.65	0	3.049	6.099	9.152	12.21	15.27	18.34	21.41	24.49	27.57
33.67	0	3.051	6.104	9.159	12.22	15.28	18.35	21.42	24.5	27.59
34.69	0	3.054	6.109	9.166	12.23	15.29	18.36	21.44	24.52	27.6
35.71	0	3.056	6.114	9.173	12.24	15.3	18.37	21.45	24.53	27.62
36.73	0	3.059	6.118	9.18	12.24	15.31	18.39	21.46	24.54	27.63
37.76	0	3.061	6.122	9.186	12.25	15.32	18.4	21.47	24.56	27.64
38.78	0	3.063	6.126	9.192	12.26	15.33	18.41	21.49	24.57	27.65

39.8	0	3.065	6.13	9.198	12.27	15.34	18.42	21.5	24.58	27.67
40.82	0	3.067	6.134	9.203	12.27	15.35	18.43	21.51	24.59	27.68
41.84	0	3.068	6.138	9.208	12.28	15.36	18.43	21.52	24.6	27.69
42.86	0	3.07	6.141	9.213	12.29	15.36	18.44	21.53	24.61	27.7
43.88	0	3.072	6.144	9.218	12.29	15.37	18.45	21.53	24.62	27.71
44.9	0	3.073	6.147	9.222	12.3	15.38	18.46	21.54	24.63	27.72
45.92	0	3.075	6.15	9.226	12.3	15.38	18.47	21.55	24.64	27.73
46.94	0	3.076	6.153	9.231	12.31	15.39	18.47	21.56	24.65	27.74
47.96	0	3.078	6.156	9.235	12.32	15.4	18.48	21.57	24.66	27.75
48.98	0	3.079	6.158	9.238	12.32	15.4	18.49	21.58	24.67	27.76
50	0	3.08	6.161	9.242	12.32	15.41	18.5	21.58	24.67	27.77

$$-Y_0\left(\frac{\mu_m r_1}{r_2}\right)[\mu_m J_1(\mu_m) - Bi_T J_0(\mu_m)] = J_0\left(\frac{\mu_m r_1}{r_2}\right)[Bi_T Y_0(\mu_m) - \mu_m Y_1(\mu_m)]$$

(5 PPI coated foam)

Bi_t	μ_1	μ_2	μ_3	μ_4	μ_5	μ_6	μ_7	μ_8	μ_9	μ_{10}
0.001	11.05	34.05	56.88	79.67	102.5	125.2	148	170.8	193.6	216.4
1.021	11.7	34.27	57.01	79.76	102.5	125.3	148.1	170.8	193.6	216.4
2.042	12.28	34.48	57.13	79.86	102.6	125.4	148.1	170.9	193.7	216.4
3.062	12.81	34.7	57.26	79.95	102.7	125.4	148.2	170.9	193.7	216.5
4.083	13.29	34.9	57.39	80.04	102.7	125.5	148.2	171	193.7	216.5
5.103	13.72	35.11	57.52	80.13	102.8	125.5	148.3	171	193.8	216.5
6.123	14.12	35.31	57.64	80.22	102.9	125.6	148.3	171.1	193.8	216.6
7.144	14.49	35.5	57.77	80.31	103	125.7	148.4	171.1	193.8	216.6
8.164	14.83	35.69	57.89	80.41	103	125.7	148.4	171.1	193.9	216.6
9.184	15.15	35.88	58.02	80.5	103.1	125.8	148.5	171.2	193.9	216.7
10.2	15.44	36.07	58.14	80.59	103.2	125.8	148.5	171.2	194	216.7
11.23	15.72	36.25	58.26	80.67	103.2	125.9	148.6	171.3	194	216.7
12.25	15.97	36.42	58.38	80.76	103.3	125.9	148.6	171.3	194	216.8
13.27	16.21	36.59	58.5	80.85	103.4	126	148.7	171.4	194.1	216.8
14.29	16.44	36.76	58.61	80.94	103.5	126.1	148.7	171.4	194.1	216.8
15.31	16.65	36.93	58.73	81.03	103.5	126.1	148.8	171.4	194.2	216.9
16.33	16.85	37.09	58.84	81.11	103.6	126.2	148.8	171.5	194.2	216.9
17.35	17.03	37.24	58.96	81.2	103.7	126.2	148.9	171.5	194.2	216.9
18.37	17.21	37.39	59.07	81.28	103.7	126.3	148.9	171.6	194.3	217
19.39	17.38	37.54	59.18	81.37	103.8	126.3	149	171.6	194.3	217
20.41	17.53	37.68	59.29	81.45	103.9	126.4	149	171.7	194.3	217
21.43	17.68	37.82	59.4	81.54	103.9	126.5	149.1	171.7	194.4	217.1
22.45	17.82	37.96	59.5	81.62	104	126.5	149.1	171.7	194.4	217.1
23.47	17.96	38.09	59.61	81.7	104.1	126.6	149.2	171.8	194.5	217.1
24.49	18.08	38.22	59.71	81.78	104.1	126.6	149.2	171.8	194.5	217.2
25.51	18.21	38.35	59.81	81.87	104.2	126.7	149.3	171.9	194.5	217.2
26.53	18.32	38.47	59.91	81.95	104.3	126.7	149.3	171.9	194.6	217.2
27.55	18.43	38.59	60.01	82.03	104.3	126.8	149.3	172	194.6	217.3
28.57	18.54	38.71	60.11	82.1	104.4	126.8	149.4	172	194.6	217.3
29.59	18.64	38.82	60.2	82.18	104.5	126.9	149.4	172	194.7	217.3
30.61	18.73	38.93	60.3	82.26	104.5	127	149.5	172.1	194.7	217.4
31.63	18.82	39.04	60.39	82.34	104.6	127	149.5	172.1	194.7	217.4
32.65	18.91	39.15	60.48	82.41	104.7	127.1	149.6	172.2	194.8	217.4
33.67	19	39.25	60.57	82.49	104.7	127.1	149.6	172.2	194.8	217.5
34.69	19.08	39.35	60.66	82.56	104.8	127.2	149.7	172.2	194.9	217.5
35.71	19.16	39.44	60.75	82.64	104.8	127.2	149.7	172.3	194.9	217.5

36.73	19.23	39.54	60.83	82.71	104.9	127.3	149.8	172.3	194.9	217.6
37.76	19.3	39.63	60.92	82.78	105	127.3	149.8	172.4	195	217.6
38.78	19.37	39.72	61	82.85	105	127.4	149.9	172.4	195	217.6
39.8	19.44	39.81	61.08	82.92	105.1	127.4	149.9	172.4	195	217.7
40.82	19.5	39.89	61.16	82.99	105.1	127.5	150	172.5	195.1	217.7
41.84	19.56	39.98	61.24	83.06	105.2	127.5	150	172.5	195.1	217.7
42.86	19.62	40.06	61.32	83.13	105.3	127.6	150	172.6	195.1	217.8
43.88	19.68	40.14	61.4	83.2	105.3	127.6	150.1	172.6	195.2	217.8
44.9	19.74	40.21	61.47	83.27	105.4	127.7	150.1	172.6	195.2	217.8
45.92	19.79	40.29	61.55	83.33	105.4	127.7	150.2	172.7	195.3	217.9
46.94	19.84	40.36	61.62	83.4	105.5	127.8	150.2	172.7	195.3	217.9
47.96	19.89	40.43	61.69	83.46	105.6	127.8	150.3	172.8	195.3	217.9
48.98	19.94	40.5	61.76	83.53	105.6	127.9	150.3	172.8	195.4	218
50	19.99	40.57	61.83	83.59	105.7	127.9	150.4	172.8	195.4	218

$$-Y_0\left(\frac{\mu_m r_1}{r_2}\right)[\mu_m J_1(\mu_m) - Bi_T J_0(\mu_m)] = J_0\left(\frac{\mu_m r_1}{r_2}\right)[Bi_T Y_0(\mu_m) - \mu_m Y_1(\mu_m)]$$

(10 PPI coated foam)

Bi_t	μ_1	μ_2	μ_3	μ_4	μ_5	μ_6	μ_7	μ_8	μ_9	μ_{10}
0.001	11.33	34.9	58.28	81.63	105	128.3	151.7	175	198.3	221.7
1.021	11.98	35.11	58.41	81.73	105.1	128.4	151.7	175.1	198.4	221.7
2.042	12.56	35.33	58.54	81.82	105.1	128.4	151.8	175.1	198.4	221.8
3.062	13.09	35.54	58.67	81.91	105.2	128.5	151.8	175.1	198.5	221.8
4.083	13.57	35.74	58.79	82	105.3	128.6	151.9	175.2	198.5	221.8
5.103	14.01	35.95	58.92	82.1	105.3	128.6	151.9	175.2	198.5	221.9
6.123	14.42	36.15	59.05	82.19	105.4	128.7	152	175.3	198.6	221.9
7.144	14.79	36.35	59.17	82.28	105.5	128.7	152	175.3	198.6	221.9
8.164	15.14	36.54	59.3	82.37	105.6	128.8	152.1	175.4	198.7	222
9.184	15.46	36.73	59.42	82.46	105.6	128.9	152.1	175.4	198.7	222
10.2	15.76	36.91	59.54	82.55	105.7	128.9	152.2	175.4	198.7	222
11.23	16.04	37.09	59.66	82.64	105.8	129	152.2	175.5	198.8	222.1
12.25	16.3	37.27	59.78	82.73	105.8	129	152.3	175.5	198.8	222.1
13.27	16.54	37.44	59.9	82.82	105.9	129.1	152.3	175.6	198.8	222.1
14.29	16.77	37.61	60.02	82.9	106	129.1	152.4	175.6	198.9	222.2
15.31	16.99	37.78	60.13	82.99	106	129.2	152.4	175.7	198.9	222.2
16.33	17.19	37.94	60.25	83.08	106.1	129.3	152.5	175.7	199	222.2
17.35	17.38	38.1	60.36	83.16	106.2	129.3	152.5	175.7	199	222.3
18.37	17.56	38.25	60.48	83.25	106.3	129.4	152.6	175.8	199	222.3
19.39	17.73	38.4	60.59	83.34	106.3	129.4	152.6	175.8	199.1	222.3
20.41	17.89	38.54	60.7	83.42	106.4	129.5	152.7	175.9	199.1	222.4
21.43	18.04	38.69	60.8	83.5	106.5	129.5	152.7	175.9	199.1	222.4
22.45	18.19	38.82	60.91	83.59	106.5	129.6	152.8	176	199.2	222.4
23.47	18.33	38.96	61.02	83.67	106.6	129.7	152.8	176	199.2	222.5
24.49	18.46	39.09	61.12	83.75	106.7	129.7	152.8	176	199.3	222.5
25.51	18.58	39.22	61.22	83.83	106.7	129.8	152.9	176.1	199.3	222.5
26.53	18.7	39.34	61.32	83.91	106.8	129.8	152.9	176.1	199.3	222.6
27.55	18.81	39.47	61.42	83.99	106.9	129.9	153	176.2	199.4	222.6
28.57	18.92	39.58	61.52	84.07	106.9	129.9	153	176.2	199.4	222.6
29.59	19.03	39.7	61.62	84.15	107	130	153.1	176.2	199.4	222.7
30.61	19.13	39.81	61.71	84.23	107.1	130	153.1	176.3	199.5	222.7
31.63	19.22	39.92	61.81	84.31	107.1	130.1	153.2	176.3	199.5	222.7
32.65	19.31	40.03	61.9	84.38	107.2	130.2	153.2	176.4	199.6	222.8
33.67	19.4	40.13	61.99	84.46	107.2	130.2	153.3	176.4	199.6	222.8
34.69	19.48	40.24	62.08	84.54	107.3	130.3	153.3	176.5	199.6	222.8
35.71	19.56	40.33	62.17	84.61	107.4	130.3	153.4	176.5	199.7	222.9

36.73	19.64	40.43	62.26	84.68	107.4	130.4	153.4	176.5	199.7	222.9
37.76	19.71	40.52	62.34	84.76	107.5	130.4	153.5	176.6	199.7	222.9
38.78	19.79	40.62	62.43	84.83	107.6	130.5	153.5	176.6	199.8	223
39.8	19.85	40.71	62.51	84.9	107.6	130.5	153.6	176.7	199.8	223
40.82	19.92	40.79	62.59	84.97	107.7	130.6	153.6	176.7	199.8	223
41.84	19.98	40.88	62.67	85.04	107.7	130.6	153.6	176.7	199.9	223.1
42.86	20.05	40.96	62.75	85.11	107.8	130.7	153.7	176.8	199.9	223.1
43.88	20.11	41.04	62.83	85.18	107.9	130.7	153.7	176.8	200	223.1
44.9	20.16	41.12	62.91	85.25	107.9	130.8	153.8	176.9	200	223.2
45.92	20.22	41.2	62.98	85.31	108	130.8	153.8	176.9	200	223.2
46.94	20.27	41.27	63.06	85.38	108	130.9	153.9	176.9	200.1	223.2
47.96	20.32	41.35	63.13	85.45	108.1	130.9	153.9	177	200.1	223.3
48.98	20.37	41.42	63.2	85.51	108.1	131	154	177	200.1	223.3
50	20.42	41.49	63.27	85.58	108.2	131	154	177.1	200.2	223.3

$$-Y_0\left(\frac{\mu_m r_1}{r_2}\right)[\mu_m J_1(\mu_m) - Bi_T J_0(\mu_m)] = J_0\left(\frac{\mu_m r_1}{r_2}\right)[Bi_T Y_0(\mu_m) - \mu_m Y_1(\mu_m)]$$

(20 PPI coated foam)

Bi_t	μ_1	μ_2	μ_3	μ_4	μ_5	μ_6	μ_7	μ_8	μ_9	μ_{10}
0.001	14.98	45.84	76.51	107.2	137.8	168.4	199.1	229.7	260.3	291
1.021	15.63	46.05	76.64	107.3	137.9	168.5	199.1	229.8	260.4	291
2.042	16.23	46.27	76.77	107.3	137.9	168.6	199.2	229.8	260.4	291
3.062	16.78	46.48	76.9	107.4	138	168.6	199.2	229.8	260.5	291.1
4.083	17.3	46.69	77.03	107.5	138.1	168.7	199.3	229.9	260.5	291.1
5.103	17.78	46.9	77.16	107.6	138.2	168.7	199.3	229.9	260.5	291.1
6.123	18.22	47.1	77.28	107.7	138.2	168.8	199.4	230	260.6	291.2
7.144	18.64	47.3	77.41	107.8	138.3	168.9	199.4	230	260.6	291.2
8.164	19.04	47.5	77.54	107.9	138.4	168.9	199.5	230.1	260.6	291.2
9.184	19.41	47.7	77.66	108	138.4	169	199.5	230.1	260.7	291.3
10.2	19.76	47.89	77.78	108.1	138.5	169	199.6	230.1	260.7	291.3
11.23	20.09	48.08	77.91	108.2	138.6	169.1	199.6	230.2	260.8	291.3
12.25	20.4	48.27	78.03	108.3	138.7	169.1	199.7	230.2	260.8	291.4
13.27	20.7	48.45	78.15	108.3	138.7	169.2	199.7	230.3	260.8	291.4
14.29	20.98	48.64	78.27	108.4	138.8	169.3	199.8	230.3	260.9	291.5
15.31	21.24	48.81	78.39	108.5	138.9	169.3	199.8	230.4	260.9	291.5
16.33	21.5	48.99	78.51	108.6	138.9	169.4	199.9	230.4	260.9	291.5
17.35	21.74	49.16	78.63	108.7	139	169.4	199.9	230.4	261	291.6
18.37	21.97	49.33	78.75	108.8	139.1	169.5	200	230.5	261	291.6
19.39	22.18	49.5	78.87	108.9	139.2	169.5	200	230.5	261.1	291.6
20.41	22.39	49.66	78.98	109	139.2	169.6	200.1	230.6	261.1	291.7
21.43	22.59	49.82	79.1	109.1	139.3	169.7	200.1	230.6	261.1	291.7
22.45	22.78	49.98	79.21	109.1	139.4	169.7	200.2	230.7	261.2	291.7
23.47	22.97	50.13	79.32	109.2	139.4	169.8	200.2	230.7	261.2	291.8
24.49	23.14	50.28	79.43	109.3	139.5	169.8	200.3	230.7	261.3	291.8
25.51	23.31	50.43	79.54	109.4	139.6	169.9	200.3	230.8	261.3	291.8
26.53	23.47	50.58	79.65	109.5	139.6	169.9	200.4	230.8	261.3	291.9
27.55	23.62	50.72	79.76	109.6	139.7	170	200.4	230.9	261.4	291.9
28.57	23.77	50.86	79.87	109.6	139.8	170.1	200.5	230.9	261.4	291.9
29.59	23.92	51	79.98	109.7	139.8	170.1	200.5	231	261.4	292
30.61	24.05	51.13	80.08	109.8	139.9	170.2	200.6	231	261.5	292
31.63	24.18	51.26	80.19	109.9	140	170.2	200.6	231	261.5	292
32.65	24.31	51.39	80.29	110	140	170.3	200.6	231.1	261.6	292.1
33.67	24.43	51.52	80.39	110.1	140.1	170.3	200.7	231.1	261.6	292.1
34.69	24.55	51.65	80.49	110.1	140.2	170.4	200.7	231.2	261.6	292.1
35.71	24.67	51.77	80.59	110.2	140.2	170.5	200.8	231.2	261.7	292.2

36.73	24.78	51.89	80.69	110.3	140.3	170.5	200.8	231.2	261.7	292.2
37.76	24.88	52	80.79	110.4	140.4	170.6	200.9	231.3	261.7	292.2
38.78	24.99	52.12	80.88	110.5	140.4	170.6	200.9	231.3	261.8	292.3
39.8	25.08	52.23	80.98	110.5	140.5	170.7	201	231.4	261.8	292.3
40.82	25.18	52.34	81.07	110.6	140.6	170.7	201	231.4	261.8	292.3
41.84	25.27	52.45	81.17	110.7	140.6	170.8	201.1	231.5	261.9	292.4
42.86	25.36	52.56	81.26	110.8	140.7	170.8	201.1	231.5	261.9	292.4
43.88	25.45	52.66	81.35	110.8	140.8	170.9	201.2	231.5	262	292.4
44.9	25.54	52.76	81.44	110.9	140.8	170.9	201.2	231.6	262	292.5
45.92	25.62	52.86	81.53	111	140.9	171	201.3	231.6	262	292.5
46.94	25.7	52.96	81.62	111.1	140.9	171.1	201.3	231.7	262.1	292.5
47.96	25.77	53.06	81.71	111.1	141	171.1	201.4	231.7	262.1	292.6
48.98	25.85	53.15	81.79	111.2	141.1	171.2	201.4	231.7	262.1	292.6
50	25.92	53.25	81.88	111.3	141.1	171.2	201.4	231.8	262.2	292.6

$$Y_1\left(\frac{\lambda_n r_1}{r_2}\right)[\lambda_n J_1(\lambda_n) - Bi_m J_0(\lambda_n)] = J_1\left(\frac{\lambda_n r_1}{r_2}\right)[\lambda_n Y_1(\lambda_n) - Bi_m Y_0(\lambda_n)]$$

(5 PPI coated foam)

Bi_m	λ_1	λ_2	λ_3	λ_4	λ_5	λ_6	λ_7	λ_8	λ_9	λ_{10}
10	7.224	25.52	47.08	69.37	91.9	114.5	137.2	159.9	182.6	205.3
30.2	9.552	28.73	49.55	71.25	93.38	115.7	138.2	160.8	183.4	206
50.41	10.3	30.34	51.23	72.74	94.67	116.8	139.2	161.6	184.2	206.7
70.61	10.67	31.25	52.37	73.89	95.73	117.8	140.1	162.4	184.9	207.4
90.82	10.89	31.84	53.16	74.76	96.6	118.6	140.8	163.1	185.5	208
111	11.03	32.23	53.74	75.43	97.3	119.3	141.5	163.8	186.1	208.5
131.2	11.13	32.52	54.17	75.96	97.88	119.9	142.1	164.3	186.7	209.1
151.4	11.21	32.74	54.5	76.37	98.35	120.4	142.6	164.8	187.2	209.5
171.6	11.27	32.91	54.77	76.72	98.74	120.8	143	165.3	187.6	210
191.8	11.32	33.05	54.99	77	99.07	121.2	143.4	165.7	188	210.4
212	11.36	33.16	55.17	77.23	99.35	121.5	143.7	166	188.3	210.7
232.2	11.39	33.25	55.32	77.43	99.59	121.8	144	166.3	188.7	211
252.4	11.41	33.33	55.44	77.6	99.8	122	144.3	166.6	189	211.3
272.7	11.44	33.4	55.55	77.75	99.98	122.2	144.5	166.9	189.2	211.6
292.9	11.46	33.46	55.65	77.88	100.1	122.4	144.7	167.1	189.5	211.9
313.1	11.47	33.51	55.73	78	100.3	122.6	144.9	167.3	189.7	212.1
333.3	11.49	33.56	55.81	78.1	100.4	122.7	145.1	167.5	189.9	212.3
353.5	11.5	33.6	55.88	78.19	100.5	122.9	145.2	167.6	190	212.5
373.7	11.52	33.63	55.94	78.27	100.6	123	145.4	167.8	190.2	212.6
393.9	11.53	33.67	55.99	78.34	100.7	123.1	145.5	167.9	190.4	212.8
414.1	11.54	33.7	56.04	78.41	100.8	123.2	145.6	168.1	190.5	212.9
434.3	11.55	33.72	56.08	78.47	100.9	123.3	145.7	168.2	190.6	213.1
454.5	11.55	33.75	56.12	78.53	100.9	123.4	145.8	168.3	190.7	213.2
474.7	11.56	33.77	56.16	78.58	101	123.5	145.9	168.4	190.8	213.3
494.9	11.57	33.79	56.19	78.63	101.1	123.5	146	168.5	190.9	213.4
515.1	11.57	33.81	56.22	78.67	101.1	123.6	146.1	168.6	191	213.5
535.3	11.58	33.83	56.25	78.71	101.2	123.7	146.1	168.6	191.1	213.6
555.5	11.59	33.84	56.28	78.75	101.2	123.7	146.2	168.7	191.2	213.7
575.7	11.59	33.86	56.31	78.78	101.3	123.8	146.3	168.8	191.3	213.8
595.9	11.6	33.87	56.33	78.82	101.3	123.8	146.3	168.8	191.4	213.9
616.1	11.6	33.89	56.35	78.85	101.4	123.9	146.4	168.9	191.4	214
636.3	11.6	33.9	56.37	78.87	101.4	123.9	146.4	169	191.5	214
656.5	11.61	33.91	56.39	78.9	101.4	123.9	146.5	169	191.6	214.1
676.7	11.61	33.92	56.41	78.93	101.5	124	146.5	169.1	191.6	214.2
696.9	11.62	33.93	56.43	78.95	101.5	124	146.6	169.1	191.7	214.2
717.1	11.62	33.94	56.44	78.97	101.5	124.1	146.6	169.2	191.7	214.3

737.3	11.62	33.95	56.46	78.99	101.5	124.1	146.7	169.2	191.8	214.3
757.6	11.62	33.96	56.47	79.02	101.6	124.1	146.7	169.3	191.8	214.4
777.8	11.63	33.97	56.49	79.03	101.6	124.2	146.7	169.3	191.9	214.4
798	11.63	33.98	56.5	79.05	101.6	124.2	146.8	169.3	191.9	214.5
818.2	11.63	33.98	56.51	79.07	101.6	124.2	146.8	169.4	192	214.5
838.4	11.64	33.99	56.52	79.09	101.7	124.2	146.8	169.4	192	214.6
858.6	11.64	34	56.54	79.1	101.7	124.3	146.8	169.4	192	214.6
878.8	11.64	34	56.55	79.12	101.7	124.3	146.9	169.5	192.1	214.7
899	11.64	34.01	56.56	79.13	101.7	124.3	146.9	169.5	192.1	214.7
919.2	11.64	34.02	56.57	79.15	101.7	124.3	146.9	169.5	192.1	214.7
939.4	11.65	34.02	56.58	79.16	101.8	124.3	146.9	169.6	192.2	214.8
959.6	11.65	34.03	56.59	79.17	101.8	124.4	147	169.6	192.2	214.8
979.8	11.65	34.03	56.59	79.18	101.8	124.4	147	169.6	192.2	214.8
1000	11.65	34.04	56.6	79.2	101.8	124.4	147	169.6	192.2	214.9

$$Y_1\left(\frac{\lambda_n r_1}{r_2}\right)[\lambda_n J_1(\lambda_n) - Bi_m J_0(\lambda_n)] = J_1\left(\frac{\lambda_n r_1}{r_2}\right)[\lambda_n Y_1(\lambda_n) - Bi_m Y_0(\lambda_n)]$$

(10 PPI coated foam)

Bi_m	λ_1	λ_2	λ_3	λ_4	λ_5	λ_6	λ_7	λ_8	λ_9	λ_{10}
10	7.336	26.09	48.21	71.06	94.14	117.3	140.6	163.8	187.1	210.4
30.2	9.737	29.36	50.69	72.94	95.63	118.5	141.6	164.7	187.9	211.1
50.41	10.52	31.01	52.41	74.46	96.93	119.7	142.6	165.6	188.6	211.8
70.61	10.9	31.96	53.57	75.62	98.01	120.6	143.4	166.4	189.4	212.4
90.82	11.13	32.56	54.39	76.51	98.89	121.5	144.2	167.1	190	213
111	11.28	32.98	54.99	77.21	99.61	122.2	144.9	167.7	190.6	213.6
131.2	11.39	33.28	55.44	77.75	100.2	122.8	145.5	168.3	191.2	214.1
151.4	11.47	33.51	55.79	78.18	100.7	123.3	146	168.8	191.7	214.6
171.6	11.53	33.69	56.07	78.54	101.1	123.7	146.5	169.3	192.1	215.1
191.8	11.58	33.83	56.29	78.83	101.4	124.1	146.9	169.7	192.5	215.5
212	11.62	33.95	56.48	79.08	101.7	124.4	147.2	170	192.9	215.8
232.2	11.65	34.04	56.64	79.28	102	124.7	147.5	170.3	193.2	216.2
252.4	11.68	34.13	56.77	79.46	102.2	125	147.8	170.6	193.5	216.5
272.7	11.7	34.2	56.89	79.62	102.4	125.2	148	170.9	193.8	216.7
292.9	11.72	34.26	56.99	79.75	102.6	125.4	148.2	171.1	194	217
313.1	11.74	34.31	57.07	79.87	102.7	125.6	148.4	171.3	194.3	217.2
333.3	11.76	34.36	57.15	79.98	102.8	125.7	148.6	171.5	194.5	217.4
353.5	11.77	34.4	57.22	80.08	103	125.8	148.8	171.7	194.6	217.6
373.7	11.78	34.44	57.28	80.16	103.1	126	148.9	171.8	194.8	217.8
393.9	11.8	34.48	57.34	80.24	103.2	126.1	149	172	195	218
414.1	11.81	34.51	57.39	80.31	103.2	126.2	149.2	172.1	195.1	218.1
434.3	11.82	34.54	57.44	80.37	103.3	126.3	149.3	172.2	195.2	218.3
454.5	11.82	34.56	57.48	80.43	103.4	126.4	149.4	172.4	195.4	218.4
474.7	11.83	34.59	57.52	80.48	103.5	126.5	149.5	172.5	195.5	218.5
494.9	11.84	34.61	57.55	80.53	103.5	126.5	149.5	172.6	195.6	218.6
515.1	11.85	34.63	57.59	80.58	103.6	126.6	149.6	172.7	195.7	218.7
535.3	11.85	34.65	57.62	80.62	103.6	126.7	149.7	172.7	195.8	218.8
555.5	11.86	34.66	57.65	80.66	103.7	126.7	149.8	172.8	195.9	218.9
575.7	11.86	34.68	57.67	80.7	103.7	126.8	149.8	172.9	196	219
595.9	11.87	34.69	57.7	80.73	103.8	126.8	149.9	173	196	219.1
616.1	11.87	34.71	57.72	80.76	103.8	126.9	149.9	173	196.1	219.2
636.3	11.88	34.72	57.74	80.79	103.9	126.9	150	173.1	196.2	219.3
656.5	11.88	34.73	57.76	80.82	103.9	127	150.1	173.1	196.2	219.3
676.7	11.89	34.74	57.78	80.85	103.9	127	150.1	173.2	196.3	219.4
696.9	11.89	34.76	57.8	80.87	104	127	150.1	173.2	196.3	219.5
717.1	11.89	34.77	57.82	80.9	104	127.1	150.2	173.3	196.4	219.5

737.3	11.9	34.78	57.83	80.92	104	127.1	150.2	173.3	196.5	219.6
757.6	11.9	34.78	57.85	80.94	104	127.2	150.3	173.4	196.5	219.6
777.8	11.9	34.79	57.86	80.96	104.1	127.2	150.3	173.4	196.6	219.7
798	11.9	34.8	57.88	80.98	104.1	127.2	150.3	173.5	196.6	219.7
818.2	11.91	34.81	57.89	81	104.1	127.2	150.4	173.5	196.6	219.8
838.4	11.91	34.82	57.9	81.02	104.1	127.3	150.4	173.5	196.7	219.8
858.6	11.91	34.82	57.91	81.03	104.2	127.3	150.4	173.6	196.7	219.9
878.8	11.91	34.83	57.93	81.05	104.2	127.3	150.5	173.6	196.8	219.9
899	11.92	34.84	57.94	81.06	104.2	127.3	150.5	173.6	196.8	219.9
919.2	11.92	34.84	57.95	81.08	104.2	127.4	150.5	173.7	196.8	220
939.4	11.92	34.85	57.96	81.09	104.2	127.4	150.5	173.7	196.9	220
959.6	11.92	34.86	57.97	81.11	104.3	127.4	150.6	173.7	196.9	220.1
979.8	11.92	34.86	57.98	81.12	104.3	127.4	150.6	173.8	196.9	220.1
1000	11.93	34.87	57.98	81.13	104.3	127.4	150.6	173.8	196.9	220.1

$$Y_1\left(\frac{\lambda_n r_1}{r_2}\right)[\lambda_n J_1(\lambda_n) - Bi_m J_0(\lambda_n)] = J_1\left(\frac{\lambda_n r_1}{r_2}\right)[\lambda_n Y_1(\lambda_n) - Bi_m Y_0(\lambda_n)]$$

(20 PPI coated foam)

$\mathrm{Bi_m}$	λ_1	λ_2	λ_3	λ_4	λ_5	λ_6	λ_7	λ_8	λ_9	λ_{10}
10	8.69	33.48	62.81	92.94	123.3	153.8	184.3	214.9	245.4	276
30.2	12.01	37.33	65.49	94.9	124.8	155	185.4	215.8	246.2	276.7
50.41	13.19	39.55	67.54	96.6	126.2	156.2	186.4	216.6	247	277.4
70.61	13.8	40.92	69.07	98	127.5	157.3	187.3	217.5	247.8	278.1
90.82	14.17	41.84	70.21	99.15	128.5	158.2	188.2	218.3	248.5	278.7
111	14.42	42.49	71.08	100.1	129.5	159.1	189	219	249.1	279.4
131.2	14.59	42.97	71.76	100.9	130.2	159.9	189.7	219.7	249.8	280
151.4	14.73	43.34	72.29	101.5	130.9	160.5	190.3	220.3	250.4	280.5
171.6	14.83	43.63	72.73	102	131.5	161.1	190.9	220.9	250.9	281
191.8	14.91	43.87	73.09	102.5	132	161.7	191.5	221.4	251.4	281.5
212	14.98	44.06	73.39	102.8	132.4	162.1	191.9	221.9	251.9	282
232.2	15.03	44.23	73.65	103.2	132.8	162.5	192.4	222.3	252.3	282.4
252.4	15.08	44.37	73.87	103.5	133.1	162.9	192.8	222.7	252.7	282.8
272.7	15.12	44.48	74.06	103.7	133.4	163.2	193.1	223.1	253.1	283.2
292.9	15.16	44.59	74.22	103.9	133.7	163.5	193.4	223.4	253.4	283.5
313.1	15.19	44.68	74.37	104.1	133.9	163.8	193.7	223.7	253.7	283.8
333.3	15.22	44.76	74.5	104.3	134.1	164	194	224	254	284.1
353.5	15.24	44.83	74.62	104.5	134.3	164.3	194.2	224.2	254.3	284.4
373.7	15.26	44.9	74.72	104.6	134.5	164.5	194.4	224.5	254.5	284.7
393.9	15.28	44.95	74.81	104.7	134.7	164.6	194.6	224.7	254.8	284.9
414.1	15.3	45.01	74.9	104.8	134.8	164.8	194.8	224.9	255	285.1
434.3	15.32	45.05	74.98	104.9	134.9	165	195	225.1	255.2	285.3
454.5	15.33	45.1	75.05	105	135.1	165.1	195.2	225.3	255.4	285.5
474.7	15.34	45.14	75.12	105.1	135.2	165.2	195.3	225.4	255.6	285.7
494.9	15.36	45.17	75.18	105.2	135.3	165.4	195.5	225.6	255.7	285.9
515.1	15.37	45.21	75.23	105.3	135.4	165.5	195.6	225.7	255.9	286.1
535.3	15.38	45.24	75.28	105.4	135.5	165.6	195.7	225.9	256	286.2
555.5	15.39	45.27	75.33	105.4	135.5	165.7	195.8	226	256.2	286.4
575.7	15.4	45.3	75.38	105.5	135.6	165.8	195.9	226.1	256.3	286.5
595.9	15.41	45.32	75.42	105.5	135.7	165.9	196	226.2	256.4	286.6
616.1	15.41	45.35	75.46	105.6	135.8	165.9	196.1	226.3	256.5	286.8
636.3	15.42	45.37	75.49	105.7	135.8	166	196.2	226.4	256.6	286.9
656.5	15.43	45.39	75.53	105.7	135.9	166.1	196.3	226.5	256.7	287
676.7	15.43	45.41	75.56	105.7	135.9	166.2	196.4	226.6	256.8	287.1
696.9	15.44	45.43	75.59	105.8	136	166.2	196.4	226.7	256.9	287.2
717.1	15.45	45.44	75.62	105.8	136	166.3	196.5	226.8	257	287.3

737.3	15.45	45.46	75.65	105.9	136.1	166.3	196.6	226.8	257.1	287.4
757.6	15.46	45.48	75.67	105.9	136.1	166.4	196.6	226.9	257.2	287.5
777.8	15.46	45.49	75.7	105.9	136.2	166.4	196.7	227	257.3	287.6
798	15.47	45.51	75.72	106	136.2	166.5	196.8	227	257.3	287.6
818.2	15.47	45.52	75.75	106	136.3	166.5	196.8	227.1	257.4	287.7
838.4	15.48	45.53	75.77	106	136.3	166.6	196.9	227.2	257.5	287.8
858.6	15.48	45.54	75.79	106.1	136.3	166.6	196.9	227.2	257.5	287.9
878.8	15.48	45.56	75.81	106.1	136.4	166.7	197	227.3	257.6	287.9
899	15.49	45.57	75.83	106.1	136.4	166.7	197	227.3	257.7	288
919.2	15.49	45.58	75.84	106.1	136.4	166.7	197.1	227.4	257.7	288
939.4	15.5	45.59	75.86	106.2	136.5	166.8	197.1	227.4	257.8	288.1
959.6	15.5	45.6	75.88	106.2	136.5	166.8	197.1	227.5	257.8	288.2
979.8	15.5	45.61	75.89	106.2	136.5	166.9	197.2	227.5	257.9	288.2
1000	15.5	45.62	75.91	106.2	136.6	166.9	197.2	227.6	257.9	288.3